A Multi-Component Mass Transport Model for Polymer Electrolyte Fuel Cells

by

Chad Adam Balen

A thesis submitted in partial fulfillment of the requirements for the degree of

Master of Science

Department of Mechanical Engineering

University of Alberta

Abstract

Polymer electrolyte fuel cells (PEFCs) operate with a ternary mixture of fuel and reactants. The majority of numerical models in the literature, including the in-house Open-source Fuel Cell Simulation Toolbox (OpenFCST) software, use Fick's law of diffusion which is only valid for binary mixtures. An accurate multi-component mass transport (MMT) model accounting for both convective and diffusive transport is necessary to improve PEFC performance predictions and assess the errors due to the use of Fick's law. The focus of this research is the implementation of a novel isothermal compressible MMT model. The new model will allow OpenFCST to perform along the channel and possibly 3-dimensional PEFC simulations.

In the porous media of the fuel cell, the volume averaging method is applied to the equations resulting in an additional Darcy-Forchheimer term. Diffusion coefficients and dynamic viscosities of the species are calculated using Chapman-Enskog theory. The partial dynamic viscosity of the gas species are calculated using either Wilke's or Kerkhof and Geboers' model. The MMT model is validated by comparing results to several benchmark problems, including a Stefan tube problem. The Stefan tube solution showed a maximum molar fraction error of 0.007 (1.6%) compared to the analytical Maxwell-Stefan solution, which is considered to be within an acceptable range. Finally, the MMT model is coupled with electron and proton transport, and electrochemical reaction equations in order to develop a PEFC cathode model. Performance predictions of the multi-component and Fick's cathode models are compared to show the effect of the improved model.

Keywords: polymer electrolyte fuel cell, finite element method, isothermal, compressible, multi-component convective-diffusive mass transport, Darcy-Forchheimer

"I have come to believe that the whole world is an engima, a harmless enigma that is made terrible by our own mad attempt to interpret it as though it had an underlying truth"

- Umberto Eco

Acknowledgements

I would like to thank my supervisor Dr. Marc Secanell for providing me the opportunity to pursue research in numerically modeling fuel cells. Before I started, you told me that you will expect more from me than other supervisors. I was fine with that because nothing great is ever easy. Over the past two and a half years I have learned so much from you. You always set the expectations high and pushed me to do more and be better, even when I did not want to. I have you to thank for my success.

I would also like to thank my colleagues for all your help and support. We have had fun over these past two and a half years. The potlucks and movie nights were always nice to de-stress after a long day. Thank you Aslan and Jie for your help with checking over my math and help with derivations. Aslan you always pushed me to improve the quality and rigorousness in my derivations and proofs. Toni you made the end of my time at ESDL enjoyable with our pranks, and how you helped me see there is more to life than just sitting in front of my computer. Alex, you have helped me so much in the final stages of thesis writing. Thank you Dietrich, Jin, and Gio. We started in undergrad together and now we are graduating from grad school. I am sad that I will not be able to spend more time here with all you guys. I will miss the meetings and how you were my guinea pigs for my new cakes, ice cream, apple crumble, and chocolate truffle recipes, but I am sure you guys never minded.

Finally, I would like to thank my family. It has been a long journey to this point that would not have been possible without your support. I have you to thank for molding me into the man I have become. Thank you for pushing me to achieve more and to pursue my education. You raised me to always put the highest quality into my work and I hope I have made you proud.

Table of Contents

List of Tables

List of Figures

Nomenclature

English Letters

$\boldsymbol{F}_i$	External force vector field, $[\mathrm{g\,cm\,s^{-2}}]$
$\boldsymbol{g}$	Gravity vector field, $[\mathrm{cm\,s^{-2}}]$
$\boldsymbol{v}$	Velocity vector field, $[\mathrm{cm\,s^{-1}}]$
$\boldsymbol{w}$	Vector test function for velocity
$D_{\alpha\beta}$	Fick's diffusion coefficient, $[\mathrm{m^2\,s^{-1}}]$
$\hat{\mathbf{I}}$	Identity tensor
$\mathscr{D}_{\alpha\beta}$	Maxwell-Stefan's diffusion coefficient, $[\mathrm{cm^2\,s^{-1}}]$
$\hat{\mathbf{K}}$	Intrinsic permeability tensor, $[\mathrm{cm^2}]$
P	Pressure, $[\mathrm{g\,cm^{-1}\,s^{-2}}]$
J	Volumetric current density $[\mathrm{A\,cm^{-3}}]$
D^T	Multi-component thermal diffusion coefficients, $[\mathrm{g\,cm^{-1}\,s^{-1}}]$
d_e	Equivalent diameter [cm]
d_h	Hydraulic diameter [cm]
F	Faraday's constant $[96\,485\,\mathrm{C\,mol^{-1}}]$
h	Relaxation factor
j	Current density $[\mathrm{A\,cm^{-2}}]$
k	Boltzmann constant, $[1.381 \times 10^{-23}\,\mathrm{J\,K^{-1}}]$
M	Molar mass, $[\mathrm{g\,mol^{-1}}]$

N_A Avogadro's constant, $[6.022 \times 10^{23}\,\mathrm{molecule\,mol^{-1}}]$

q Scalar test function for density

R Ideal gas constant, $[8.314 \times 10^{7}\,\mathrm{g\,cm^{2}\,s^{-2}\,K^{-1}\,mol^{-1}}]$

T Temperature, [K]

t Time, [s]

V_{REV} Total volume of the REV

Abbreviations

BFM Binary Friction Model

CL Catalyst Layer

deal.II Differential Equations Analysis Library

DGM Dusty Gas Model

dofs Degrees of Freedom

ESDL Energy Systems Design Laboratory

OpenFCST Open-source Fuel Cell Simulation Toolbox

FEA Finite Element Analysis

GDL Gas Diffusion Layer

HOR Hydrogen Oxidation Reaction

MMT Multi-component Mass Transport

MPL Microporous Layer

ORR Oxygen Reduction Reaction

PEFC Polymer Electrolyte Fuel Cell

PEM Polymer Electrolyte Membrane

REV Representative Elementary Volume

Re Reynolds number

SOFC Solid Oxide Fuel Cell

ARS Adaptive Refinement Study

FEM Finite Element Method

GIS Grid Independence Study

ICCP Ionomer Covered Catalyst Particle

LHS Left Hand Side

LU Lower Upper

MPI Message Passing Interface

MUMPS MUltifrontal Massively Parallel sparse direct Solver

PDE Partial Differential Equation

PETSc Portable, Extensible Toolkit for Scientific Computation

RH Relative Humidity

RHS Right Hand Side

UMFPACK Unsymmetric MultiFrontal Package

Greek Letters

$\Omega_{\alpha\beta}^{(\ell,s)}$ Collision integral

Ω_D^* Dimensionless diffusion collision integral

$\Omega_{\alpha\beta}^*$ Dimensionless collision integral

Ω_η^* Dimensionless viscosity collision integral

ϵ Maximum attractive energy between two molecules, [J]

η Partial dynamic viscosity, $[\mathrm{g\,cm^{-1}\,s^{-1}}]$

η^0 Dynamic viscosity of a pure substance, $[\mathrm{g\,cm^{-1}\,s^{-1}}]$

$\hat{\boldsymbol{\beta}}$ Forchheimer correction tensor, [cm]

Γ Boundary of Ω

λ Bulk viscosity, $[\mathrm{g\,cm^{-1}\,s^{-1}}]$

μ Porosity network constant

$\mu_{\alpha\beta}$ Reduced mass between species α and β, $[\mathrm{kg\,molecule^{-1}}]$

Ω Domain in $\mathbb{R}^n$

Φ Test function vector

ϕ_m Membrane electrical potential, [V]

ϕ_s Solid electrical potential, [V]

ε Porosity

ε_{th} Percolation threshold for the lattice that presents the catalyst layer

ρ Density, $[\mathrm{g\,cm^{-3}}]$

σ Collision diameter, [m]

λ_{stoic} Air to stoichiometric mixture ratio

Γ Thermodynamic correction factor

τ Tortuosity

$\hat{\boldsymbol{\tau}}$ Viscous stress tensor, $[\mathrm{g\,cm^{-1}\,s^{-2}}]$

ζ Second viscosity, $[\mathrm{g\,cm^{-1}\,s^{-1}}]$

Mathematical Operators

: Frobenius inner product, i.e. the component-wise inner product of two matrices (or tensors of rank 2) as if they were vectors ($\hat{\boldsymbol{A}} : \hat{\boldsymbol{B}} = tr(\hat{\boldsymbol{A}}^T \hat{\boldsymbol{B}})$)

δ Variation operator

∇_s Symmetric gradient, i.e. $\nabla_s = \frac{1}{2}\left(\nabla + \nabla^T\right)$

$\otimes$ Dyadic product between two vectors, i.e. $\boldsymbol{a} \otimes \boldsymbol{b} = \boldsymbol{a}\boldsymbol{b}^T$

d_h Hydraulic diameter, [cm]

S Backwards step height, [cm]

U_{avg} Average velocity, [$\mathrm{cm\,s^{-1}}$]

x_1 Lower reattachment length for backwards channel step flow, [cm]

Subscripts and Superscripts

α,β Species indices

$\hat{}$ Above character (i.e. $\hat{\boldsymbol{A}}$) represents a tensor

c Channel

f Fluid

fs Frontal surface

mix Mixture

p Porous layer

t Total

Chapter 1

Introduction

1.1 Motivation

In recent years the need to reduce carbon emissions to mitigate climate change has been a growing concern. Although, it cannot be said that there has not been resistance. For instance, in 2011 Canada announced that it was withdrawing from the Kyoto Protocol out of fears of the effect to the Canadian economy [3]. No matter what side a person takes on the issue of climate change, fossil fuels are a non-renewable resource and one day they will be depleted. For this reason, alternative energy resources need to be investigated to find better and more efficient energy sources. A problem that plagues some alternative energy sources, like solar and wind energy, is that they cannot provide a consistent source of power. Instead they require efficient energy storage methods and should be used as a hybrid system [4]. One possibility to integrate renewable energy and storage, is to use solar and/or wind electricity to produce hydrogen via water electrolysis. This hydrogen could then be used in fuel cell vehicles to eliminate transportation emissions. One reason to use hydrogen as the form for energy storage instead of batteries is because of their higher energy density.

Fuel cells work by producing electrical energy directly from a chemical reaction. This leads to less stages for energy loss, and results in greater efficiencies than that of a combustion engine [5, 6]. Fuel cells vary in type based on factors such as the temperature, electrolyte, and fuel used. Polymer Electrolyte Fuel Cells (PEFCs) have shown considerable promise. They have high efficiencies, fast refueling times, and are capable of operating at low temperatures. For these reasons, PEFCs are considered a viable option for applications to the automotive industry. Current fuel cell vehicles commercially produced include the Hyundai Tucson FCEV, Toyota Mirai, and Honda Clarity. As well, PEFCs are being investigated for use in laptops [7], airplanes [8, 9], and forklifts [10].

One of the major challenges with PEFCs is the associated fabrication cost. This is because PEFCs run at low temperatures, and as such require platinum as a catalyst for the

chemical reaction to occur. For this reason, one major focus of current research is reducing the amount of platinum required while maintaining performance [11, 12]. One day the use of platinum as a catalyst may not even be necessary as some researchers are even investing other possible catalysts for PEFCs [13–15].

PEFC research based entirely on experiments becomes very costly, due to the platinum and other materials required for testing different configurations to find a more efficient solution. As well, due to the small scales at which the processes take place it is currently impossible to directly observe some of the fundamental phenomena that occurs in a fuel cell. This is where numerical modeling can be advantageous in PEFC design. Simulations can be run to test different design parameters and find an optimal solution so only a few experiments have to be done based on the simulation results.

Modeling a PEFC is a multi-physics and multi-phase problem. Equations for the different aspects of a PEFC including the electrochemistry, mass transport, heat transfer, and liquid water transport are all coupled together. For this reason, it can be difficult to find an optimal design using experiments alone. As one parameter may improve a PEFC in certain aspects it may also inhibit others, for this reason a balance must be found. The Open-source Fuel Cell Simulation Toolbox (OpenFCST) [16, 17] has been developed to account for these different coupled equations. OpenFCST was originally developed by Secanell [18], and has been improved to include the effects of catalyst layer (CL) structure [19], multiple kinetic models [20, 21], non-isothermal two-phase transport [22–24], and different aspects of mass transport [25, 26]. This work aims to improve OpenFCST by implementing a multi-component mass transport model to better predict the effects of mass transport losses in a PEFC.

The losses of a PEFC can be broken into three regions, the kinetic, ohmic, and mass transport losses. This is shown in Figure 1.1. At low overpotentials, kinetic losses dominate. Kinetic losses are the result of the need to overcome the activation energy required for the chemical reactions to occur. Ohmic losses occur at moderate overpotentials, and are due to ionic and electronic conduction losses. Mass transport losses are the result of the combination of two factors: 1) the inability to provide fuel and oxidant fast enough to the electrochemical reaction site, (called "starvation"), and 2) the increased production of water leading to liquid water accumulation in gas pores thereby blocking gas transport (called "flooding"). These two factors determine the limiting current of a PEFC, and for this reason it is an important aspect that needs to be accurately modeled for optimal PEFC design. To do this, an accurate model for the multi-component transport was implemented to determine the transport of the different gas species in a PEFC.

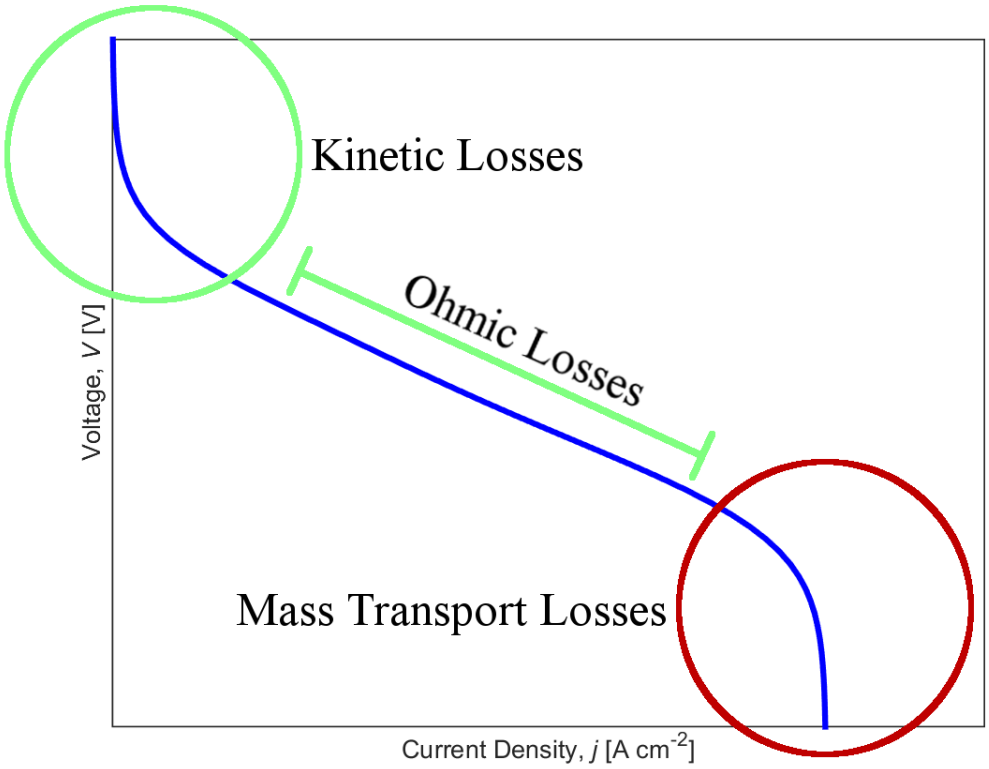

Figure 1.1 – PEFC typical performance curve illustrating the three main regions of operation: kinetic, ohmic, and mass transport

1.2 PEFC Background

A combustion engine works by running a hydrocarbon combustion reaction to produce heat. This heat is then transformed into mechanical work. If electrical power is the end goal, then this mechanical work must then be converted to electricity. Each of these stages results in a loss of energy making the overall process very inefficient. Alternatively, a PEFC operates by transforming hydrogen and oxygen into water and the byproduct of the reaction is electricity. Due to this direct conversion from chemical to electrical energy there are less stages for energy loss to occur and the overall process is much more efficient than a combustion engine.

The overall reaction that occurs in a PEFC is expressed as:

$$H_2 + \frac{1}{2}O_2 \rightleftharpoons H_2O \tag{1.1}$$

This reaction alone does not produce electrical power, instead the reaction must be split into two electrochemical half cell reactions. That way electrons are formed as an intermediate product that can be used to produce electrical power. This is possible through the use of

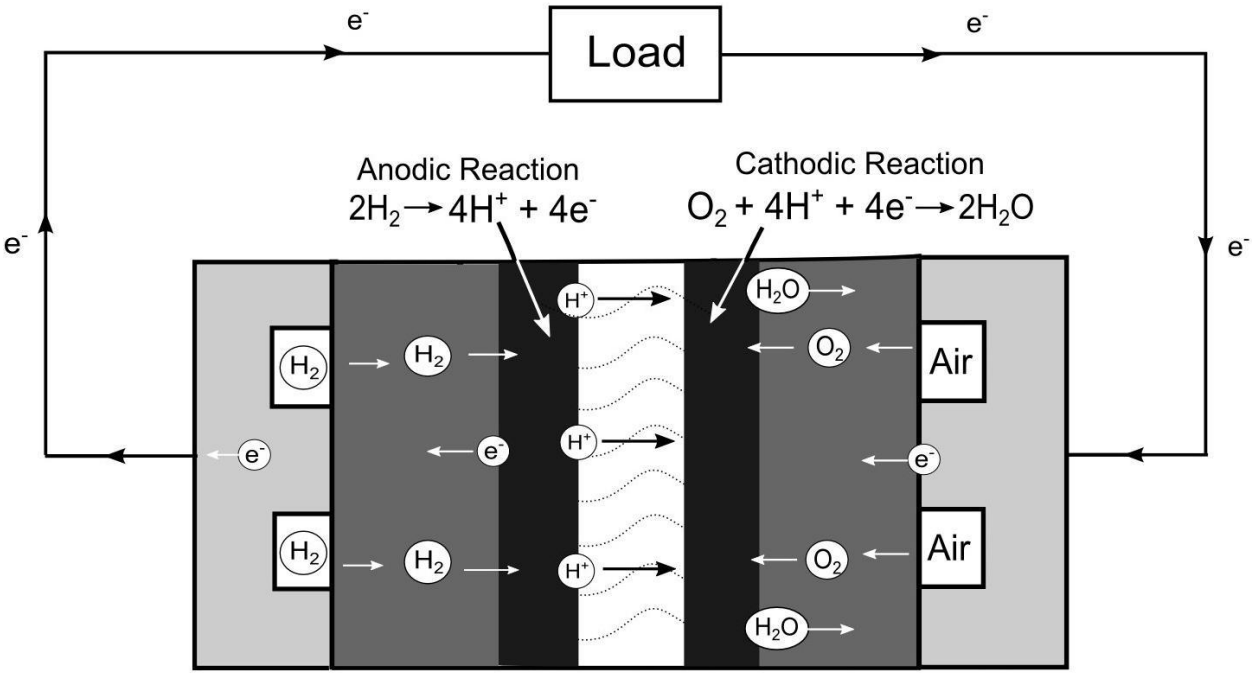

Figure 1.2 – Basic operation of a PEFC. Reprinted with permission [2]

an electrolyte. An electrolyte allows protons to pass through but prevents the electrons from doing so. For this reason, the electrons need to take a different path to the reaction site. Through this path they can be used to produce electrical power before completing the overall chemical reaction. In a PEFC, these two electrochemical half cell reactions occur on each side of the PEFC, the anode and cathode, and are separated by a polymer electrolyte membrane (PEM). This process is shown in Figure 1.2.

Hydrogen is supplied on the anode side where it diffuses through the anode's gas diffusion layer (GDL) and microporous layer (MPL). The hydrogen then reacts in the anode's CL producing protons and electrons as shown in the reaction:

$$H_2 \rightleftharpoons 2H^+ + 2e^- \tag{1.2}$$

This reaction is called the hydrogen oxidation reaction (HOR). The protons are able to diffuse through the PEM, typically Nafion®, a sulfonated tetrafluoroethylene polymer. As mentioned previously the PEM is an electrolyte, thus the protons are conducted through while insulating electron transport. Instead, the electrons travel in the opposite direction and pass through a circuit where they can be used to produce electrical power.

Oxygen, typically in the form of air, is supplied on the cathode side. Similar to hydrogen, the oxygen diffuses through the cathode's GDL and MPL. At the cathode's CL the oxygen,

protons, and electrons combine producing water, as shown in the reaction:

$$\frac{1}{2}O_2 + 2H^+ + 2e^- \rightleftharpoons H_2O \tag{1.3}$$

This reaction is called the oxygen reduction reaction (ORR). The water produced then diffuses through the cathode's MPL and GDL where it is removed from the PEFC through the cathode channel.

Although the GDL and MPL are not directly involved in the electrochemical reaction they increase the overall performance of a PEFC. GDLs are typically made of carbon paper, and the MPL consists of carbon black nanoparticles and polytetrafluoroethelyne (PTFE) coated on top of the GDL. As well, the GDL is typically treated with PTFE to give it hydrophobic properties. This ensures that water is removed from the layers to reduce "flooding" effects. More information on the production process for GDLs can be found in [27].

The GDL provides a support to the thinner layers. As the name implies the GDL helps the gases evenly distribute as they diffuse to the CL. This reduces losses as more oxygen and hydrogen is able to reach the CL reaction sites below the bipolar plate. The MPL is not a requirement for a fuel cell to operate, however the GDL and CL have pores on the scale of 10 to 30 µm and 10 to 100 nm respectively [28]. The MPL reduces contact resistance and encourages liquid water transport by having pores at an intermediate size in comparison to the two layers. Further, the CL is very delicate because it has a thickness of 10 to 50 µm [28]. The GDL provides structural support as it has a thickness on the order of 100 to 400 µm [28].

1.3 Literature Review

Most models can trace their roots to the 1-dimensional (1D) models developed by either Springer et al. [29] or Bernardi and Verbrugge [30]. These early models were reasonably detailed and could determine the performance of a fuel cell. The problem is that they are 1D models, and 2D effects such as channel geometry cannot be considered. Parameters for these early models were possibly curve fitted to experimental data. This is a problem because differences between the results of the model and experimental data could be due to the assumptions used. By curve fitting a parameter may be changed to an unrealistic value to account for some other effect not being accounted for. As a result, it can be difficult to run optimization studies as the model may no longer be valid outside of the data it was fitted to. For this reason, greater emphasis has been placed on numerical models based on governing equations that physically describe the true geometry and physical phenomena that occurs inside a fuel cell. These governing equations that describe fuel cell operation are typically

nonlinear, multi-physics, multi-phase models that describe the most salient physical aspects in a fuel cell.

One reason that 2D models are attractive when modeling different behaviour in a PEFC is the computational expense compared to 3D models. 2D models can use anywhere from 1000 to 10 000 elements, while 3D models typically require 100 000 to a few million elements [31]. Figure 1.3 displays the two domains that can be considered in 2D PEFC simulations. Through the channel 2D simulations [32–35] have the benefit of possibly only considering the porous media domain and using symmetry boundary conditions to only represent half of the channel and bipolar plate region. Since only the porous domain is considered, the boundary condition used at the GDL-channel interface is a constant density boundary condition. This is problematic because as the fuel progresses through the channel it will be consumed, resulting in less reactant being available downstream. To accurately predict the consumption of fuel along the channel an accurate mass transport model is required. This can be difficult because usually one set of governing equations valid for the entire domain is desired. So, the model must be capable of describing the transport in both the channel, where convection dominates, and the porous layers, where diffusion dominates.

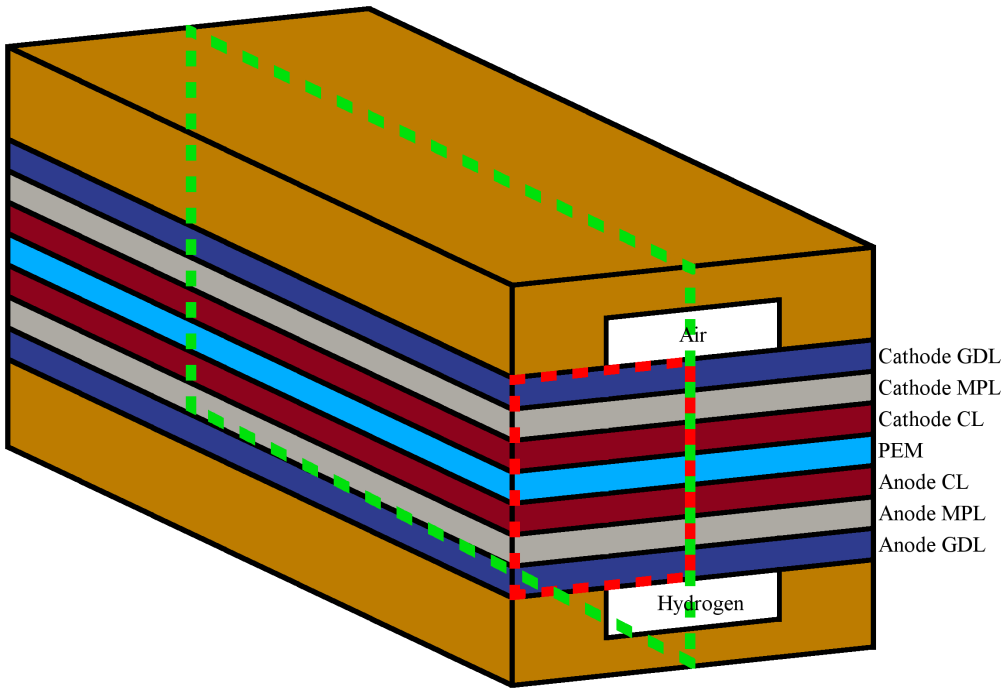

Figure 1.3 – 3D schematic of one channel of a PEFC. The red rectangle displays the through the channel 2D domain, and the green rectangle displays the along the channel 2D domain

1.3.1 Mass Transport in a Porous Media

Fick's second law of diffusion was first derived by Adolf Fick in 1855 [36] and can be expressed as:

$$\frac{\partial C_\alpha}{\partial t} = \nabla \cdot (C_t D_{\alpha\beta} \nabla x_\alpha) \tag{1.4}$$

where index α represents the species, C_α is the concentration of the species ($\mathrm{mol\,cm^{-3}}$), t is time (s), C_t is the total concentration of the mixture ($\mathrm{mol\,cm^{-3}}$), $D_{\alpha\beta}$ is Fick's diffusion coefficient ($\mathrm{cm^2\,s^{-1}}$), and x is the molar fraction. Fick's law of diffusion is meant for describing diffusion of binary mixtures. Only for infinitely dilute multi-component mixtures is Fick's law appropriate to approximate diffusion in a multi-component mixture [37]. This assumption assumes that the species are extremely diluted in a solvent, resulting in the diluted solute species only interacting with the solvent. This assumption is typically used in fuel cell modeling. As a result, several models still use Fick's law for the determining the mass transport [38–42].

The more generalized Maxwell-Stefan model for diffusive transport can be expressed as [43, 44]:

$$-C_t \nabla x_\alpha = \sum_{\alpha \neq \beta}^{N} \frac{x_\alpha \boldsymbol{N}_\beta - x_\beta \boldsymbol{N}_\alpha}{\mathscr{D}_{\alpha\beta}} \tag{1.5}$$

where C_t is the total concentration ($\mathrm{mol\,cm^{-3}}$), $\boldsymbol{N}$ is the molar flux ($\mathrm{mol\,cm^{-2}\,s^{-1}}$), and $\mathscr{D}_{\alpha\beta}$ is the Maxwell-Stefan diffusion coefficient ($\mathrm{cm^2\,s^{-1}}$). The Maxwell-Stefan equations are more accurate for a multi-component mixture because they account for the interactions between all the species. These extra interactions, not accounted for by Fick's law, can result in unintuitive diffusive transport phenomena; i.e. reverse diffusion, osmotic diffusion, and a diffusion barrier [45]. Reverse diffusion occurs when a species diffuses from low to high concentration gradient, the opposite of what Fick's law describes. Osmotic diffusion occurs when diffusion occurs even though no concentration gradient is present. Finally, a diffusion barrier occurs when no diffusion occurs, even though there is a concentration gradient. A good example of these phenomena was shown in experiments performed by Duncan and Toor [46]. In the Duncan and Toor experiment, osmotic and reverse diffusion occurred because one of the gas species was "pulled" by another as it diffused from a high to low concentration gradient.

Although more complex to implement, resulting in increased computational time and storage, the Maxwell-Stefan equations will typically lead to a more accurate solution than Fick's law. This has been shown to be true in other fields, such as membrane distillation as studied by Banat et al. [47]. In the case of PEFCs, Lindstrom and Wetton did a mathematical analysis of the gas mixture in the GDL of a PEFC and found that the results using Fick's law and the Maxwell-Stefan equations only differed by a few percent [48]. Martínez et al.

investigated the difference in results of the Maxwell-Stefan equations and the approximated multi-component (AMC) model, which is based on Fick's law. Martínez et al. found that the maximum error between the two results was at most 5% [49].

The dusty gas model (DGM) has been proposed at least five times throughout the years [50], Evans et al. [51], and Mason and Malinauskas [52] are the most commonly associated with the DGM. When the total pressure is uniform the DGM is expressed as [53]:

$$-\frac{1}{RT}\nabla P_\alpha = \sum_{\alpha\neq\beta}^{N}\frac{x_\alpha \boldsymbol{N}_\beta - x_\beta \boldsymbol{N}_\alpha}{\mathscr{D}_{\alpha\beta}} - \frac{\boldsymbol{N}_\beta}{D_\beta^K} \tag{1.6}$$

where R is the ideal gas constant ($8.314\times10^7\,\mathrm{g\,cm^2\,s^{-2}\,K^{-1}\,mol^{-1}}$), T is the temperature (K), P_α is the pressure of species α ($\mathrm{g\,cm^{-1}\,s^{-2}}$), and D^K is the Knudsen diffusion coefficient ($\mathrm{cm^2\,s^{-1}}$). Interestingly in the case of solid oxide fuel cells (SOFCs), Suwanwarangkul et al. determined Fick's law better described diffusive transport compared to the Maxwell-Stefan equations, and found the DGM to be the most accurate [54]. However, Vural et al. has criticized Suwanwarangkul et al. for assuming argon's molar fraction to be constant, and for using the same tortuosity fitting parameter for each model instead of fitting tortuosity to each model individually [55]. Vural et al. instead found the results from the Maxwell-Stefan equations and the DGM to be comparable with the tortuosity having a substantial effect on differences [55].

The DGM is considered an extension of the Maxwell-Stefan equations to include Knudsen diffusion. In recent years, some researchers have begun to reject the DGM [56–58], after Kerkhof pointed out a self-consistency issue in the DGM where viscous forces were accounted for twice [59]. In the same article that Kerkhof criticized the DGM he went on to develop his own model, called the binary friction model (BFM) [59], based on the Lightfoot friction model [60]. For isothermal gases, Kerkhof's BFM is expressed as:

$$\frac{1}{P_t}\nabla P_\alpha = RT\sum_{\alpha\neq\beta}^{N}\Phi_{\alpha\beta}\frac{x_\beta \boldsymbol{N}_\alpha - x_\alpha \boldsymbol{N}_\beta}{P_t\mathscr{D}_{\alpha\beta}} - \left(D_\beta^K + \frac{\hat{\mathbf{K}}}{\kappa_\beta}\right)^{-1}\frac{RT}{P_t}\boldsymbol{N}_\beta \tag{1.7}$$

$$\Phi_{\alpha\beta} = \begin{cases} 1 & \text{in the continuum regime} \\ \frac{\Lambda_{\alpha\beta}}{r_0} & \text{in the Knudsen regime} \end{cases} \tag{1.8}$$

$$\kappa_\beta = \frac{\eta_\beta^0}{P_t\sum_{k=1}^{N}x_k\xi_{\beta k}} \tag{1.9}$$

$$\xi_{\alpha\beta} = \frac{\left[1+(\eta_\alpha^0/\eta_\beta^0)^{1/2}(M_\beta/M_\alpha)^{1/4}\right]^2}{\left[8(1+M_\alpha/M_\beta)\right]^{1/2}} \tag{1.10}$$

where P_t is the total pressure ($\mathrm{g\,cm^{-1}\,s^{-2}}$), Λ is the average mean free path (cm), r_0 is the pore radius (cm), $\hat{\mathbf{K}}$ is the intrinsic permeability ($\mathrm{cm^2}$), η_β^0 is the dynamic viscosity of

species β, and M is the molar mass ($\mathrm{g\,mol^{-1}}$). The BFM includes intermolecular diffusion, as well as Knudsen and viscous wall friction terms [59]. Fimrite et al. modified the BFM into the binary friction membrane model (BFM2) to specifically describe transport of water and protons in perfluorosulfonic acid (PFSA) membranes, including Nafion® [61]. Pant et al. pointed out possible shortcomings with the model when applied to transport in capillaries. This is because BFM applies Darcy's law, during its derivation, which assumes no-slip even though diffusion slip would be present in capillaries. As well, the use of Darcy's law results in the assumption that the mass and molar average velocities must equal [58]. Pant et al. went on to develop a modification to the BFM, the modified binary friction model, to correct for these issues.

When a momentum equation is included in a porous media the simplest equation to use is Darcy's law. Henry Darcy formulated Darcy's law based on experimental results in 1856 [62]. Darcy's law is expressed as:

$$\nabla P = -\eta \hat{\mathbf{K}}^{-1} \boldsymbol{v} \tag{1.11}$$

where $\boldsymbol{v}$ is the mass-averaged velocity vector ($\boldsymbol{v} = \sum w_\alpha v_\alpha$) of the mixture ($\mathrm{cm\,s^{-1}}$) and η is the dynamic viscosity of the mixture ($\mathrm{g\,cm^{-1}\,s^{-1}}$). Darcy's law describes the laminar flow of a fluid through a porous medium. Although it is based on experimental data, it has been derived from a theoretical basis by Whitaker [63].

Darcy's law clearly results in a linear relation between velocity and pressure. This result however is only valid in low flow regimes when the Reynolds number is less than 1. A correction can be applied for high velocity flow to account for the nonlinear relation between pressure and velocity. In this case, equation (1.11) is modified to become the Darcy-Forchheimer law, and it is expressed as [64, 65]:

$$\nabla P = -\eta \hat{\mathbf{K}}^{-1} \boldsymbol{v} + \hat{\boldsymbol{\beta}} \rho |\boldsymbol{v}| \boldsymbol{v} \tag{1.12}$$

where ρ is the density ($\mathrm{g\,cm^{-3}}$) and $\hat{\boldsymbol{\beta}}$ is the Forchheimer correction tensor (cm).

For high porosities, $\varepsilon > 0.6$ [66], and if viscous effects within the fluid need to be considered Brinkman's equation [67, 68] can be used:

$$\nabla P = -\eta \hat{\mathbf{K}}^{-1} \boldsymbol{v} + \widetilde{\eta} \nabla^2 \boldsymbol{v} \tag{1.13}$$

where $\widetilde{\eta}$ is the effective viscosity ($\mathrm{g\,cm^{-1}\,s^{-1}}$). The high porosity required makes this problematic for most porous media, as the porosity of porous media is typically less than 0.6 [66]. Another issue with Brinkman's equation is the effective viscosity because this is not a typical parameter known. One method to remedy this, which was done by Brinkman, is to assume that $\widetilde{\eta} \approx \eta$, however this is generally not true [66].

1.3.2 Gas Channel Effects on Mass Transport

The gas channels are used to transport the fuel and oxygen to the fuel cell and remove water from the fuel cell. By considering the channel in the domain of the simulation it allows for the ability to account for this oxygen depletion along the channel. As well, different channel designs are advantageous over others depending on what is required for increased performance. For instance, serpentine channels are beneficial when effective water removal is required [69]. Although there are benefits to including the channel in a PEFC model, the main issue is the resulting governing equations required. In a channel the transport is convection dominated, while in the porous layers transport is diffusion dominated. This makes it difficult to select appropriate governing equations to describe these two different domains for mass transport. One approach is to use different equations in the different domains, while the second is to use governing equations that are valid in all domains.

Berning et al. applied the first approach to solving a non-isothermal PEFC in 3D [70]. They considered the membrane to be impermeable so the transport in the cathode and anode was decoupled. They used the Navier-Stokes equations to describe the flow of the gas mixture in the channel. In the porous layers they argued that the momentum equation reduces to Darcy's law, and used the Maxwell-Stefan equations to describe the transport of the individual species. Berning and Djilali used this same set of transport equations when they later also included phase change in their model [71]. This approach is not limited to simplifying to Darcy's law in the porous layers. For instance, Gurau et al. modeled a 2D MEA using the Navier-Stokes in both the channel and porous layers domain [72]. In the porous layers, the Navier-Stokes equations were volume averaged and a source term for the frictional losses from Darcy's law was included. They then used Fick's diffusion to describe the transport of the individual species. What Gurau et al. did differently was have three separate transport equations for different species only valid in different domains of the PEFC. As a result there was an overlapping of two of the transport equations in the CL of the anode and cathode of the PEFC. When using governing equations only valid in specific sub-domains care must be taken when handling the internal and external boundaries [31].

Using a single set of governing equations valid in all domains is not significantly different. The main difference is that the same momentum equation is solved in all domains. In the porous layers the Navier-Stokes equations are volume averaged and an additional source term representing the frictional drag from Darcy's law is included. The Stefan-Maxwell or generalized multi-species Fick's law can be used to determine the transport of the individual species as done in [73–77].

For the two approaches above, most researchers have used commercial software for modeling a PEFC with the Navier-Stokes equations. Commercial software is typically easier

to use and implement than codes built in-house, as a coding background is not a major requirement. The problem with using commercial software is that a person may not know the exact form of the equations being solved, or how they are solved. This can lead to confusion, as researchers may write the compressible continuity equation and Cauchy momentum equation but refer to it as the incompressible Navier-Stokes equations as is the case in [70, 73, 75]. For reference, the compressible continuity equation and Cauchy momentum equation (steady-state and neglecting body forces) are:

$$\nabla \cdot (\rho \boldsymbol{v}) = 0 \tag{1.14}$$

$$\nabla \cdot (\rho \boldsymbol{v} \otimes \boldsymbol{v}) = -\nabla P + \nabla \cdot \left(\eta(\nabla \boldsymbol{v} + (\nabla \boldsymbol{v})^T)\right) \tag{1.15}$$

where ρ is the density of the mixture ($\mathrm{g\,cm^{-3}}$), while the incompressible form used in the Navier-Stokes equations (steady-state and neglecting body forces) are:

$$\nabla \cdot \boldsymbol{v} = 0 \tag{1.16}$$

$$\rho(\boldsymbol{v} \cdot \nabla)\boldsymbol{v} = -\nabla P + \eta \nabla^2 \boldsymbol{v} \tag{1.17}$$

This can make it difficult for a reader to actually know which equations were actually implemented. One example of this problem is Berning and Djilali, when using the commercial software CFX, referred to the Cauchy momentum equation as the "momentum equation for an incompressible Newtonian fluid" [71]. Commercial code is so prevalent among researchers that a review of modeling in PEFCs by Siegel only discussed OpenFOAM "as an alternative" [31]. For this reason, the use of an in-house built code, like OpenFCST, allows a researcher, and others, to know the exact form of the equations implemented.

From the above discussion, when dealing with the channel no matter which of the two approaches are selected the Navier-Stokes equations have been used in the channel to describe the gas mixture. For the porous layers then either a volume averaged form of the Navier-Stokes equations with an additional Darcy source term, or a simplified momentum equation to Darcy's law is used. The typical choices for modeling the individual species have been Fick's law or the Maxwell-Stefan equations, however the DGM or the BFM could also be used.

In 2005, Kerhof and Geboers proposed a new model to describe the multi-component transport [1, 78]. This novel approach has a continuity and momentum equation for each gas species, instead of the mixture. These equations were derived with the intent to account for phenomena that the current method cannot account for. An example, would by counter-flow types of transport, where different species are moving in opposite directions. These equations are expressed for species, α, as:

$$\frac{\partial \rho_\alpha}{\partial t} + \nabla \cdot \boldsymbol{F}_{mass_\alpha} = 0 \tag{1.18}$$

$$\frac{\partial}{\partial t}(\rho_\alpha \boldsymbol{v}_\alpha) = -\nabla \cdot \hat{\boldsymbol{F}}_{mom_\alpha} - \nabla \cdot (P_\alpha \hat{\mathbf{I}} - \hat{\boldsymbol{\tau}}_{\alpha\beta}) + \boldsymbol{F}_\alpha - \boldsymbol{D}_{therm_\alpha} + \boldsymbol{D}_\alpha \tag{1.19}$$

$$\boldsymbol{F}_{mass_\alpha} = \rho_\alpha \boldsymbol{v}_\alpha \tag{1.20}$$

$$\hat{\boldsymbol{F}}_{mom_\alpha} = \rho_\alpha \boldsymbol{v}_\alpha \otimes \boldsymbol{v}_\alpha \tag{1.21}$$

$$\hat{\boldsymbol{\tau}}_{\alpha\beta} = 2 \sum_{\beta}^{N} \frac{\eta_{\alpha\beta}}{2} \left(\nabla \boldsymbol{v}_\beta + (\nabla \boldsymbol{v}_\beta)^T - \frac{2}{3} (\nabla \cdot \boldsymbol{v}_\beta) \hat{\mathbf{I}} \right) \tag{1.22}$$

$$\boldsymbol{D}_{therm_\alpha} = \frac{1}{P_t} \sum_{\beta=1}^{N} \frac{P_\alpha P_\beta}{\mathscr{D}_{\alpha\beta}} \left(\frac{D_\alpha^T}{\rho_\alpha} - \frac{D_\beta^T}{\rho_\beta} \right) \nabla \ln T \tag{1.23}$$

$$\boldsymbol{D}_\alpha = \sum_{\beta=1}^{N} P_\alpha P_\beta \hat{\boldsymbol{D}}_{\alpha\beta} (\boldsymbol{v}_\beta - \boldsymbol{v}_\alpha) \tag{1.24}$$

$$\hat{\boldsymbol{D}}_{\alpha\beta} = (P_t \mathscr{D}_{\alpha\beta})^{-1} \hat{\mathbf{I}} \tag{1.25}$$

where t is time, $\hat{\mathbf{I}}$ is the identity tensor, $\hat{\boldsymbol{\tau}}$ is the viscous stress tensor, $\boldsymbol{F}_\alpha$ is an external body force vector field, P_t is the total pressure, D^T is the multi-component thermal diffusion coefficients, and T is the temperature. These equations are similar to the compressible continuity and Cauchy momentum equation shown earlier, however since they have to be solved for each individual species this can make the problem computationally expensive as more species are included.

This has not been met without controversy, as Mills and Chang [79] criticized the work of Salcedo-Díaz et al. for using Maxwell-slip over diffusion slip. Mills and Chang then went on to show that the classical approach, where the Navier-Stokes equations for the mixture with Fick's diffusion for the H_2O-Air, was valid. Faliagas has also criticized Kerkhof and Geboers' model [80]. As mentioned in a reply from Kerhof [81], Faliagas goes back and forth between arguing for individual momentum equations and trying to retain the classical approach. Faliagas does remark that Kerhof and Geboers' model needs to be backed by numerical experimentation to determine its validity and the possibility of numerical instability [80]. To the best of the author's knowledge no one has implemented Kerkhof and Geboers' model in a porous media, and only Salcedo-Díaz et al. [82] has applied it to a Stefan tube problem.

Based on this discussion, when including the channel into PEFC modeling there are not a large amount of options available. The approach taken by others has typically been to use the Navier-Stokes equations for the mixture and Maxwell-Stefan or Fick's law to describe the transport of the individual species. A novel model by Kerhof and Geboers has been proposed which has not been validated in porous layers or PEFC modeling. Outside of PEFC modeling, Kerkhof and Geboers' model has not been thoroughly tested to answer critical questions such as:

1. Can the equations be solved numerically?

2. What boundary conditions are appropriate?

3. Do the results make sense?

By implementing Kerhof and Geboers' model in OpenFCST it can be tested to determine its validity and numerical stability in PEFC modeling, as well as for more general applications.

1.4 Contributions

The major contributions made in this thesis towards PEFC modeling literature are:

1. Developed and validated a novel multi-component mass transport model,

2. Developed a PEFC through the channel cathode model accounting for multi-component effects and highlighted key differences with previous models,

3. Developed an along the channel compressible, multi-component model to study along the channel concentration changes.

1.5 Thesis Outline

This thesis is organized into five chapters. Chapter 1 introduced the reader to PEFCs, and described their importance, applications, and challenges. The need for accurate models describing PEFCs is highlighted. Background was provided, giving the reader a basic understanding of the operation of a PEFC. As well, an overview of the past and present research in modeling mass transport in PEFCs was discussed. Chapter 2 discusses the governing equations and simplifying assumptions. Closure relations are provided for calculation of gas species properties. Detailed derivations of the volume averaging, linearization, and finite element weak formulations required to numerically solve the governing equations are given. Chapter 3 validates the implementation of the governing equations against five benchmark tests that test all aspects of the mass transport model. Thus showing that the equations were implemented correctly and accurately predict known problems and their solutions. Chapter 4 discusses the coupling to PEFC kinetics, and simulations of the cathode are performed. These simulations compare the new mass transport model to the previously used Fick's model in OpenFCST. As well, simulations are performed along the channel. This will allow for the effects of fluid flow in channels to be included in PEFC modeling. Finally, chapter 5 presents final conclusions of this thesis and provides suggestions for future research in mass transport of PEFC modeling.

Chapter 2

Mass Transport Governing Equations

2.1 Introduction

In 2005, Kerkhof and Geboers developed a new formulation for mass transport [1, 78]. Starting from the Boltzmann equation, an extension to Cauchy's momentum equation was developed for each gaseous species in a mixture. The governing equation for species α is given by:

$$\frac{\partial \rho_\alpha}{\partial t} + \nabla \cdot \boldsymbol{F}_{mass_\alpha} = S_\alpha \tag{2.1}$$

$$\frac{\partial}{\partial t}(\rho_\alpha \boldsymbol{v}_\alpha) = -\nabla \cdot \hat{\boldsymbol{F}}_{mom_\alpha} - \nabla \cdot (P_\alpha \hat{\mathbf{I}} - \hat{\boldsymbol{\tau}}_{\alpha\beta}) + \boldsymbol{F}_\alpha - \boldsymbol{D}_{therm_\alpha} + \boldsymbol{D}_\alpha \tag{2.2}$$

$$\boldsymbol{F}_{mass_\alpha} = \rho_\alpha \boldsymbol{v}_\alpha \tag{2.3}$$

$$\hat{\boldsymbol{F}}_{mom_\alpha} = \rho_\alpha \boldsymbol{v}_\alpha \otimes \boldsymbol{v}_\alpha \tag{2.4}$$

$$\hat{\boldsymbol{\tau}}_{\alpha\beta} = 2 \sum_{\beta}^{N} \frac{\eta_{\alpha\beta}}{2} \left(\nabla \boldsymbol{v}_\beta + (\nabla \boldsymbol{v}_\beta)^T - \frac{2}{3} (\nabla \cdot \boldsymbol{v}_\beta) \hat{\mathbf{I}} \right) \tag{2.5}$$

$$\boldsymbol{D}_{therm_\alpha} = \frac{1}{P_t} \sum_{\beta=1}^{N} \frac{P_\alpha P_\beta}{\mathscr{D}_{\alpha\beta}} \left(\frac{D_\alpha^T}{\rho_\alpha} - \frac{D_\beta^T}{\rho_\beta} \right) \nabla \ln T \tag{2.6}$$

$$\boldsymbol{D}_\alpha = \sum_{\beta=1}^{N} P_\alpha P_\beta \hat{\boldsymbol{D}}_{\alpha\beta} (\boldsymbol{v}_\beta - \boldsymbol{v}_\alpha) \tag{2.7}$$

$$\hat{\boldsymbol{D}}_{\alpha\beta} = (P_t \mathscr{D}_{\alpha\beta})^{-1} \hat{\mathbf{I}} \tag{2.8}$$

where t is time, ρ is a density scalar field, $\boldsymbol{v}$ is a velocity vector field, S_α is a sink/source term, P is a pressure scalar field, $\hat{\mathbf{I}}$ is the identity tensor, $\hat{\boldsymbol{\tau}}_{\alpha\beta}$ is the viscous stress tensor (discussed below), $\boldsymbol{F}_\alpha$ is an external force vector field, P_t is the total pressure, D^T is the multi-component thermal diffusion coefficients, T is the temperature, and $\mathscr{D}_{\alpha\beta}$ is the Maxwell-Stefan diffusion coefficient between species α and β.

Equation (2.1) is the typical unsteady continuity equation, before any incompressibility assumptions are made, with an additional sink/source term to account for losing or gaining mass in the control volume. In typical mass transport conditions mass is conserved and $S_\alpha = 0$. In this situation the total mass flux along the boundary of the control volume must equal zero. For fuel cells, a chemical reaction is occurring and a sink/source term must be included. A source/sink term, S_α, is not considered in this chapter, and further discussion is left till section 4.2.

Equation (2.2) looks similar to Cauchy's momentum equation. The term on the LHS represents an accumulation of momentum with time. The first term on the RHS, $\nabla \cdot \hat{\boldsymbol{F}}_{mom_\alpha}$, is the convective term and represents the movement of the fluid particle due to the bulk motion of the fluid. The next two terms are an expansion of the stress tensor term in Cauchy's momentum equation. The first of these two terms is the hydrostatic pressure term, $P\hat{\mathbf{I}}$, which acts normal and inwards to the surface. The second of the two terms is the viscous stress tensor, $\hat{\boldsymbol{\tau}}_{\alpha\beta}$, which describes the stress due to the strain rate of the fluid in terms of viscosity and the velocity vector field. The most typical external force vector field included in models is body force, which is included when gravity is considered in the governing equations. The last two terms are new and help couple the momentum equations for each gas species. The thermal diffusion term, $\boldsymbol{D}_{therm}$, represents gas diffusion due to temperature gradients. The diffusion term, $\boldsymbol{D}_\alpha$, is the Maxwell-Stefan diffusion term for multi-component species diffusion.

2.2 Assumptions

The following assumptions were considered:

1. Steady-state conditions, i.e. all derivatives with respect to time are negligible
2. Single-phase
3. Isothermal, i.e. $\nabla \ln T \approx 0$
4. All gases can be considered ideal gases, therefore density and pressure are related by $P = \frac{\rho}{M} RT$
5. For all derivations gravity is considered the only external forces, i.e. $\boldsymbol{F}_\alpha = \rho_\alpha \boldsymbol{g}$, however gravity was neglected when running all simulations.
6. Second viscosity, ζ_α, is negligible, i.e. $\zeta_\alpha \approx 0$
7. The multi-component diffusion in gases occurs at low density, allowing for Maxwell-Stefan diffusion coefficients to be represented by binary diffusivities, i.e. $\mathscr{D}_{\alpha\beta} \approx D_{\alpha\beta}$

8. The binary diffusivity coefficients used to determine the Maxwell-Stefan diffusion coefficients can be approximated from Chapman-Enskog theory

9. The partial viscosity is dominant along the main diagonal such that $\hat{\boldsymbol{\tau}}_{\alpha\beta} \approx \hat{\boldsymbol{\tau}}_{\alpha}$.

Applying the assumptions above and simplifying, the governing equations that were implemented in OpenFCST are:

$$0 = \nabla \cdot \boldsymbol{F}_{mass_\alpha} \tag{2.9}$$

$$0 = \nabla \cdot (\hat{\boldsymbol{F}}_{mom_\alpha} + P_\alpha \hat{\mathbf{I}} - \hat{\boldsymbol{\tau}}_\alpha) - (\rho_\alpha \boldsymbol{g} + \boldsymbol{D}_\alpha) \tag{2.10}$$

$$\boldsymbol{F}_{mass_\alpha} = \rho_\alpha \boldsymbol{v}_\alpha \tag{2.11}$$

$$\hat{\boldsymbol{F}}_{mom_\alpha} = \rho_\alpha \boldsymbol{v}_\alpha \otimes \boldsymbol{v}_\alpha \tag{2.12}$$

$$\boldsymbol{D}_\alpha = \sum_{\beta=1}^{N} P_\alpha P_\beta \hat{\boldsymbol{D}}_{\alpha\beta}(\boldsymbol{v}_\beta - \boldsymbol{v}_\alpha) \tag{2.13}$$

$$\hat{\boldsymbol{D}}_{\alpha\beta} = (P_t \mathscr{D}_{\alpha\beta})^{-1} \hat{\mathbf{I}} \tag{2.14}$$

2.3 Closure Equations

2.3.1 Viscous Stress Tensor

The viscous stress tensor is represented for species α as:

$$\hat{\boldsymbol{\tau}}_\alpha = 2\eta_\alpha \nabla_s \boldsymbol{v}_\alpha + \lambda_\alpha (\nabla \cdot \boldsymbol{v}_\alpha)\hat{\mathbf{I}} \tag{2.15}$$

where λ is the bulk viscosity, η is the partial dynamic viscosity, and ∇_s is the symmetric gradient defined as $\nabla_s = \frac{1}{2}\left(\nabla + \nabla^T\right)$. It should be noted that the ∇^T term in the symmetric gradient does not imply that the gradient operator is transposed. Rather, the gradient of the velocity vector field is transposed; i.e. $\nabla^T \boldsymbol{v}_\alpha = (\nabla \boldsymbol{v}_\alpha)^T$. As mentioned in section 2.2, since the second viscosity, ζ, is assumed negligible then the relation between second viscosity, bulk viscosity, and dynamic viscosity becomes:

$$\cancelto{0}{\zeta_\alpha} = \lambda_\alpha + \frac{2}{3}\eta_\alpha \tag{2.16}$$

$$\lambda_\alpha = -\frac{2}{3}\eta_\alpha \tag{2.17}$$

This allows for the viscous stress tensor to be only a function of the partial dynamic viscosity and the velocity vector field, and is expressed as:

$$\hat{\boldsymbol{\tau}}_\alpha = 2\eta_\alpha \nabla_s \boldsymbol{v}_\alpha - \frac{2}{3}\eta_\alpha (\nabla \cdot \boldsymbol{v}_\alpha)\hat{\mathbf{I}} \tag{2.18}$$

2.3.2 Diffusion Coefficient

Chapman-Engskog theory was used to determine accurately the Maxwell-Stefan diffusion coefficients [45]. A modified form of this equation presented by Bird [45] is used in OpenFCST. This equation was modified to account for a different choice of units for input variables and is expressed as [45]:

$$D_{\alpha\beta} = 188.29\, T^{3/2} \frac{\sqrt{1/M_\alpha + 1/M_\beta}}{P_t\, \sigma_{\alpha\beta}^2\, \Omega_D^*} \tag{2.19}$$

$$\sigma_{\alpha\beta} = \frac{1}{2}(\sigma_\alpha + \sigma_\beta) \tag{2.20}$$

where $D_{\alpha\beta}$ is the diffusion coefficient ($\mathrm{cm^2\,s^{-1}}$), M is the molar mass ($\mathrm{g\,mol^{-1}}$), P_t is the absolute total pressure (Pa), σ_α is the characteristic diameter of the molecule known as the collision diameter [45], and Ω_D^* is the diffusion collision integral. Ω_D^* can be considered a correction factor from assuming an idealized rigid-sphere molecular model. Due to the complexity of the integral expression for Ω_D^* it is often easier to interpolate from tabulated values, like those given by Bird [45]. Neufeld et al. has curve fitted this data to the following equation [83]:

$$\Omega_D^* = \frac{1.06036}{(T^*)^{0.15610}} + \frac{0.19300}{\exp(0.47635\, T^*)} + \frac{1.03587}{\exp(1.52996\, T^*)} + \frac{1.76474}{\exp(3.89411\, T^*)} \tag{2.21}$$

$$T_{\alpha\beta}^* = \frac{Tk}{\epsilon_{\alpha\beta}} \tag{2.22}$$

$$\epsilon_{\alpha\beta} = \sqrt{\epsilon_\alpha \epsilon_\beta} \tag{2.23}$$

where $T_{\alpha\beta}^*$ is the reduced temperature between species α and β, k is the Boltzmann constant ($1.381 \times 10^{-23}\,\mathrm{J\,K^{-1}}$), and ϵ is the maximum attractive energy between two molecules [45] (J). Values for ϵ are typically reported in relation to the Boltzmann constant in the form ϵ/k.

Under normal circumstances, equation (2.19) is a function of pressure and because the species are assumed to be ideal gases then the diffusion coefficient is a function of density. However, if equation (2.19) is substituted into equation (2.14) as follows:

$$\hat{\boldsymbol{D}}_{\alpha\beta} = (P_t \mathscr{D}_{\alpha\beta})^{-1} \hat{\mathbf{I}} \tag{2.24}$$

$$= \left(P_t\, 188.29\, T^{3/2} \frac{\sqrt{1/M_\alpha + 1/M_\beta}}{P_t\, \sigma_{\alpha\beta}^2\, \Omega_D^*} \right)^{-1} \hat{\mathbf{I}} \tag{2.25}$$

$$= \left(188.29\, T^{3/2} \frac{\sqrt{1/M_\alpha + 1/M_\beta}}{\sigma_{\alpha\beta}^2\, \Omega_D^*} \right)^{-1} \hat{\mathbf{I}} \tag{2.26}$$

then the pressure, and by extension density, cancels out.

2.3.3 Viscosity Model

Kerkhof and Geboers emphasize that the partial dynamic viscosity, η_α, is not the same as the dynamic viscosity for a pure substance, η_α^0 [78]. There are multiple methods for calculating the dynamic viscosity of a mixture [84–86], however not much has been done to determine the partial viscosity of the individual components in a mixture. Using Kerkhof and Geboers' assumption that the partial viscosities of the components are additive towards the dynamic viscosity of the mixture, then previous methods for calculating the dynamic viscosity of a mixture can typically be used. Two different models are presented here that were implemented in OpenFCST. One proposed by Wilke [87], that is simple to implement and fairly accurate. The second was derived by Kerkhof and Geboers [1]. It is more accurate, but also more computationally expensive.

2.3.3.1 Wilke's Model

Kerkhof and Geboers recommended using the model developed by Wilke for determining the partial viscosity of a mixture [78]. Since the partial viscosities are assumed to be additive towards the overall mixture partial viscosity, the summation over species α is removed from Wilke's model [87]. This results in the following partial viscosity for species α:

$$\eta_\alpha = \frac{x_\alpha \eta_\alpha^0}{\sum_{\beta=1}^{N} x_\beta \xi_{\alpha\beta}} \tag{2.27}$$

$$\xi_{\alpha\beta} = \frac{\left[1 + (\eta_\alpha^0/\eta_\beta^0)^{1/2}(M_\beta/M_\alpha)^{1/4}\right]^2}{\left[8(1 + M_\alpha/M_\beta)\right]^{1/2}} \tag{2.28}$$

where x is the molar fraction, and M is the molar mass. Since the governing equations use density instead of molar fraction as a solution variable, the following relation can be used to transform the equation into a function of density:

$$x_\alpha = \frac{C_\alpha}{C_t} = \frac{\rho_\alpha M}{\rho M_\alpha} \tag{2.29}$$

where C_α and C_t are the species and total concentration ($\mathrm{mol\,cm^{-3}}$) respectively. This replaces the molar fraction with the unknown density scalar field from the governing equations. Thus, the partial viscosity will be approximated as follows:

$$\eta_\alpha = \frac{\rho_\alpha \eta_\alpha^0}{M_\alpha \sum_{\beta=1}^{N} \frac{\rho_\beta}{M_\beta} \xi_{\alpha\beta}} \tag{2.30}$$

$$\xi_{\alpha\beta} = \frac{\left[1 + (\eta_\alpha^0/\eta_\beta^0)^{1/2}(M_\beta/M_\alpha)^{1/4}\right]^2}{\left[8(1 + M_\alpha/M_\beta)\right]^{1/2}} \tag{2.31}$$

where ρ_α is the density of species α.

Wilke's viscosity model neglects second-order terms, and with the exception of the hydrogen-argon mixture the average deviation from experimental points is 0.49% [87]. From other researchers it has been found that Wilke's viscosity model is fairly accurate and only loses accuracy for mixtures containing hydrogen [84, 86]. Poling [86] goes further stating that it looses accuracy when $M_\alpha >> M_\beta$ and $\eta^0_\alpha >> \eta^0_\beta$. For this reason when simulating an anode or a full membrane electrode assembly (MEA) of a PEFC another method should possibly be considered.

To determine the dynamic viscosity of each of the individual species, Chapman-Engskog theory will be used. This equation is expressed as [45]:

$$\eta^0 = 2.6693 \times 10^{-5} \frac{\sqrt{MT}}{\sigma^2 \, \Omega^*_\eta} \tag{2.32}$$

where η^0 is the dynamic viscosity of the individual species ($\mathrm{g\,s^{-1}\,cm^{-1}}$), Ω^*_η is the viscosity collision integral. Like Ω^*_D, values for Ω^*_η are tabulated by Bird [45], and Neufeld et al. has curve fitted this data to the following equation [83]:

$$\Omega^*_\eta = \frac{1.16145}{(T^*)^{0.14874}} + \frac{0.52487}{\exp(0.77320\,T^*)} + \frac{2.16178}{\exp(2.43787\,T^*)} \tag{2.33}$$

$$T^* = \frac{Tk}{\epsilon} \tag{2.34}$$

Since this equation is for determining the dynamic viscosity of a pure substance, then it is not related to any of the species in the mixture. As a result, no type of averaging for the variables σ and ϵ/k between the different species is required.

2.3.3.2 Kerkhof and Geboers' Model

Kerkhof and Geboers derived a set of equations for the partial viscosity from the $\boldsymbol{B}$-terms in the perturbation function, ϕ, for the Boltzmann equation [1, 88]. These equations are similar to those derived by Hirschfelder et al. [85] in that they both utilize the Lennard-Jones constants and the collision integrals, as both require the inversion of a matrix in order to find the partial viscosities. These equations are:

$$\hat{\boldsymbol{P}}\boldsymbol{\eta} = \mathbf{1} \tag{2.35}$$

$$P_{\alpha\alpha} = \frac{2}{kT}\left(\frac{4}{5}\Omega^{(2,2)}_{\alpha\alpha} + \frac{16M_\alpha}{15\rho_\alpha}\sum_{\beta\neq\alpha}^{N}\frac{\rho_\beta}{(M_\alpha+M_\beta)^2}\left(5M_\alpha\Omega^{(1,1)}_{\alpha\beta} + \frac{3}{2}M_\beta\Omega^{(2,2)}_{\alpha\beta}\right)\right) \tag{2.36}$$

$$P_{\alpha\beta} = -\frac{2}{kT}\left(\frac{16}{15}\left(\frac{M_\alpha M_\beta}{(M_\alpha+M_\beta)^2}\right)\left(5\Omega^{(1,1)}_{\alpha\beta} - \frac{3}{2}\Omega^{(2,2)}_{\alpha\beta}\right)\right) \tag{2.37}$$

where $\boldsymbol{\eta}$ is a vector of the partial viscosities ($\mathrm{kg\,s^{-1}\,m^{-1}}$), $\mathbf{1}$ is a vector of ones, M is the molar mass ($\mathrm{kg\,mol^{-1}}$), ρ is the density, and $\Omega_{\alpha\beta}^{(\ell,s)}$ are the collision integrals. The collision integrals, $\Omega_{\alpha\beta}^{(\ell,s)}$, are expressed as:

$$\Omega_{\alpha\beta}^{(\ell,s)} = \Omega_{\alpha\beta}^{*(\ell,s)} \left[\Omega_{\alpha\beta}^{(\ell,s)}\right]_{rs} \tag{2.38}$$

$$\left[\Omega_{\alpha\beta}^{(\ell,s)}\right]_{rs} = \sqrt{\frac{kT}{2\pi\mu_{\alpha\beta}}} \left(\frac{(s+1)!}{2}\right) \left[Q_{\alpha\beta}^{\ell}\right]_{rs} \tag{2.39}$$

$$\left[Q_{\alpha\beta}^{\ell}\right]_{rs} = \left(1 - \frac{1}{2}\left(\frac{1+(-1)^{\ell}}{1+\ell}\right)\right)\pi\sigma_{\alpha\beta}^{2} \tag{2.40}$$

$$\sigma_{\alpha\beta} = \frac{1}{2}\left(\sigma_{\alpha} + \sigma_{\beta}\right) \tag{2.41}$$

$$\mu_{\alpha\beta} = \frac{M_{\alpha}M_{\beta}}{N_A(M_{\alpha}+M_{\beta})} \tag{2.42}$$

where σ is the collision diameter (m), $\mu_{\alpha\beta}$ is the reduced mass between species α and β, and N_A is Avogadro's constant ($6.022 \times 10^{23}\,\mathrm{molecule\,mol^{-1}}$). The subscript rs stands for rigid spheres and signifies that $\left[\Omega_{\alpha\beta}^{(\ell,s)}\right]_{rs}$ is derived assuming that the particles are treated as rigid spheres. As a result, $\Omega_{\alpha\beta}^{*(\ell,s)}$ is a correction factor to account for the differences in behaviour from this assumption. Similarly to Ω_D^* and Ω_η^*, values for $\Omega_{\alpha\beta}^*$ are tabulated by Hirschfelder et al. [85]. Kerkhof and Geboers have curve fitted Hirschfelder's data using a Neufeld-type equation [1] as follows:

$$\Omega_{\alpha\beta}^{*(\ell,s)} = a\left(T_{\alpha\beta}^{*}\right)^{-b} + c\exp\left(-dT_{\alpha\beta}^{*}\right) \tag{2.43}$$

$$T_{\alpha\beta}^{*} = \frac{Tk}{\epsilon_{\alpha\beta}} \tag{2.44}$$

$$\epsilon_{\alpha\beta} = \sqrt{\epsilon_{\alpha}\epsilon_{\beta}} \tag{2.45}$$

The values for the constants in equation (2.43) for $\Omega_{\alpha\beta}^{*(1,1)}$ and $\Omega_{\alpha\beta}^{*(2,2)}$ are shown in Table 2.1.

Table 2.1 – Constants for empirical $\Omega_{\alpha\beta}^{*(\ell,s)}$ equations (Ref [1])

Variable	$\Omega_{\alpha\beta}^{*(1,1)}$		$\Omega_{\alpha\beta}^{*(2,2)}$	
	$0.3 \le T^* < 2.5$	$2.5 \le T^* \le 400$	$0.3 \le T^* < 2.5$	$2.5 \le T^* \le 400$
a	1.340794	1.066993	26.425725	1.151508
b	0.326244	0.157384	0.045563	0.145812
c	1.546648	0.424013	-25.232304	0.437374
d	2.768179	0.698873	0.016075	0.670219

2.3.3.3 Comparison of Results

Hirschfelder et al. [85] has provided experimental data at various temperatures for an Argon-Neon and Argon-Neon-Helium mixture. This data will be used to validate that both viscosity models have been implemented correctly in OpenFCST and results will be compared. Table 2.2 shows the gas properties that these two models require for calculating the partial viscosities of the mixtures.

Table 2.2 – Gas properties

Property	Argon	Neon	Helium	Units	Reference
M	39.948×10^{-3}	20.183×10^{-3}	$4.002\,602 \times 10^{-3}$ [89]	$\mathrm{kg\,mol^{-1}}$	[45]
σ	3.432×10^{-10}	2.789×10^{-10}	2.576×10^{-10}	m	[85]
ε/k	124	35.7	10.2	K	[85]

Figures 2.1, 2.2, and 2.3 show the partial viscosity calculated using Wilke and Kerkhof and Geboers' models at various temperatures. The experimental values are also shown for the dynamic viscosity of the mixture. Both models appear to accurately predict the dynamic viscosity of the mixture. As well, the partial viscosity of the mixture intuitively shows what one would expect. That the partial viscosity of the mixture approaches the dynamic viscosity as the mole fractions approach 1.

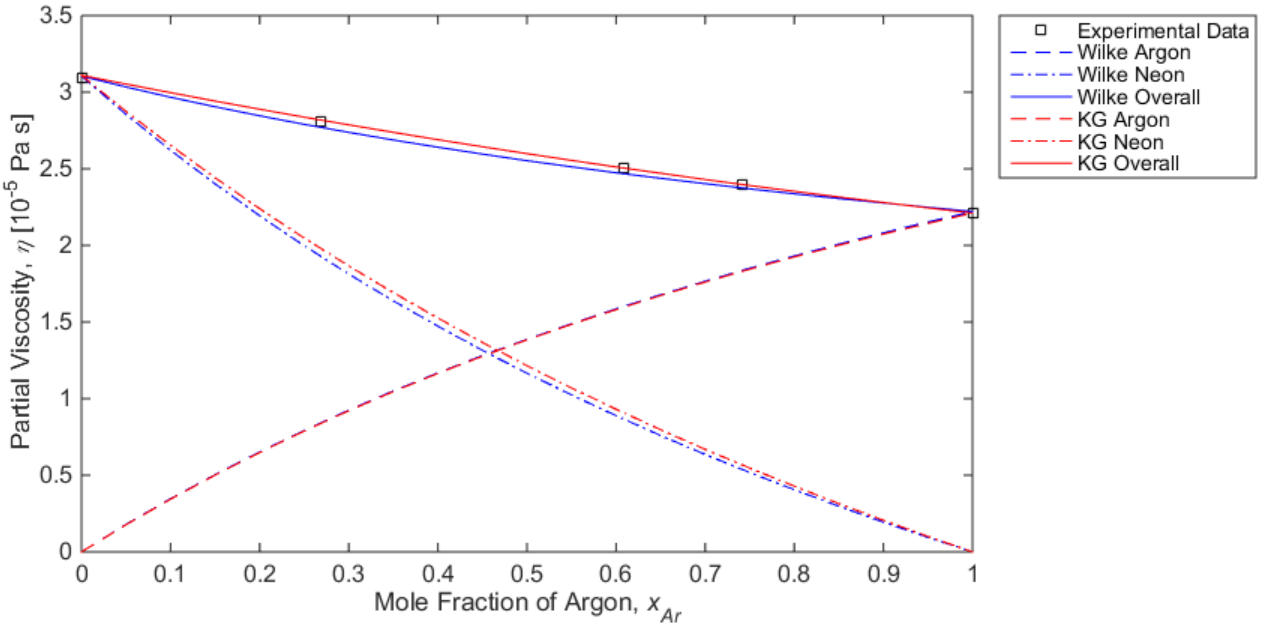

Figure 2.1 – Partial viscosity of Ar-Ne mixture at T=293.16 K

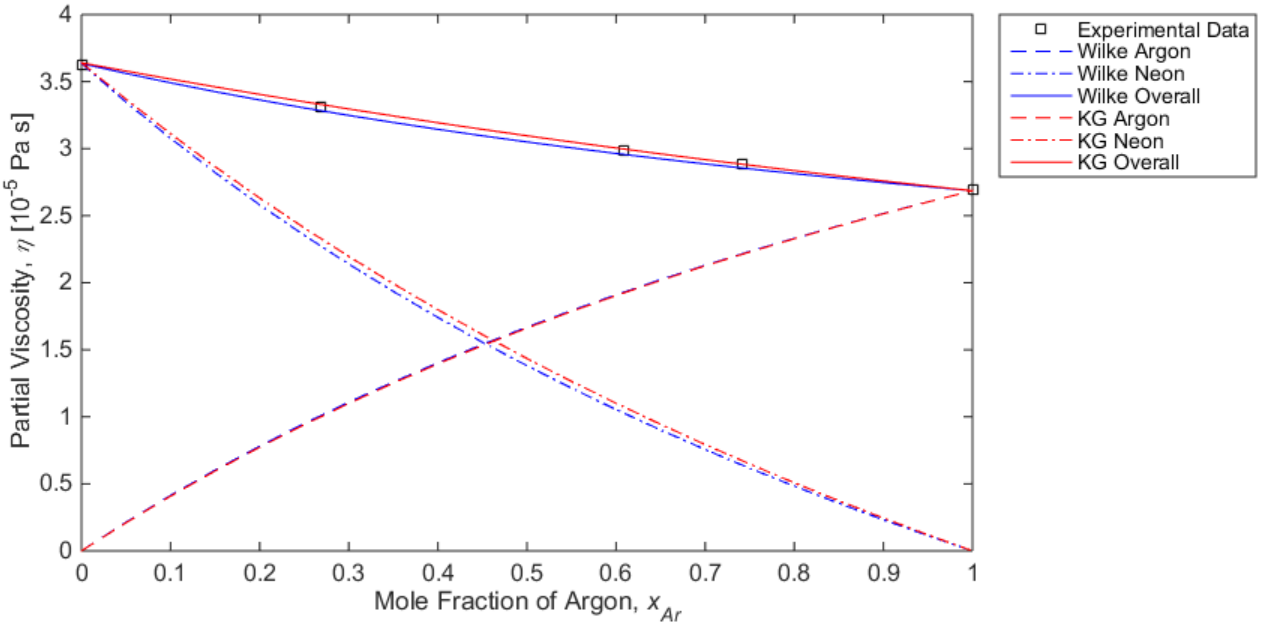

Figure 2.2 – Partial viscosity of Ar-Ne mixture at T=373.16 K

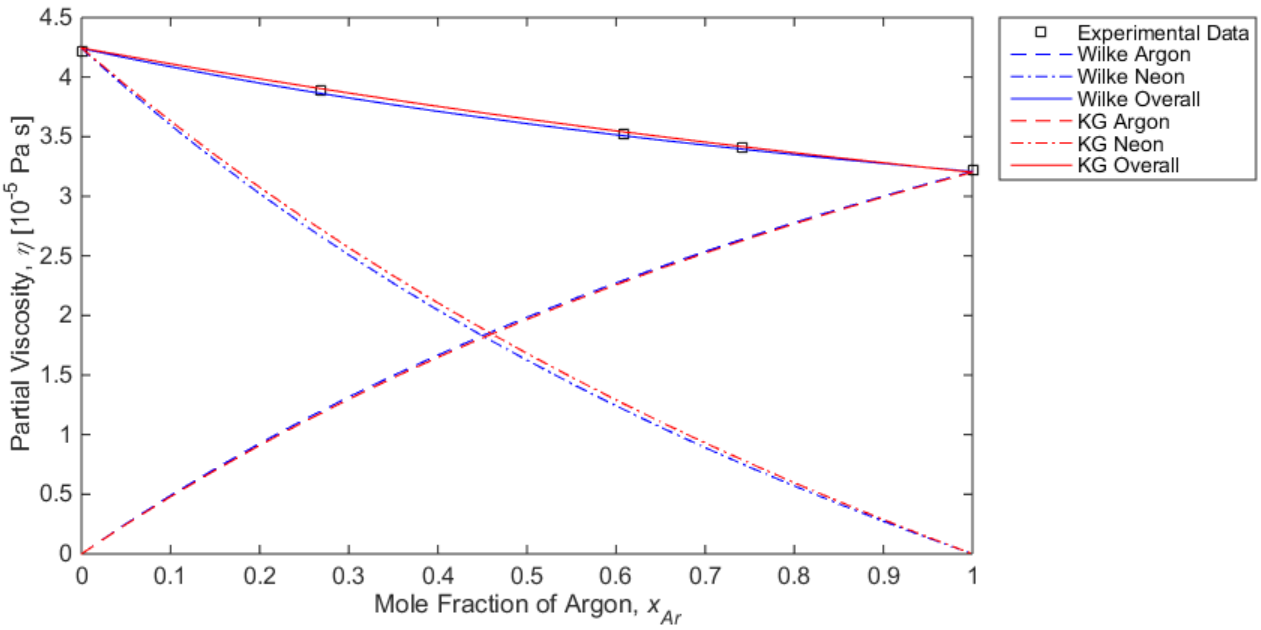

Figure 2.3 – Partial viscosity of Ar-Ne mixture at T=473.16 K

To properly compare the accuracy of each model the dynamic viscosity of the mixture was calculated at the same molar fractions as the experimental partial viscosity. Then an the least squares error was calculated assuming the experimental values are the exact solution. Table 2.3 shows the overall partial viscosities compared with the experimental values at various temperatures. From this the least squares error for Wilke and Kerkhof and Geboers' models are tabulated in Table 2.4. With the exception of the case when the temperature is 473.16 K, Kerkhof and Geboers' model was always more accurate than Wilke's. Both Wilke and Kerkhof and Geboers' models show an increased error from the 373.16 K to 473.16 K. In the case of a PEFC this should not be a problem as temperatures do not typically go above 373.15 K.

Table 2.3 – Dynamic viscosity of an *Ar-Ne* mixture at various temperatures

T (K)	x_{Ar}	0.0000	0.2680	0.6091	0.7421	1.000
293.16	Experimental	3.092	2.808	2.504	2.401	2.213
	Wilke	3.105	2.771	2.468	2.374	2.221
	KG	3.110	2.819	2.504	2.397	2.211
373.16	Experimental	3.623	3.313	2.990	2.885	2.693
	Wilke	3.635	3.283	2.957	2.855	2.686
	KG	3.640	3.330	2.997	2.883	2.686
473.16	Experimental	4.220	3.890	3.529	3.413	3.222
	Wilke	4.241	3.864	3.508	3.395	3.208
	KG	4.245	3.905	3.541	3.417	3.202

Table 2.4 – Error in dynamic viscosity of the *Ar-Ne* mixture at various temperatures

T (K)	Least Squares Error	
	Wilke	KG
293.16	0.061×10^{-5}	0.022×10^{-5}
373.16	0.055×10^{-5}	0.026×10^{-5}
473.16	0.390×10^{-5}	0.443×10^{-5}

Table 2.5 shows the dynamic viscosity of the mixture at various temperatures for different molar fractions of Argon and Neon. If the values for Kerkhof and Geboers' model calculated in this work and by Kerkhof and Geboers themselves [1] are compared they are nearly identical for all cases. This validates the equations implemented in OpenFCST to calculate Kerkhof and Geboers' partial viscosity model. Table 2.6 shows the least squares error for Wilke and Kerkhof and Geboers' model. For all cases Kerkhof and Geboers' partial viscosity model has a smaller error and is consistently around 0.025×10^{-5}. On the other hand, Wilke's model appears to have a steadily increasing error.

Table 2.5 – Dynamic viscosity of an *Ar-Ne-He* mixture at various temperatures

T (K)	x_{Ar}	x_{Ne}	Experimental	Wilke	KG
293	0.2670	0.5576	2.740	2.708	2.736
	0.3213	0.3193	2.569	2.563	2.575
	0.5851	0.2166	2.411	2.411	2.432
	0.2382	0.2189	2.504	2.524	2.512
373	0.2670	0.5576	3.237	3.213	3.233
	0.3213	0.3193	3.044	3.052	3.050
	0.5851	0.2166	2.886	2.894	2.910
	0.2382	0.2189	2.957	2.999	2.966
473	0.2670	0.5576	3.790	3.785	3.792
	0.3213	0.3193	3.574	3.605	3.582
	0.5851	0.2166	3.415	3.437	3.439
	0.2382	0.2189	3.470	3.537	3.477

Table 2.6 – Error in dynamic viscosity of an *Ar-Ne-He* mixture at various temperatures

T (K)	Least Squares Error	
	Wilke	KG
293	0.038×10^{-5}	0.023×10^{-5}
373	0.050×10^{-5}	0.027×10^{-5}
473	0.077×10^{-5}	0.027×10^{-5}

2.4 Representative Elementary Volume Averaging

2.4.1 Introduction

A PEFC has five distinct layers: the channel, GDL, MPL, CL, and PEM. The GDL, MPL, and CL being porous materials require a representative elementary volume (REV) averaging form of the governing equations. Consider the small porous elementary volume shown in Figure 2.4, where there is a fluid domain and a solid domain. If one were to model the fluid flow through this porous medium it would be computationally challenging. This is because a highly refined mesh that accurately reflects the porous structure and necessary boundary conditions would be required. Thus, resulting in a computationally expensive simulation. Instead, an approximate solution can be obtained by volume averaging the equations in the domain [90].

The two most common choices for REV averaging are the phase and intrinsic average. For the phase average, the field variables are averaged over the entire domain including the solid domain. While for the intrinsic average, the field variables are averaged over the domain that the fluid exists in. The phase and intrinsic REV averages are mathematically defined

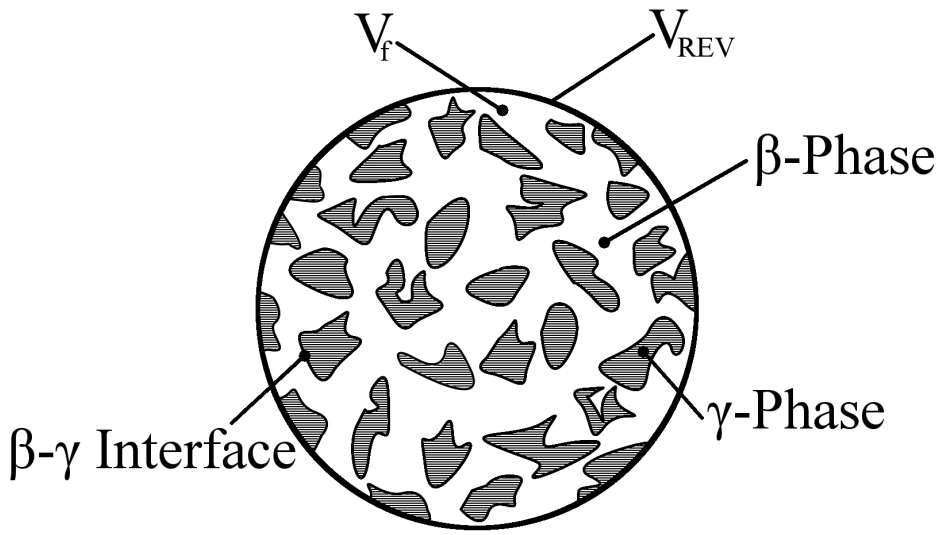

Figure 2.4 – Representation of REV averaging

for a given function ϕ respectively as [90]:

$$\langle \phi \rangle = \frac{1}{V_{REV}} \int_{V_f} \phi \, \mathrm{d}V \tag{2.46}$$

$$\langle \phi \rangle^f = \frac{1}{V_f} \int_{V_f} \phi \, \mathrm{d}V \tag{2.47}$$

where V_{REV} is the total volume of the REV and V_f is the volume of the fluid in the REV. These two REV averages can be related to each other through the definition of porosity, ε, as follows:

$$\langle \phi \rangle = \varepsilon \langle \phi \rangle^f \tag{2.48}$$

$$\varepsilon = \frac{V_f}{V_{REV}} \tag{2.49}$$

Zingan [91] determined that the best choice is the combination $(\langle \rho_\alpha \rangle, \langle \boldsymbol{v}_\alpha \rangle^f)$. This is because it generates a stable non-oscillatory numerical solution with no jumps in the solution variables across the interface.

To apply this REV averaging to the governing equations the following identities are useful

[92–94]:

$$\langle A\phi + B\psi\rangle = A\langle\phi\rangle + B\langle\psi\rangle \tag{2.50}$$

$$\langle A\phi + B\psi\rangle^f = A\langle\phi\rangle^f + B\langle\psi\rangle^f \tag{2.51}$$

$$\langle\phi\psi\rangle \approx \frac{1}{\varepsilon}\langle\phi\rangle\langle\psi\rangle \tag{2.52}$$

$$\langle\phi\psi\rangle^f \approx \frac{1}{\varepsilon}\langle\phi\rangle^f\langle\psi\rangle^f \tag{2.53}$$

$$\langle\nabla\phi\rangle = \nabla\langle\phi\rangle + \frac{1}{V_{REV}}\oint_{A_{\beta\gamma}} \phi\boldsymbol{n}_{\beta\gamma}\,\mathrm{d}A \tag{2.54}$$

$$\langle\nabla\cdot\boldsymbol{F}\rangle = \nabla\cdot\langle\boldsymbol{F}\rangle + \frac{1}{V_{REV}}\oint_{A_{\beta\gamma}} \boldsymbol{F}\cdot\boldsymbol{n}_{\beta\gamma}\,\mathrm{d}A \tag{2.55}$$

$$\langle\nabla\boldsymbol{F}\rangle = \nabla\langle\boldsymbol{F}\rangle + \frac{1}{V_{REV}}\oint_{A_{\beta\gamma}} \boldsymbol{F}\otimes\boldsymbol{n}_{\beta\gamma}\,\mathrm{d}A \tag{2.56}$$

$$\langle\nabla\cdot\hat{\boldsymbol{T}}\rangle = \nabla\cdot\langle\hat{\boldsymbol{T}}\rangle + \frac{1}{V_{REV}}\oint_{A_{\beta\gamma}} \hat{\boldsymbol{T}}\boldsymbol{n}_{\beta\gamma}\,\mathrm{d}A \tag{2.57}$$

where ϕ and ψ are scalar fields, $\boldsymbol{F}$ is a vector field, $\hat{\boldsymbol{T}}$ is a tensor field, and $A_{\beta\gamma}$ and $\boldsymbol{n}_{\beta\gamma}$ are the surface area and normal vector of the β-γ interface within the control volume respectively. Expressed more simply the β-γ interface is the interface between the fluid and solid inside the control volume. As such, when the vector field, $\boldsymbol{F}$, represents a velocity vector field then by the no penetration and no-slip assumption this boundary integral must be zero. A proof for equation (2.54) can be found in [95] or [93]. The technique used in [95] or [93] can also be used to prove equations (2.55) to (2.57).

2.4.2 Multi-Component Mass Transport Model

As discussed by Zingan [91], after averaging the governing equations become:

$$0 = \nabla\cdot\langle\boldsymbol{F}_{mass_\alpha}\rangle \tag{2.58}$$

$$\begin{aligned} 0 = \nabla\cdot\left(\langle\hat{\boldsymbol{F}}_{mom_\alpha}\rangle + \langle P_\alpha\rangle\hat{\mathbf{I}} - \langle\hat{\boldsymbol{\tau}}_\alpha\rangle\right) + \frac{1}{V_{REV}}\oint_{A_{\beta\gamma}}\left(P_\alpha\hat{\mathbf{I}} - \hat{\boldsymbol{\tau}}_\alpha\right)\boldsymbol{n}_{\beta\gamma}\,\mathrm{d}A \\ - \left(\langle\rho_\alpha\rangle\boldsymbol{g} + \langle\boldsymbol{D}_\alpha\rangle\right) \end{aligned} \tag{2.59}$$

$$\langle\boldsymbol{F}_{mass_\alpha}\rangle = \langle\rho_\alpha\rangle\langle\boldsymbol{v}_\alpha\rangle^f \tag{2.60}$$

$$\langle\hat{\boldsymbol{F}}_{mom_\alpha}\rangle = \langle\rho_\alpha\rangle\langle\boldsymbol{v}_\alpha\rangle^f\otimes\langle\boldsymbol{v}_\alpha\rangle^f \tag{2.61}$$

$$\langle P_\alpha\rangle = \langle\rho_\alpha\rangle\frac{RT_{mix}}{M_\alpha} \tag{2.62}$$

$$\langle\boldsymbol{D}_\alpha\rangle = \frac{1}{\varepsilon}\sum_{\beta=1}^{N}\langle P_\alpha\rangle\langle P_\beta\rangle\hat{\boldsymbol{D}}_{\alpha\beta}(\langle\boldsymbol{v}_\beta\rangle^f - \langle\boldsymbol{v}_\alpha\rangle^f) \tag{2.63}$$

Based on the work of Zingan [91] a derivation for equation (2.58) and (2.59) can be found in Appendix A.

Whitaker [90] proposed a closure form for the surface integral in equation (2.59) by approximating it with Darcy's Law. In a PEFC there is a possibility to have high velocity flows, the extended Darcy-Forchheimer law was used instead:

$$\frac{1}{V_{REV}}\oint_{A_{\beta\gamma}}(P_\alpha\hat{\mathbf{I}}-\hat{\boldsymbol{\tau}}_\alpha)\boldsymbol{n}_{\beta\gamma}\,\mathrm{d}A \approx \langle\eta_\alpha\rangle\hat{\mathbf{K}}^{-1}\varepsilon\langle\boldsymbol{v}_\alpha\rangle + \hat{\boldsymbol{\beta}}\langle\rho_\alpha\rangle|\varepsilon\langle\boldsymbol{v}_\alpha\rangle|\varepsilon\langle\boldsymbol{v}_\alpha\rangle \tag{2.64}$$

where $\hat{\mathbf{K}}^{-1}$ is the inverse of the permeability tensor (cm^2) and $\hat{\boldsymbol{\beta}}$ is the nonlinear Forchheimer correction tensor (cm). The Darcy-Forchheimer law is an extension of typical Darcy flow. Since Darcy's law is only valid for low flow regimes, the additional Forchheimer correction tensor allows for more accuracy to better reflect high velocity flows through a porous medium. This results in the following REV averaged governing equations for a porous domain:

$$0 = \nabla\cdot\langle\boldsymbol{F}_{mass_\alpha}\rangle \tag{2.65}$$

$$0 = \nabla\cdot\left(\langle\hat{\boldsymbol{F}}_{mom_\alpha}\rangle + \langle P_\alpha\rangle\hat{\mathbf{I}} - \langle\hat{\boldsymbol{\tau}}_\alpha\rangle\right) - \left(\langle\boldsymbol{F}_{por_\alpha}\rangle + \langle\rho_\alpha\rangle\boldsymbol{g} + \langle\boldsymbol{D}_\alpha\rangle\right) \tag{2.66}$$

$$\langle\boldsymbol{F}_{mass_\alpha}\rangle = \langle\rho_\alpha\rangle\langle\boldsymbol{v}_\alpha\rangle^f \tag{2.67}$$

$$\langle\hat{\boldsymbol{F}}_{mom_\alpha}\rangle = \langle\rho_\alpha\rangle\langle\boldsymbol{v}_\alpha\rangle^f\otimes\langle\boldsymbol{v}_\alpha\rangle^f \tag{2.68}$$

$$\langle P_\alpha\rangle = \langle\rho_\alpha\rangle\frac{RT_{mix}}{M_\alpha} \tag{2.69}$$

$$\langle\boldsymbol{F}_{por_\alpha}\rangle = -\langle\eta_\alpha\rangle\hat{\mathbf{K}}^{-1}\varepsilon\langle\boldsymbol{v}_\alpha\rangle^f - \hat{\boldsymbol{\beta}}\langle\rho_\alpha\rangle|\varepsilon\langle\boldsymbol{v}_\alpha\rangle^f|\varepsilon\langle\boldsymbol{v}_\alpha\rangle^f \tag{2.70}$$

$$\langle\boldsymbol{D}_\alpha\rangle = \frac{1}{\varepsilon}\sum_{\beta=1}^{N}\langle P_\alpha\rangle\langle P_\beta\rangle\hat{\boldsymbol{D}}_{\alpha\beta}(\langle\boldsymbol{v}_\beta\rangle^f - \langle\boldsymbol{v}_\alpha\rangle^f) \tag{2.71}$$

2.4.3 Closure Equations

2.4.3.1 Viscous Stress Tensor

Considering the stress tensor term, first equation (2.57) is applied as follows:

$$\langle\nabla\cdot\hat{\boldsymbol{\tau}}_\alpha\rangle = \nabla\cdot\langle\hat{\boldsymbol{\tau}}_\alpha\rangle + \frac{1}{V_{REV}}\oint_{A_{\beta\gamma}}\hat{\boldsymbol{\tau}}_\alpha\boldsymbol{n}_{\beta\gamma}\,\mathrm{d}A \tag{2.72}$$

Opening the stress tensor term, equations (2.50) and (2.52) can now be applied:

$$\langle\hat{\boldsymbol{\tau}}_\alpha\rangle = 2\langle\eta_\alpha\nabla_s\boldsymbol{v}_\alpha\rangle - \frac{2}{3}\langle\eta_\alpha\left(\nabla\cdot\boldsymbol{v}_\alpha\right)\hat{\mathbf{I}}\rangle \tag{2.73}$$

$$\approx \frac{2}{\varepsilon}\langle\eta_\alpha\rangle\langle\nabla_s\boldsymbol{v}_\alpha\rangle - \frac{2}{3\varepsilon}\langle\eta_\alpha\rangle\langle\nabla\cdot\boldsymbol{v}_\alpha\rangle\hat{\mathbf{I}} \tag{2.74}$$

Equations (2.56) and (2.55) can then be applied as follows:

$$\langle \hat{\boldsymbol{\tau}}_\alpha \rangle = \frac{2}{\varepsilon}\langle \eta_\alpha \rangle \left(\nabla_s \langle \boldsymbol{v}_\alpha \rangle + \frac{1}{V_{REV}} \oint_{A_{\beta\gamma}} \boldsymbol{v}_\alpha \otimes \boldsymbol{n}_{\beta\gamma} \, \mathrm{d}A \right) - \frac{2}{3\varepsilon}\langle \eta_\alpha \rangle \left(\nabla \cdot \langle \boldsymbol{v}_\alpha \rangle + \frac{1}{V_{REV}} \oint_{A_{\beta\gamma}} \boldsymbol{v}_\alpha \cdot \boldsymbol{n}_{\beta\gamma} \, \mathrm{d}A \right) \hat{\mathbf{I}} \quad (2.75)$$

Assuming no-slip along the β-γ interface in the REV and no penetration is assumed along the boundary of the porous medium control volume, then both surface integrals in equation (2.75) must be zero. Finally, the velocity vector field must be converted to an intrinsic average like so:

$$\langle \hat{\boldsymbol{\tau}}_\alpha \rangle = \frac{2}{\varepsilon}\langle \eta_\alpha \rangle \nabla_s \langle \boldsymbol{v}_\alpha \rangle - \frac{2}{3\varepsilon}\langle \eta_\alpha \rangle \nabla \cdot \langle \boldsymbol{v}_\alpha \rangle \hat{\mathbf{I}} \quad (2.76)$$

$$= 2\langle \eta_\alpha \rangle \nabla_s \langle \boldsymbol{v}_\alpha \rangle^f - \frac{2}{3}\langle \eta_\alpha \rangle \nabla \cdot \langle \boldsymbol{v}_\alpha \rangle^f \hat{\mathbf{I}} \quad (2.77)$$

In summary,

$$\langle \nabla \cdot \hat{\boldsymbol{\tau}}_\alpha \rangle = \nabla \cdot \langle \hat{\boldsymbol{\tau}}_\alpha \rangle + \frac{1}{V_{REV}} \oint_{A_{\beta\gamma}} \hat{\boldsymbol{\tau}}_\alpha \boldsymbol{n}_{\beta\gamma} \, \mathrm{d}A \quad (2.78)$$

$$= \nabla \cdot \left(2\langle \eta_\alpha \rangle \nabla_s \langle \boldsymbol{v}_\alpha \rangle^f - \frac{2}{3}\langle \eta_\alpha \rangle \nabla \cdot \langle \boldsymbol{v}_\alpha \rangle^f \hat{\mathbf{I}} \right) + \frac{1}{V_{REV}} \oint_{A_{\beta\gamma}} \hat{\boldsymbol{\tau}}_\alpha \boldsymbol{n}_{\beta\gamma} \, \mathrm{d}A \quad (2.79)$$

where $\hat{\boldsymbol{\tau}}_\alpha$ is the stress tensor, $\langle \eta_\alpha \rangle$ is the phase averaged partial dynamic viscosity, $\langle \boldsymbol{v}_\alpha \rangle^f$ is the intrinsic averaged velocity vector field, $\hat{\mathbf{I}}$ is the identity tensor, V_{REV} is the total volume of the REV, and $\boldsymbol{n}_{\beta\gamma}$ is the normal vector along the surface of the domain of the element.

2.4.3.2 Diffusion Coefficient

Section 2.3.2 showed that the diffusion coefficient calculated from Chapman-Engskog theory is a function of total pressure. As discussed in section 2.3.2, this total pressure cancels out and is not considered for volume averaging, however volume averaging is still required.

By volume averaging, the porosity of the porous medium has been accounted for in the diffusion term, expressed:

$$\langle \boldsymbol{D}_\alpha \rangle = \frac{1}{\varepsilon} \sum_{\beta=1}^{N} \langle P_\alpha \rangle \langle P_\beta \rangle \hat{\boldsymbol{D}}_{\alpha\beta} (\langle \boldsymbol{v}_\beta \rangle^f - \langle \boldsymbol{v}_\alpha \rangle^f) \quad (2.80)$$

$$= \sum_{\beta=1}^{N} \langle P_\alpha \rangle \langle P_\beta \rangle \left(\frac{1}{\varepsilon P_t \mathscr{D}_{\alpha\beta}} \hat{\mathbf{I}} \right) (\langle \boldsymbol{v}_\beta \rangle^f - \langle \boldsymbol{v}_\alpha \rangle^f) \quad (2.81)$$

From macro-scale observation a fluid may appear to travel in a straight line through a porous media, but unlike a channel a fluid is not able to move in any direction freely. Fine particles

that make up the porous media obstruct the path of the fluid, and the fluid must pass around these fine particles. This tortuous path that the particles diffuse along must be accounted for. This is typically represented mathematically as:

$$\mathscr{D}_{\alpha\beta}^{eff} = \frac{\varepsilon}{\tau}\mathscr{D}_{\alpha\beta} \tag{2.82}$$

where $\mathscr{D}_{\alpha\beta}^{eff}$ is the effective Maxwell-Stefan diffusion coefficient, and τ is the tortuosity through the porous media. When in the porous domain, $\mathscr{D}_{\alpha\beta}^{eff}$ is then used in place of $\mathscr{D}_{\alpha\beta}$ in the governing equations. Tortuosity is the ratio of the length of the cord to the distance between the two ends. A tortuosity of 1 would represent a straight line, while a circle would have an infinite tortuosity.

Tortuosity is a difficult quantity to obtain, and is typically estimated through empirical relations. The most common relation used is Bruggeman's relation, expressed as:

$$\tau = \varepsilon^{-0.5} \tag{2.83}$$

$$\mathscr{D}_{\alpha\beta}^{eff} = \varepsilon^{1.5}\mathscr{D}_{\alpha\beta} \tag{2.84}$$

Secanell [18] pointed out that this can lead to inaccuracies in modeling the porous layers of a PEFC. This is because Bruggeman [96] obtained this relation for a bed of spheres of different size [18, 96, 97], which does not accurately describe the porous structures in a PEFC. Pharoah et al. analyzed effective transport properties and determined that using the Bruggeman relation in a PEFC overpredicts the oxygen concentration in the CL resulting in higher current densities.

Secanell [18] used a relation proposed by Tomadakis et al. in [98], where Monte Carlo simulations were used for predicting effective diffusivity. They determined a relation for effective diffusivity that is expressed as:

$$\mathscr{D}_{\alpha\beta}^{eff} = \mathscr{D}_{\alpha\beta}\left(\frac{\varepsilon - \varepsilon_{th}}{1 - \varepsilon_{th}}\right)^{\mu}\mathcal{H}(\varepsilon - \varepsilon_{th}) \tag{2.85}$$

$$\mathcal{H}(\varepsilon - \varepsilon_{th}) = \begin{cases} 0 & \text{if } \varepsilon < \varepsilon_{th} \\ 1 & \text{if } \varepsilon \geq \varepsilon_{th} \end{cases} \tag{2.86}$$

where ε_{th} and μ are constants dependent on the orientation of the fibers in the porous media, and $\mathcal{H}(\varepsilon - \varepsilon_{th})$ is the Heaviside unit step function.

The method proposed by Tomadakis et al. [98] and used by Secanell [18] was also used in this work. The resulting diffusion coupling term in the governing equation is expressed

as:

$$\langle \boldsymbol{D}_\alpha \rangle = \sum_{\beta=1}^{N} \langle P_\alpha \rangle \langle P_\beta \rangle \hat{\boldsymbol{D}}_{\alpha\beta} (\langle \boldsymbol{v}_\beta \rangle^f - \langle \boldsymbol{v}_\alpha \rangle^f) \tag{2.87}$$

$$\hat{\boldsymbol{D}}_{\alpha\beta} = \left(P_t \mathscr{D}_{\alpha\beta}^{eff} \right)^{-1} \hat{\mathbf{I}} \tag{2.88}$$

$$\mathscr{D}_{\alpha\beta}^{eff} = \mathscr{D}_{\alpha\beta} \left(\frac{\varepsilon - \varepsilon_{th}}{1 - \varepsilon_{th}} \right)^{\mu} \mathcal{H}(\varepsilon - \varepsilon_{th}) \tag{2.89}$$

2.4.3.3 Viscosity Model

Both Wilke and Kerkhof and Geboers' viscosity models are functions of the unknown density scalar field, then an REV averaging must also be considered. This is much more straightforward than some of the previous REV averaging derivation, as no swapping of integration and differentiation is required.

2.4.3.3.1 Wilke's Model

The REV average of Wilke's viscosity model is derived by applying equation (2.52) to (2.30) as follows:

$$\langle \eta_\alpha \rangle = \frac{\eta_\alpha^0}{M_\alpha} \left\langle \frac{\rho_\alpha}{\sum_{\beta=1}^{N} \frac{\rho_\beta}{M_\beta} \xi_{\alpha\beta}} \right\rangle \tag{2.90}$$

$$= \frac{\langle \rho_\alpha \rangle \eta_\alpha^0}{\varepsilon M_\alpha \sum_{\beta=1}^{N} \frac{\langle \rho_\beta \rangle}{M_\beta} \xi_{\alpha\beta}} \tag{2.91}$$

2.4.3.3.2 Kerkhof and Geboers' Model

For Kerkhof and Geboers' viscosity model the values for $\hat{\boldsymbol{P}}$ off the main diagonal are not functions of the unknown density scalar field. As a result, only equation (2.36) needs to be REV averaged. This is done by simply applying equation (2.52) as follows:

$$\langle \eta_\alpha \rangle = \langle P_{\alpha\alpha} \rangle \tag{2.92}$$

$$= \frac{2}{kT} \left(\frac{4}{5} \Omega_{\alpha\alpha}^{(2,2)} + \left\langle \frac{16 M_\alpha}{15 \rho_\alpha} \sum_{\beta \neq \alpha}^{N} \frac{\rho_\beta}{(M_\alpha + M_\beta)^2} \left(5 M_\alpha \Omega_{\alpha\beta}^{(1,1)} + \frac{3}{2} M_\beta \Omega_{\alpha\beta}^{(2,2)} \right) \right\rangle \right) \tag{2.93}$$

$$= \frac{2}{kT} \left(\frac{4}{5} \Omega_{\alpha\alpha}^{(2,2)} + \frac{16 M_\alpha}{15 \varepsilon \langle \rho_\alpha \rangle} \sum_{\beta \neq \alpha}^{N} \frac{\langle \rho_\beta \rangle}{(M_\alpha + M_\beta)^2} \left(5 M_\alpha \Omega_{\alpha\beta}^{(1,1)} + \frac{3}{2} M_\beta \Omega_{\alpha\beta}^{(2,2)} \right) \right) \tag{2.94}$$

2.4.4 Summary

Consider a d-dimensional fuel cell model in the domain $\Omega \subset \mathbb{R}^d$ with a boundary Γ. From section 2.4 the governing equations must be valid in two separate domains, the channel and

the porous layers. As a result, the domain, Ω, must contain two subset domains. One for the channel $\Omega_c \subset \Omega$ with a boundary $\Gamma_c \subset \Gamma$, and a second for the porous layers $\Omega_p \subset \Omega$ with a boundary $\Gamma_p \subset \Gamma$.

From this information, and that from the previous sections, the governing equations can be re-written to be valid in all domains as follows:

$$0 = \nabla \cdot \boldsymbol{F}_{mass_\alpha} \qquad \text{in } \Omega \tag{2.95}$$

$$0 = \nabla \cdot (\hat{\boldsymbol{F}}_{mom_\alpha} + P_\alpha \hat{\mathbf{I}} - \hat{\boldsymbol{\tau}}_\alpha) - (\boldsymbol{F}_{por_\alpha} + \rho_\alpha \boldsymbol{g} + \boldsymbol{D}_\alpha) \qquad \text{in } \Omega \tag{2.96}$$

$$\hat{F}_{mass_\alpha} = \rho_\alpha \boldsymbol{v}_\alpha \tag{2.97}$$

$$\hat{\boldsymbol{F}}_{mom_\alpha} = \rho_\alpha \boldsymbol{v}_\alpha \otimes \boldsymbol{v}_\alpha \tag{2.98}$$

$$P_\alpha = \rho_\alpha \frac{R T_{mix}}{M_\alpha} \tag{2.99}$$

$$\hat{\boldsymbol{\tau}}_\alpha = 2\eta_\alpha \nabla_s \boldsymbol{v}_\alpha - \frac{2}{3}\eta_\alpha \nabla \cdot \boldsymbol{v}_\alpha \hat{\mathbf{I}} \tag{2.100}$$

$$\boldsymbol{F}_{por_\alpha} = \begin{cases} 0 & \text{in } \Omega_c \\ -\eta_\alpha \hat{\mathbf{K}}^{-1} \varepsilon \boldsymbol{v}_\alpha - \hat{\boldsymbol{\beta}} \rho_\alpha |\varepsilon \boldsymbol{v}_\alpha| \varepsilon \boldsymbol{v}_\alpha & \text{in } \Omega_p \end{cases} \tag{2.101}$$

$$\boldsymbol{D}_\alpha = \sum_{\beta=1}^{N} P_\alpha P_\beta \hat{\boldsymbol{D}}_{\alpha\beta} (\boldsymbol{v}_\beta - \boldsymbol{v}_\alpha) \tag{2.102}$$

$$\hat{\boldsymbol{D}}_{\alpha\beta} = \left(P_t \mathscr{D}_{\alpha\beta}^{eff} \right)^{-1} \hat{\mathbf{I}} \tag{2.103}$$

$$\varepsilon = \begin{cases} 1 & \text{in } \Omega_c \\ 0 < \varepsilon \leq 1 & \text{in } \Omega_p \end{cases} \tag{2.104}$$

$$\rho_\alpha = \begin{cases} \rho_\alpha & \text{in } \Omega_c \\ \langle \rho_\alpha \rangle & \text{in } \Omega_p \end{cases} \tag{2.105}$$

$$\boldsymbol{v}_\alpha = \begin{cases} \boldsymbol{v}_\alpha & \text{in } \Omega_c \\ \langle \boldsymbol{v}_\alpha \rangle^f & \text{in } \Omega_p \end{cases} \tag{2.106}$$

where $\forall \alpha \in \mathbb{Z}$ and is the species index in the domain Ω.

2.5 Linearization

2.5.1 Newton-Raphson's Method

Since this is a nonlinear system of equations the governing equations are linearized. This can be done before or after the equations are weakened. Due to personal preference the governing equations were linearized first. This is done by taking the governing equations in

their current residual form, and perturbing the solution variables slightly using a first order Taylor series expansion. This is done as follows:

$$0 = \boldsymbol{R}(\rho_\alpha^{n+1}, \boldsymbol{v}_\alpha^{n+1}) = \boldsymbol{R}(\rho_\alpha^n, \boldsymbol{v}_\alpha^n) + \left.\frac{\partial \boldsymbol{R}}{\partial \rho_\alpha}\right|^n \delta\rho_\alpha + \left.\frac{\partial \boldsymbol{R}}{\partial \boldsymbol{v}_\alpha}\right|^n \delta\boldsymbol{v}_\alpha + \mathcal{O}((\delta\rho_\alpha)^2 + (\delta\boldsymbol{v}_\alpha)^2) \tag{2.107}$$

Thus, the linear problem to be solved is of the form:

$$\left.\frac{\partial \boldsymbol{R}}{\partial \rho_\alpha}\right|^n \delta\rho_\alpha + \left.\frac{\partial \boldsymbol{R}}{\partial \boldsymbol{v}_\alpha}\right|^n \delta\boldsymbol{v}_\alpha = -\boldsymbol{R}(\rho_\alpha^n, \boldsymbol{v}_\alpha^n) \tag{2.108}$$

where the solution increments, $\delta\rho_\alpha$ and $\delta\boldsymbol{v}_\alpha$ are being solved for. For future convenience, when the variation operator, δ, is not applied to a solution variable it will take the form:

$$\delta\boldsymbol{R} = \left.\frac{\partial \boldsymbol{R}}{\partial \rho_\alpha}\right|^n \delta\rho_\alpha + \left.\frac{\partial \boldsymbol{R}}{\partial \boldsymbol{v}_\alpha}\right|^n \delta\boldsymbol{v}_\alpha \tag{2.109}$$

After $\delta\rho_\alpha$ and $\delta\boldsymbol{v}_\alpha$ have been solved for, a line search method is used to update the solution variables. This line search method is done as follows:

$$\rho_\alpha^{n+1} = \rho_\alpha^n + h\delta\rho_\alpha \tag{2.110}$$

$$\boldsymbol{v}_\alpha^{n+1} = \boldsymbol{v}_\alpha^n + h\delta\boldsymbol{v}_\alpha \tag{2.111}$$

where h is a relaxation step size that can be used to help convergence. For all cases analyzed in this work a value of 1 for h was found to be suitable.

The solution variables are categorized into blocks. One block for each density species solution variable, and d blocks for each orthogonal velocity species component in d-dimensional space. At the end of each iteration the L_2 norm is computed for each of these vectors. The overall residual is then computed as the L_2 norm of these L_2 norm block residuals. For the stopping criteria, a tolerance of 10^{-8} was used.

2.5.2 Multi-Component Mass Transport Model

Applying the process discussed in the previous section to the governing equations, the Taylor series expansion appears as follows:

$$\nabla \cdot \boldsymbol{F}_{mass_\alpha}^{n+1} = \nabla \cdot (\boldsymbol{F}_{mass_\alpha}^n + \delta\boldsymbol{F}_{mass_\alpha}^n) + \mathcal{O}((\delta\rho_\alpha)^2 + (\delta\boldsymbol{v}_\alpha)^2) \tag{2.112}$$

$$\begin{aligned} \nabla \cdot (\hat{\boldsymbol{F}}_{mom_\alpha}^{n+1} + P_\alpha^{n+1}\hat{\mathbf{I}} - \hat{\boldsymbol{\tau}}_\alpha^{n+1}) - (\boldsymbol{F}_{por_\alpha}^{n+1} + \rho_\alpha^{n+1}\boldsymbol{g} + \boldsymbol{D}_\alpha^{n+1}) \\ = \nabla \cdot [(\hat{\boldsymbol{F}}_{mom_\alpha}^n + \delta\hat{\boldsymbol{F}}_{mom_\alpha}) + (P_\alpha^n\hat{\mathbf{I}} + \delta P_\alpha\hat{\mathbf{I}}) - (\hat{\boldsymbol{\tau}}_\alpha^n + \delta\hat{\boldsymbol{\tau}}_\alpha)] \\ - [(\boldsymbol{F}_{por_\alpha}^n + \delta\boldsymbol{F}_{por_\alpha}) + (\rho_\alpha^n\boldsymbol{g} + \delta\rho_\alpha\boldsymbol{g}) + (\boldsymbol{D}_\alpha^n + \delta\boldsymbol{D}_\alpha)] \\ + \mathcal{O}((\delta\rho_\alpha)^2 + (\delta\boldsymbol{v}_\alpha)^2) \end{aligned} \tag{2.113}$$

Neglecting higher order terms the linearized system of equations to be solved are:

$$\nabla \cdot \delta \boldsymbol{F}_{mass_\alpha} = -\nabla \cdot \boldsymbol{F}^n_{mass_\alpha} \quad \text{in } \Omega \tag{2.114}$$

$$\begin{aligned} \nabla \cdot (\delta \hat{\boldsymbol{F}}_{mom_\alpha} + \delta P_\alpha \hat{\mathbf{I}} - \delta \hat{\boldsymbol{\tau}}_\alpha) - (\delta \boldsymbol{F}_{por_\alpha} + \delta \rho_\alpha \boldsymbol{g} + \delta \boldsymbol{D}_\alpha) \\ = -\nabla \cdot (\hat{\boldsymbol{F}}^n_{mom_\alpha} + P^n_\alpha \hat{\mathbf{I}} - \hat{\boldsymbol{\tau}}^n_\alpha) + (\boldsymbol{F}^n_{por_\alpha} + \rho^n_\alpha \boldsymbol{g} + \boldsymbol{D}^n_\alpha) \end{aligned} \quad \text{in } \Omega \tag{2.115}$$

$$\delta \boldsymbol{F}_{mass_\alpha} = \delta \rho_\alpha \boldsymbol{v}^n_\alpha + \rho^n_\alpha \delta \boldsymbol{v}_\alpha \tag{2.116}$$

$$\delta \hat{\boldsymbol{F}}_{mom_\alpha} = \delta \rho_\alpha \boldsymbol{v}^n_\alpha \otimes \boldsymbol{v}^n_\alpha + \rho^n_\alpha \delta \boldsymbol{v}_\alpha \otimes \boldsymbol{v}^n_\alpha + \rho^n_\alpha \boldsymbol{v}^n_\alpha \otimes \delta \boldsymbol{v}_\alpha \tag{2.117}$$

$$\delta P_\alpha = \delta \rho_\alpha \frac{R T_{mix}}{M_\alpha} \tag{2.118}$$

$$\delta \boldsymbol{F}_{por_\alpha} = \begin{cases} 0 & \text{in } \Omega_c \\ -\hat{\mathbf{K}}^{-1} \varepsilon \left(\boldsymbol{v}^n_\alpha \delta \eta_\alpha + \eta_\alpha \delta \boldsymbol{v}_\alpha \right) & \\ \quad - \hat{\boldsymbol{\beta}} \left(\delta \rho_\alpha |\varepsilon \boldsymbol{v}^n_\alpha| \varepsilon \boldsymbol{v}^n_\alpha + \rho^n_\alpha \dfrac{\varepsilon \boldsymbol{v}^n_\alpha \varepsilon \delta \boldsymbol{v}_\alpha}{|\varepsilon \boldsymbol{v}^n_\alpha|} \varepsilon \boldsymbol{v}^n_\alpha + \rho^n_\alpha |\varepsilon \boldsymbol{v}^n_\alpha| \varepsilon \delta \boldsymbol{v}_\alpha \right) & \text{in } \Omega_p \end{cases} \tag{2.119}$$

$$\delta \boldsymbol{D}_\alpha = \sum_{\beta=1}^{N} (\delta P_\alpha P_\beta + P_\alpha \delta P_\beta) \hat{\boldsymbol{D}}_{\alpha\beta} (\boldsymbol{v}^n_\beta - \boldsymbol{v}^n_\alpha) + P_\alpha P_\beta \hat{\boldsymbol{D}}_{\alpha\beta} (\delta \boldsymbol{v}_\beta - \delta \boldsymbol{v}_\alpha) \tag{2.120}$$

$$\varepsilon = \begin{cases} 1 & \text{in } \Omega_c \\ 0 < \varepsilon \leq 1 & \text{in } \Omega_p \end{cases} \tag{2.121}$$

$$\rho^n_\alpha = \begin{cases} \rho^n_\alpha & \text{in } \Omega_c \\ \langle \rho^n_\alpha \rangle & \text{in } \Omega_p \end{cases} \tag{2.122}$$

$$\boldsymbol{v}^n_\alpha = \begin{cases} \boldsymbol{v}^n_\alpha & \text{in } \Omega_c \\ \langle \boldsymbol{v}^n_\alpha \rangle^f & \text{in } \Omega_p \end{cases} \tag{2.123}$$

2.5.3 Closure Equations

2.5.3.1 Viscous Stress Tensor

The viscous stress tensor is a function composed of gradients and divergence of the velocity solution variable as well as the partial viscosity. Since the partial viscosity is a function of the density scalar field, this results in an extra term for the variation with respect to the partial viscosity. It can easily be determined that the variation in the viscous stress tensor is as follows:

$$\delta \hat{\boldsymbol{\tau}}_\alpha = \delta \eta_\alpha \left(2 \nabla_s \boldsymbol{v}_\alpha - \frac{2}{3} (\nabla \cdot \boldsymbol{v}_\alpha) \hat{\mathbf{I}} \right) + \eta_\alpha \left(2 \nabla_s \delta \boldsymbol{v}_\alpha - \frac{2}{3} (\nabla \cdot \delta \boldsymbol{v}_\alpha) \hat{\mathbf{I}} \right) \tag{2.124}$$

2.5.3.2 Viscosity Model

As mentioned in the previous section, both viscosity models are functions of the unknown density scalar field. As a result, the variation with respect to the density scalar field must

be determined for these models.

2.5.3.2.1 Wilke's Model

The variation in Wilke's model is straightforward and can easily be shown to be equivalent to:

$$\langle \eta_\alpha \rangle = \frac{\langle \rho_\alpha \rangle \eta_\alpha^0}{\varepsilon M_\alpha \sum_{\beta=1}^{N} \frac{\langle \rho_\beta \rangle}{M_\beta} \xi_{\alpha\beta}} \tag{2.125}$$

$$\delta\langle \eta_\alpha \rangle = \frac{\delta\langle \rho_\alpha \rangle \eta_\alpha^0}{\varepsilon M_\alpha \sum_{\beta=1}^{N} \frac{\langle \rho_\beta \rangle}{M_\beta} \xi_{\alpha\beta}} - \frac{\langle \rho_\alpha \rangle \eta_\alpha^0}{\varepsilon M_\alpha \left(\sum_{\beta=1}^{N} \frac{\langle \rho_\beta \rangle}{M_\beta} \xi_{\alpha\beta} \right)^2} \sum_{\beta=1}^{N} \frac{\delta\langle \rho_\beta \rangle}{M_\beta} \xi_{\alpha\beta} \tag{2.126}$$

$$= \frac{\eta_\alpha^0}{\varepsilon M_\alpha} \left(\sum_{\beta=1}^{N} \frac{\langle \rho_\beta \rangle}{M_\beta} \xi_{\alpha\beta} \right)^{-1} \left[\delta\langle \rho_\alpha \rangle - \langle \rho_\alpha \rangle \left(\sum_{\beta=1}^{N} \frac{\langle \rho_\beta \rangle}{M_\beta} \xi_{\alpha\beta} \right)^{-1} \left(\sum_{\beta=1}^{N} \frac{\delta\langle \rho_\beta \rangle}{M_\beta} \xi_{\alpha\beta} \right) \right] \tag{2.127}$$

2.5.3.2.2 Kerkhof and Geboers' Model

Kerkhof and Geboers' model is difficult to linearize as equation (2.35) is a set of independent equations. On first inspection one may be inclined to do as follows:

$$\hat{\boldsymbol{P}} \boldsymbol{\eta} = \mathbf{1} \tag{2.128}$$

$$\boldsymbol{\eta} = \hat{\boldsymbol{P}}^{-1} \mathbf{1} \tag{2.129}$$

$$\delta\boldsymbol{\eta} = \delta \left(\hat{\boldsymbol{P}}^{-1} \right) \mathbf{1} \tag{2.130}$$

The problem is that this involves inverting a matrix where the values are determined by equations (2.36) and (2.37) and then taking the variation. This is a huge problem if everything is done analytically. Alternatively, take:

$$\hat{\boldsymbol{P}} \boldsymbol{\eta} = \mathbf{1} \tag{2.131}$$

$$\delta\hat{\boldsymbol{P}} \boldsymbol{\eta} + \hat{\boldsymbol{P}} \delta\boldsymbol{\eta} = \mathbf{0} \tag{2.132}$$

$$\delta\boldsymbol{\eta} = -\hat{\boldsymbol{P}}^{-1} \delta\hat{\boldsymbol{P}} \boldsymbol{\eta} \tag{2.133}$$

Finally substitute equation (2.129) into (2.133):

$$\delta\boldsymbol{\eta} = -\hat{\boldsymbol{P}}^{-1} \delta\hat{\boldsymbol{P}} \hat{\boldsymbol{P}}^{-1} \mathbf{1} \tag{2.134}$$

Using equation (2.134) the matrix inversion can be done numerically and only the variation in $\hat{\boldsymbol{P}}$ with respect to density is required. Equations (2.130) and (2.134) can be shown to be

equivalent by considering:

$$\delta\left(\hat{\boldsymbol{P}}^{-1}\hat{\boldsymbol{P}}\hat{\boldsymbol{P}}^{-1}\right) = 2\delta\left(\hat{\boldsymbol{P}}^{-1}\right)\hat{\boldsymbol{P}}\hat{\boldsymbol{P}}^{-1} + \hat{\boldsymbol{P}}^{-1}\delta\hat{\boldsymbol{P}}\hat{\boldsymbol{P}}^{-1} \tag{2.135}$$

$$\delta\left(\hat{\boldsymbol{P}}^{-1}\right) = 2\delta\left(\hat{\boldsymbol{P}}^{-1}\right) + \hat{\boldsymbol{P}}^{-1}\delta\hat{\boldsymbol{P}}\hat{\boldsymbol{P}}^{-1} \tag{2.136}$$

$$-\hat{\boldsymbol{P}}^{-1}\delta\hat{\boldsymbol{P}}\hat{\boldsymbol{P}}^{-1} = \delta\left(\hat{\boldsymbol{P}}^{-1}\right) \tag{2.137}$$

If equation (2.137) is substituted into (2.134), one obtains equation (2.130). Thus, showing equations (2.130) and (2.134) are equivalent.

Since the values off the main diagonal of $\hat{\boldsymbol{P}}$ are not a function of the density scalar field, they will be zero. This results in a variation of a matrix that only contains values along the main diagonal. The values for $\delta P_{\alpha\alpha}$ are as follows:

$$\delta\langle P_{\alpha\alpha}\rangle = \frac{32M_\alpha}{15\varepsilon kT\langle\rho_\alpha\rangle}\left(\sum_{\beta\neq\alpha}^{N}\frac{\delta\langle\rho_\beta\rangle}{(M_\alpha+M_\beta)^2}\right. \tag{2.138}$$

$$\left. - \frac{\delta\langle\rho_\alpha\rangle}{\langle\rho_\alpha\rangle}\sum_{\beta\neq\alpha}^{N}\frac{\langle\rho_\beta\rangle}{(M_\alpha+M_\beta)^2}\right)\left(5M_\alpha\Omega_{\alpha\beta}^{(1,1)} + \frac{3}{2}M_\beta\Omega_{\alpha\beta}^{(2,2)}\right) \tag{2.139}$$

2.6 Weak Formulation

The linearized form of the governing PDEs are weakened using the Bubnov-Galerkin finite element method (FEM). Using the same justification as Reddy [99] for 2D incompressible flow, q_α and $\boldsymbol{w}_\alpha$ are chosen to represent the arbitrary scalar and vector test functions for the density and velocity of species α respectively. q_α is multiplied by equation (2.114), while $\boldsymbol{w}_\alpha$ is multiplied by equation (2.115) using the dot product operator to produce a scalar momentum equation for each species α. For simplicity the index for species is removed, and only one of the species is considered. Integrating over the entire domain, Ω, the resulting set of scalar equations are:

$$\int_\Omega q\nabla\cdot\delta\boldsymbol{F}_{mass}\,\mathrm{d}\Omega = \int_\Omega -q\nabla\cdot\boldsymbol{F}_{mass}^{n}\,\mathrm{d}\Omega \tag{2.140}$$

$$\int_\Omega \boldsymbol{w}\cdot\left(\nabla\cdot(\delta\hat{\boldsymbol{F}}_{mom} + \delta P\hat{\mathbf{I}} - \delta\hat{\boldsymbol{\tau}}) - (\delta\boldsymbol{F}_{por} + \delta\rho\boldsymbol{g} + \delta\boldsymbol{D})\right)\mathrm{d}\Omega$$

$$= \int_\Omega -\boldsymbol{w}\cdot\left(\nabla\cdot(\hat{\boldsymbol{F}}_{mom}^{n} + P^n\hat{\mathbf{I}} - \hat{\boldsymbol{\tau}}^n) - (\boldsymbol{F}_{por}^{n} + \rho^n\boldsymbol{g} + \boldsymbol{D}^n)\right)\mathrm{d}\Omega \tag{2.141}$$

The integrals above require that in order to achieve a solution the following requirements must be met in Sobolev space:

$$\rho \in H^1 := \left\{ \rho : \Omega \to \mathbb{R} : \int_\Omega \rho^2 + (\rho')^2 \, \mathrm{d}\Omega < \infty \right\} \tag{2.142}$$

$$\delta\rho \in H^1 := \left\{ \delta\rho : \Omega \to \mathbb{R} : \int_\Omega (\delta\rho)^2 + (\delta\rho')^2 \, \mathrm{d}\Omega < \infty \right\} \tag{2.143}$$

$$q \in H^0 := \left\{ q : \Omega \to \mathbb{R} : \int_\Omega q^2 \, \mathrm{d}\Omega < \infty \right\} \tag{2.144}$$

$$\boldsymbol{v} \in H^2 := \left\{ \boldsymbol{v} : \Omega \to \mathbb{R}^d : \int_\Omega \boldsymbol{v}^2 + (\boldsymbol{v}')^2 + (\boldsymbol{v}'')^2 \, \mathrm{d}\Omega < \infty \right\} \tag{2.145}$$

$$\delta\boldsymbol{v} \in H^2 := \left\{ \delta\boldsymbol{v} : \Omega \to \mathbb{R}^d : \int_\Omega (\delta\boldsymbol{v})^2 + (\delta\boldsymbol{v}')^2 + (\delta\boldsymbol{v}'')^2 \, \mathrm{d}\Omega < \infty \right\} \tag{2.146}$$

$$\boldsymbol{w} \in H^0 := \left\{ \boldsymbol{w} : \Omega \to \mathbb{R}^d : \int_\Omega \boldsymbol{w}^2 \, \mathrm{d}\Omega < \infty \right\} \tag{2.147}$$

The ideal goal when performing the FEM is to weaken the equation such that both the solution variable and test function belong to the same space, i.e. $\boldsymbol{v}, \boldsymbol{w} \in H^1$. For density and its respective test function q this is not possible. In this case, a weakened form where $\rho \in H^0$ and $q \in H^1$ was found. To do this, first the following identities are applied:

$$\nabla \cdot (\boldsymbol{F} q) = q \nabla \cdot \boldsymbol{F} + \boldsymbol{F} \cdot \nabla q \tag{2.148}$$

$$\nabla \cdot \left(\hat{\boldsymbol{T}}_s \boldsymbol{F} \right) = \nabla \boldsymbol{F} : \hat{\boldsymbol{T}}_s + \boldsymbol{F} \cdot \nabla \cdot \hat{\boldsymbol{T}}_s \tag{2.149}$$

where $\boldsymbol{F}$ is a vector field, q is a scalar field, and $\hat{\boldsymbol{T}}_s$ is a symmetric tensor of rank 2. Equation (2.148) is well known and it is left to the reader to prove if they desire, while equation (2.149) is not as typical of an identity. For this reason a proof for it can be found in Appendix B.1. Discretizing the integral over the entire domain, Ω, into smaller elements, Ω^e, and applying these identities result in the following set of equations:

$$\int_{\Omega^e} \nabla \cdot (q \delta \boldsymbol{F}_{mass}) - \delta \boldsymbol{F}_{mass} \cdot \nabla q \, \mathrm{d}\Omega^e = \int_{\Omega^e} -\nabla \cdot (q \boldsymbol{F}^n_{mass}) + \boldsymbol{F}^n_{mass} \cdot \nabla q \, \mathrm{d}\Omega^e \tag{2.150}$$

$$\begin{aligned} &\int_{\Omega^e} \nabla \cdot \left(\left(\delta \hat{\boldsymbol{F}}_{mom} + \delta P \hat{\mathbf{I}} - \delta \hat{\boldsymbol{\tau}} \right) \boldsymbol{w} \right) - \nabla \boldsymbol{w} : \left(\delta \hat{\boldsymbol{F}}_{mom} + \delta P \hat{\mathbf{I}} - \delta \hat{\boldsymbol{\tau}} \right) - \boldsymbol{w} \cdot (\delta \boldsymbol{F}_{por} + \delta \rho \boldsymbol{g} + \delta \boldsymbol{D}) \, \mathrm{d}\Omega^e \\ &= \int_{\Omega^e} -\nabla \cdot \left(\left(\hat{\boldsymbol{F}}^n_{mom} + P^n \hat{\mathbf{I}} - \hat{\boldsymbol{\tau}}^n \right) \boldsymbol{w} \right) + \nabla \boldsymbol{w} : \left(\hat{\boldsymbol{F}}^n_{mom} + P^n \hat{\mathbf{I}} - \hat{\boldsymbol{\tau}}^n \right) + \boldsymbol{w} \cdot \left(\boldsymbol{F}^n_{por} + \rho^n \boldsymbol{g} + \boldsymbol{D}^n \right) \, \mathrm{d}\Omega^e \end{aligned} \tag{2.151}$$

Now the divergence theorem can be applied resulting in:

$$-\int_{\Omega^e} \delta \boldsymbol{F}_{mass} \cdot \nabla q \, \mathrm{d}\Omega^e + \oint_{\Gamma^e} q \delta \boldsymbol{F}_{mass} \cdot \boldsymbol{n} \, \mathrm{d}\Gamma^e = \int_{\Omega^e} \boldsymbol{F}^n_{mass} \cdot \nabla q \, \mathrm{d}\Omega^e - \oint_{\Gamma^e} q \boldsymbol{F}^n_{mass} \cdot \boldsymbol{n} \, \mathrm{d}\Gamma^e \tag{2.152}$$

$$
\begin{aligned}
-\int_{\Omega^e} \nabla \boldsymbol{w} : \left(\delta \hat{\boldsymbol{F}}_{mom} + \delta P \hat{\mathbf{I}} - \delta \hat{\boldsymbol{\tau}}\right) + \boldsymbol{w} \cdot \left(\delta \boldsymbol{F}_{por} + \delta \rho \boldsymbol{g} + \delta \boldsymbol{D}\right) \mathrm{d}\Omega^e \\
+ \oint_{\Gamma^e} \left(\delta \hat{\boldsymbol{F}}_{mom} + \delta P \hat{\mathbf{I}} - \delta \hat{\boldsymbol{\tau}}\right) \boldsymbol{w} \cdot \boldsymbol{n} \, \mathrm{d}\Gamma^e \\
= \int_{\Omega^e} \nabla \boldsymbol{w} : \left(\hat{\boldsymbol{F}}^n_{mom} + P^n \hat{\mathbf{I}} - \hat{\boldsymbol{\tau}}^n\right) + \boldsymbol{w} \cdot \left(\boldsymbol{F}^n_{por} + \rho^n \boldsymbol{g} + \boldsymbol{D}^n\right) \mathrm{d}\Omega^e \\
- \oint_{\Gamma^e} \left(\hat{\boldsymbol{F}}^n_{mom} + P^n \hat{\mathbf{I}} - \hat{\boldsymbol{\tau}}^n\right) \boldsymbol{w} \cdot \boldsymbol{n} \, \mathrm{d}\Gamma^e \quad (2.153)
\end{aligned}
$$

Equations (2.152) and (2.153) are now in a desirable Sobolev space to achieve a solution. The Sobolev space for each solution variable and test function are:

$$\rho \in H^0 := \left\{ \rho : \Omega \to \mathbb{R} : \int_\Omega \rho^2 \, \mathrm{d}\Omega < \infty \right\} \quad (2.154)$$

$$\delta\rho \in H^0 := \left\{ \delta\rho : \Omega \to \mathbb{R} : \int_\Omega \delta\rho^2 \, \mathrm{d}\Omega < \infty \right\} \quad (2.155)$$

$$q \in H^1 := \left\{ q : \Omega \to \mathbb{R} : \int_\Omega q^2 + (q')^2 \, \mathrm{d}\Omega < \infty \right\} \quad (2.156)$$

$$\boldsymbol{v} \in H^1 := \left\{ \boldsymbol{v} : \Omega \to \mathbb{R}^d : \int_\Omega \boldsymbol{v}^2 + (\boldsymbol{v}')^2 \, \mathrm{d}\Omega < \infty \right\} \quad (2.157)$$

$$\delta\boldsymbol{v} \in H^1 := \left\{ \delta\boldsymbol{v} : \Omega \to \mathbb{R}^d : \int_\Omega (\delta\boldsymbol{v})^2 + (\delta\boldsymbol{v}')^2 \, \mathrm{d}\Omega < \infty \right\} \quad (2.158)$$

$$\boldsymbol{w} \in H^1 := \left\{ \boldsymbol{w} : \Omega \to \mathbb{R}^d : \int_\Omega \boldsymbol{w}^2 + (\boldsymbol{w}')^2 \, \mathrm{d}\Omega < \infty \right\} \quad (2.159)$$

The arbitrary test functions are approximated by piece-wise shape functions, i.e.:

$$q \approx \sum_{i=1}^{N} q_i \psi_i^\rho \quad (2.160)$$

$$\delta\rho \approx \sum_{j=1}^{N} \delta\rho_j \psi_j^\rho \quad (2.161)$$

$$\delta\boldsymbol{v} \approx \begin{bmatrix} \sum_{l=1}^{N} \delta v_l^x \psi_l^{v_x} \\ \sum_{m=1}^{N} \delta v_m^y \psi_m^{v_y} \end{bmatrix} \quad (2.162)$$

To solve equations (2.152) and (2.153), they must be formulated into matrix form, i.e. $\hat{\boldsymbol{A}}\boldsymbol{x} = \boldsymbol{b}$. For simplicity, this is shown below for a 2D case of a single species where Dirichlet boundary conditions for velocity and density are assumed to be applied along all boundaries. It should be mentioned that this method can be applied the same for multiple species in 3D space. Substituting in the Bubnov-Galerkin method into equation (2.152) and expanding:

$$-\int_{\Omega^e} \delta\rho \boldsymbol{v}^n \cdot \nabla q + \rho^n \delta\boldsymbol{v} \cdot \nabla q \, \mathrm{d}\Omega^e = \int_{\Omega^e} \rho^n \boldsymbol{v}^n \cdot \nabla q \, \mathrm{d}\Omega^e \quad (2.163)$$

$$
\begin{aligned}
-\int_{\Omega^e} \sum_{j=1}^{N} \left[\delta\rho_j \psi_j^\rho v_x^n \sum_{i=1}^{N} q_i \frac{\partial \psi_i^\rho}{\partial x} \right] + \sum_{j=1}^{N} \left[\delta\rho_j \psi_j^\rho v_y^n \sum_{i=1}^{N} q_i \frac{\partial \psi_i^\rho}{\partial y} \right] \\
+ \sum_{l=1}^{N} \left[\rho^n \delta v_l^x \psi_l^{v_x} \sum_{i=1}^{N} q_i \frac{\partial \psi_i^\rho}{\partial x} \right] + \sum_{m=1}^{N} \left[\rho^n \delta v_m^y \psi_m^{v_y} \sum_{i=1}^{N} q_i \frac{\partial \psi_i^\rho}{\partial y} \right] \mathrm{d}\Omega^e \\
= \int_{\Omega^e} \rho^n v_x^n \sum_{i=1}^{N} q_i \frac{\partial \psi_i^\rho}{\partial x} + \rho^n v_y^n \sum_{i=1}^{N} q_i \frac{\partial \psi_i^\rho}{\partial y} \mathrm{d}\Omega^e \quad (2.164)
\end{aligned}
$$

where i, j, l, and m are the components of the degrees of freedom (dofs), N is the maximum number of dofs, and ψ_ρ, ψ_{v_x}, and ψ_{v_y} are the Lagrangian shape functions, and ρ^n, v_x^n, and v_y^n are the nodal values from the previous solution, Due to the fact that q_i can take any value, it can be pulled out of the integral like so:

$$
\begin{aligned}
-\cancel{\sum_{i=1}^{N} q_i} \int_{\Omega^e} \sum_{j=1}^{N} \delta\rho_j \psi_j^\rho v_x^n \frac{\partial \psi_i^\rho}{\partial x} + \sum_{j=1}^{N} \delta\rho_j \psi_j^\rho v_y^n \frac{\partial \psi_i^\rho}{\partial y} \\
+ \sum_{l=1}^{N} \rho^n \delta v_l^x \psi_l^{v_x} \frac{\partial \psi_i^\rho}{\partial x} + \sum_{m=1}^{N} \rho^n \delta v_m^y \psi_m^{v_y} \frac{\partial \psi_i^\rho}{\partial y} \mathrm{d}\Omega^e \\
= \cancel{\sum_{i=1}^{N} q_i} \int_{\Omega^e} \rho^n v_x^n \frac{\partial \psi_i^\rho}{\partial x} + \rho^n v_y^n \frac{\partial \psi_i^\rho}{\partial y} \quad (2.165)
\end{aligned}
$$

Resulting in equation:

$$
\begin{aligned}
-\int_{\Omega^e} \sum_{j=1}^{N} \delta\rho_j \psi_j^\rho v_x^n \frac{\partial \psi_i^\rho}{\partial x} + \sum_{j=1}^{N} \delta\rho_j \psi_j^\rho v_y^n \frac{\partial \psi_i^\rho}{\partial y} \\
+ \sum_{l=1}^{N} \rho^n \delta v_l^x \psi_l^{v_x} \frac{\partial \psi_i^\rho}{\partial x} + \sum_{m=1}^{N} \rho^n \delta v_m^y \psi_m^{v_y} \frac{\partial \psi_i^\rho}{\partial y} \mathrm{d}\Omega^e \\
= \int_{\Omega^e} \rho^n v_x^n \frac{\partial \psi_i^\rho}{\partial x} + \rho^n v_y^n \frac{\partial \psi_i^\rho}{\partial y} \quad (2.166)
\end{aligned}
$$

Equation (2.152) has now been transformed into the matrix form $\hat{\boldsymbol{K}}(-\delta\boldsymbol{u}) = \boldsymbol{f}$, where index i refers to the row of the matrix, indices j, l, and m refer to the column of the matrix, and $\delta\rho$, δv_x, and δv_y are the unknowns being solved for.

The same approach is now applied to (2.153), except to maintain readability the element

contribution will only be shown in vector notation, i.e.:

$$\delta\psi^{\rho} = \sum_{j=1}^{N} \delta\rho_j \psi_j^{\rho} \tag{2.167}$$

$$\delta\boldsymbol{\psi}^{v} = \begin{bmatrix} \sum_{l=1}^{N} \delta v_l^x \psi_l^{v_x} \\ \sum_{r=1}^{N} \delta v_r^y \psi_r^{v_y} \end{bmatrix} \tag{2.168}$$

$$\boldsymbol{\psi}^{w} = \begin{bmatrix} \sum_{k=1}^{N} w_k^x \psi_k^{v_x} \\ \sum_{p=1}^{N} w_p^y \psi_p^{v_y} \end{bmatrix} \tag{2.169}$$

It should be remembered that for a single gas the partial viscosity equals the dynamic viscosity, which is not a function of density. Substituting the above equations into equation (2.153):

$$\begin{aligned} -\int_{\Omega^e} \nabla\boldsymbol{\psi}^{w} : \Bigg(& (\delta\psi^{\rho}\boldsymbol{v}^{n} \otimes \boldsymbol{v}^{n} + \rho^{n}\delta\boldsymbol{\psi}^{v} \otimes \boldsymbol{v}^{n} + \rho^{n}\boldsymbol{v}^{n} \otimes \delta\boldsymbol{\psi}^{v}) + \delta\psi^{\rho}\frac{RT_{mix}}{M}\hat{\mathbf{I}} \\ & -\eta\left(2\nabla_s\delta\boldsymbol{\psi}^{v} - \frac{2}{3}(\nabla\cdot\delta\boldsymbol{\psi}^{v})\hat{\mathbf{I}}\right)\Bigg) + \boldsymbol{\psi}^{w}\cdot\Bigg(\Big(-\eta\hat{\mathbf{K}}^{-1}\varepsilon\delta\boldsymbol{\psi}^{v} \\ & -\hat{\boldsymbol{\beta}}\left(\delta\psi^{\rho}|\varepsilon\boldsymbol{v}^{n}|\varepsilon\boldsymbol{v}^{n} + \rho^{n}\frac{\varepsilon\boldsymbol{v}^{n}\varepsilon\delta\boldsymbol{\psi}^{v}}{|\varepsilon\boldsymbol{v}^{n}|}\varepsilon\boldsymbol{v}^{n} + \rho^{n}|\varepsilon\boldsymbol{v}^{n}|\varepsilon\delta\boldsymbol{\psi}^{v}\right)\Big) + \delta\psi^{\rho}\boldsymbol{g}\Bigg)\,\mathrm{d}\Omega^{e} \\ = \int_{\Omega^e} \nabla\boldsymbol{\psi}^{w} : \Bigg(& \rho^{n}\boldsymbol{v}^{n} \otimes \boldsymbol{v}^{n} + \rho^{n}\frac{RT_{mix}}{M}\hat{\mathbf{I}} - \eta\left(2\nabla_s\delta\boldsymbol{\psi}^{v} - \frac{2}{3}(\nabla\cdot\delta\boldsymbol{\psi}^{v})\hat{\mathbf{I}}\right)\Bigg) \\ & \boldsymbol{\psi}^{w}\cdot\Bigg(\Big(-\eta\hat{\mathbf{K}}^{-1}\varepsilon\boldsymbol{v}^{n} - \hat{\boldsymbol{\beta}}\rho^{n}|\varepsilon\boldsymbol{v}^{n}|\varepsilon\boldsymbol{v}^{n}\Big) + \rho^{n}\boldsymbol{g}\Bigg)\,\mathrm{d}\Omega^{e} \end{aligned} \tag{2.170}$$

Similarly as before the terms: $\sum_{k=1}^{N} w_{x,k}$ and $\sum_{p=1}^{N} w_{y,p}$ can be pulled out of the integrals. Due to the fact that they are arbitrary values they can be canceled out. This leaves equation (2.153) in the form:

$$\begin{aligned} -\int_{\Omega^e} \nabla\boldsymbol{\Psi}^{w} : \Bigg(& (\delta\psi^{\rho}\boldsymbol{v}^{n} \otimes \boldsymbol{v}^{n} + \rho^{n}\delta\boldsymbol{\psi}^{v} \otimes \boldsymbol{v}^{n} + \rho^{n}\boldsymbol{v}^{n} \otimes \delta\boldsymbol{\psi}^{v}) + \delta\psi^{\rho}\frac{RT_{mix}}{M}\hat{\mathbf{I}} \\ & -\eta\left(2\nabla_s\delta\boldsymbol{\psi}^{v} - \frac{2}{3}(\nabla\cdot\delta\boldsymbol{\psi}^{v})\hat{\mathbf{I}}\right)\Bigg) + \boldsymbol{\Psi}^{w}\cdot\Bigg(\Big(-\eta\hat{\mathbf{K}}^{-1}\varepsilon\delta\boldsymbol{\psi}^{v} \\ & -\hat{\boldsymbol{\beta}}\left(\delta\psi^{\rho}|\varepsilon\boldsymbol{v}^{n}|\varepsilon\boldsymbol{v}^{n} + \rho^{n}\frac{\varepsilon\boldsymbol{v}^{n}\varepsilon\delta\boldsymbol{\psi}^{v}}{|\varepsilon\boldsymbol{v}^{n}|}\varepsilon\boldsymbol{v}^{n} + \rho^{n}|\varepsilon\boldsymbol{v}^{n}|\varepsilon\delta\boldsymbol{\psi}^{v}\right)\Big) + \delta\psi^{\rho}\boldsymbol{g}\Bigg)\,\mathrm{d}\Omega^{e} \\ = \int_{\Omega^e} \nabla\boldsymbol{\Psi}^{w} : \Bigg(& \rho^{n}\boldsymbol{v}^{n} \otimes \boldsymbol{v}^{n} + \rho^{n}\frac{RT_{mix}}{M}\hat{\mathbf{I}} - \eta\left(2\nabla_s\delta\boldsymbol{\psi}^{v} - \frac{2}{3}(\nabla\cdot\delta\boldsymbol{\psi}^{v})\hat{\mathbf{I}}\right)\Bigg) \\ & \boldsymbol{\Psi}^{w}\cdot\Bigg(\Big(-\eta\hat{\mathbf{K}}^{-1}\varepsilon\boldsymbol{v}^{n} - \hat{\boldsymbol{\beta}}\rho^{n}|\varepsilon\boldsymbol{v}^{n}|\varepsilon\boldsymbol{v}^{n}\Big) + \rho^{n}\boldsymbol{g}\Bigg)\,\mathrm{d}\Omega^{e} \end{aligned} \tag{2.171}$$

$$\boldsymbol{\Psi}^w = \begin{bmatrix} \psi_k^{v_x} \\ \psi_p^{v_y} \end{bmatrix} \tag{2.172}$$

Now equation (2.153) is in matrix form, where indices k and p are for the column of the matrix, indices j, l, and m are for the row of the matrix, and $\delta\rho$ and $\delta\boldsymbol{v}$ are the unknowns being solved for.

In summary, the weakened form of the governing equations implemented in OpenFCST are:

$$\begin{aligned} -\int_{\Omega^e} \delta\boldsymbol{F}_{mass_\alpha} \cdot \nabla\Psi_\alpha^q \,\mathrm{d}\Omega^e + \oint_{\Gamma^e} \Psi_\alpha^q \delta\boldsymbol{F}_{mass_\alpha} \cdot \boldsymbol{n} \,\mathrm{d}\Gamma^e \\ = \int_{\Omega^e} \boldsymbol{F}^n_{mass_\alpha} \cdot \nabla\Psi_\alpha^q \,\mathrm{d}\Omega^e - \oint_{\Gamma^e} \Psi_\alpha^q \boldsymbol{F}^n_{mass_\alpha} \cdot \boldsymbol{n} \,\mathrm{d}\Gamma^e \end{aligned} \tag{2.173}$$

$$\begin{aligned} -\int_{\Omega^e} \nabla\boldsymbol{\Psi}_\alpha^w : \left(\delta\hat{\boldsymbol{F}}_{mom_\alpha} + \delta P_\alpha\hat{\mathbf{I}} - \delta\hat{\boldsymbol{\tau}}_\alpha\right) + \boldsymbol{\Psi}_\alpha^w \cdot \left(\delta\boldsymbol{F}_{por_\alpha} + \delta\psi_\alpha^\rho\boldsymbol{g} + \delta\boldsymbol{D}_\alpha\right) \mathrm{d}\Omega^e \\ + \oint_{\Gamma^e} \left(\delta\hat{\boldsymbol{F}}_{mom_\alpha} + \delta P_\alpha\hat{\mathbf{I}} - \delta\hat{\boldsymbol{\tau}}_\alpha\right) \boldsymbol{\Psi}_\alpha^w \cdot \boldsymbol{n} \,\mathrm{d}\Gamma^e \\ = \int_{\Omega^e} \nabla\boldsymbol{\Psi}_\alpha^w : \left(\hat{\boldsymbol{F}}^n_{mom_\alpha} + P^n_\alpha\hat{\mathbf{I}} - \hat{\boldsymbol{\tau}}^n_\alpha\right) + \boldsymbol{\Psi}_\alpha^w \cdot \left(\boldsymbol{F}^n_{por_\alpha} + \psi_\alpha^\rho\boldsymbol{g} + \boldsymbol{D}^n_\alpha\right) \mathrm{d}\Omega^e \\ - \oint_{\Gamma^e} \left(\hat{\boldsymbol{F}}^n_{mom_\alpha} + P^n_\alpha\hat{\mathbf{I}} - \hat{\boldsymbol{\tau}}^n_\alpha\right) \boldsymbol{\Psi}_\alpha^w \cdot \boldsymbol{n} \,\mathrm{d}\Gamma^e \end{aligned} \tag{2.174}$$

$$\delta\boldsymbol{F}_{mass_\alpha} = \delta\psi_\alpha^\rho\boldsymbol{v}_\alpha^n + \rho_\alpha^n\delta\boldsymbol{\psi}_\alpha^v \tag{2.175}$$

$$\boldsymbol{F}_{mass_\alpha} = \rho_\alpha^n\boldsymbol{v}_\alpha^n \tag{2.176}$$

$$\delta\hat{\boldsymbol{F}}_{mom_\alpha} = \delta\psi_\alpha^\rho\boldsymbol{v}_\alpha^n \otimes \boldsymbol{v}_\alpha^n + \rho_\alpha^n\delta\boldsymbol{\psi}_\alpha^v \otimes \boldsymbol{v}_\alpha^n + \rho_\alpha^n\boldsymbol{v}_\alpha^n \otimes \delta\boldsymbol{\psi}_\alpha^v \tag{2.177}$$

$$\hat{\boldsymbol{F}}_{mom_\alpha} = \rho_\alpha^n\boldsymbol{v}_\alpha^n \otimes \boldsymbol{v}_\alpha^n \tag{2.178}$$

$$\delta P_\alpha = \delta\psi_\alpha^\rho \frac{RT_{mix}}{M_\alpha} \tag{2.179}$$

$$P_\alpha = \rho_\alpha^n \frac{RT_{mix}}{M_\alpha} \tag{2.180}$$

$$\delta\hat{\boldsymbol{\tau}}_\alpha = \delta\eta_\alpha\left(2\nabla_s\boldsymbol{v}_\alpha^n - \frac{2}{3}(\nabla\cdot\boldsymbol{v}_\alpha^n)\hat{\mathbf{I}}\right) + \eta_\alpha\left(2\nabla_s\delta\boldsymbol{\psi}_\alpha^v - \frac{2}{3}(\nabla\cdot\delta\boldsymbol{\psi}_\alpha^v)\hat{\mathbf{I}}\right) \tag{2.181}$$

$$\hat{\boldsymbol{\tau}}_\alpha = 2\eta_\alpha\nabla_s\boldsymbol{v}_\alpha^n - \frac{2}{3}\eta_\alpha\nabla\cdot\boldsymbol{v}_\alpha^n\hat{\mathbf{I}} \tag{2.182}$$

$$\delta\boldsymbol{F}_{por_\alpha} = \begin{cases} 0 & \text{in } \Omega_c \\ -\hat{\mathbf{K}}^{-1}\varepsilon\left(\boldsymbol{v}_\alpha^n\delta\eta_\alpha + \eta_\alpha\delta\boldsymbol{\psi}_\alpha^v\right) \\ \quad -\hat{\boldsymbol{\beta}}\left(\delta\psi_\alpha^\rho|\varepsilon\boldsymbol{v}_\alpha^n|\varepsilon\boldsymbol{v}_\alpha^n + \rho_\alpha^n\dfrac{\varepsilon\boldsymbol{v}_\alpha^n\varepsilon\delta\boldsymbol{\psi}_\alpha^v}{|\varepsilon\boldsymbol{v}_\alpha^n|}\varepsilon\boldsymbol{v}_\alpha^n\right. & \text{in } \Omega_p \\ \quad\quad \left. + \rho_\alpha^n|\varepsilon\boldsymbol{v}_\alpha^n|\varepsilon\delta\boldsymbol{\psi}_\alpha^v\right) \end{cases} \tag{2.183}$$

$$\boldsymbol{F}_{por_\alpha} = \begin{cases} 0 & \text{in } \Omega_c \\ -\eta_\alpha \hat{\mathbf{K}}^{-1} \varepsilon \boldsymbol{v}_\alpha^n - \hat{\boldsymbol{\beta}} \rho_\alpha^n |\varepsilon \boldsymbol{v}_\alpha^n| \varepsilon \boldsymbol{v}_\alpha^n & \text{in } \Omega_p \end{cases} \tag{2.184}$$

$$\delta \boldsymbol{D}_\alpha = \sum_{\beta=1}^{N} (\delta P_\alpha P_\beta + P_\alpha \delta P_\beta) \hat{\boldsymbol{D}}_{\alpha\beta} (\boldsymbol{v}_\beta^n - \boldsymbol{v}_\alpha^n) + P_\alpha P_\beta \hat{\boldsymbol{D}}_{\alpha\beta} (\delta \boldsymbol{\psi}_\beta^v - \delta \boldsymbol{\psi}_\alpha^v) \tag{2.185}$$

$$\boldsymbol{D}_\alpha = \sum_{\beta=1}^{N} P_\alpha P_\beta \hat{\boldsymbol{D}}_{\alpha\beta} (\boldsymbol{v}_\beta^n - \boldsymbol{v}_\alpha^n) \tag{2.186}$$

$$\hat{\boldsymbol{D}}_{\alpha\beta} = \left(P_t \mathscr{D}_{\alpha\beta}^{eff} \right)^{-1} \hat{\mathbf{I}} \tag{2.187}$$

$$\varepsilon = \begin{cases} 1 & \text{in } \Omega_c \\ 0 < \varepsilon \leq 1 & \text{in } \Omega_p \end{cases} \tag{2.188}$$

$$\Psi_\alpha^q = \psi_{\alpha,i}^\rho \tag{2.189}$$

$$\delta \psi_\alpha^\rho = \sum_{j=1}^{N} \delta \rho_{\alpha,j} \psi_{\alpha,j}^\rho \tag{2.190}$$

$$\delta \boldsymbol{\psi}_\alpha^v = \begin{bmatrix} \sum_{l=1}^{N} \delta v_{\alpha,l}^x \psi_{\alpha,l}^{v_x} \\ \sum_{r=1}^{N} \delta v_{\alpha,r}^y \psi_{\alpha,r}^{v_y} \end{bmatrix} \tag{2.191}$$

$$\boldsymbol{\Psi}_\alpha^w = \begin{bmatrix} \psi_{\alpha,k}^{v_x} \\ \psi_{\alpha,p}^{v_y} \end{bmatrix} \tag{2.192}$$

2.7 Implementation

2.7.1 Discretization

OpenFCST utilizes the deal.II FEA library [100, 101] for handling the grid, global and adaptive refinement, finite element shape functions, and linear solvers. Due to limitations with the deal.II FEA library used by OpenFCST only quadrilaterals and quadrilateral prisms are able to be used in 2D and 3D respectively.

For incompressible flows Reddy remarks, "In order to prevent an overconstrained system of discrete equations, the interpolation used for pressure must be at least one order lower than that use for the velocity field" [99]. Donea and Huerta make a similar suggestion for compressible flows, but add that this is not a requirement like it is for incompressible flows [102]. Taylor-Hood elements [103] match this criteria and are known to give a stable solution for incompressible flows in the Stokes flow regime. In conclusion, first order and second order Lagrange shape functions will be used for the density and velocity test functions respectively.

2.7.2 Linear Solver

Due to the nonlinear nature of the equations and stability issues when trying to use an iterative solver direct solvers were used instead. The direct solvers UMFPACK (Unsymmetric MultiFrontal Package) [104] and MUMPS (MUltifrontal Massively Parallel sparse direct Solver) [105, 106] were used. UMFPACK is a direct solver for solving nonsymmetric matrices using the multifrontal LU factorization. UMFPACK has been found to be extremely stable at solving problems in OpenFCST, however it is not capable of solving the equations in parallel. As a result, it can be slow for larger problems, as is the case for 3D problems.

Recently, MUMPS, a parallel solver, has been integrated into OpenFCST. MUMPS is controlled in deal.II through the PETSc (Portable, Extensible Toolkit for Scientific Computation) library [107–109]. As well, when deal.II uses PETSc for parallel computing it also requires p4est [110] and METIS [111]. p4est and METIS are used by deal.II to distribute large meshes across multiple processors when performing parallel computing.

MUMPS was not used for running all simulations because at times there have been stability issues when solving some problems. For example, the stability has been found to be dependent on the number of threads used to solve the problem. The mesh structure has also been found to be factor, as at times by simply changing the mesh MUMPS either has an easier or more difficult time solving the problem. Finally, another believed to be factor in stability is the convection term as simulations that are done only in porous layers have shown to be more stable than those that do not. For single species simulations, MUMPS has been found to be more stable when equation (2.173) is multiplied by 10^{-4}. In cases when MUMPS has stability problems, UMFPACK has been used to solve the problem on a single thread.

2.7.3 Numerical Implementation

The numerical implementation of the isothermal compressible multi-component mass transport equations were implemented into OpenFCST by Valentin Zingan and Chad Balen. Valentin Zingan derived the equations and implemented the isothermal compressible multi-component mass transport equation class. Chad Balen re-derived all volume averages, linearization, and weak formulations of the governing equations to confirm that they were correct. Chad Balen then went and rebuilt the equation and application class so the code was generalized to be able to run any problem. During this time, Chad Balen extended the viscous stress tensor term, as Valentin Zingan had assumed constant dynamic viscosity for each species. To do this Chad Balen implemented Wilke and Kerkhof and Geboers' viscosity models to account for the partial viscosity being a function of density in the viscous stress tensor.

Chapter 3

Mass Transport Simulations and Validation

3.1 Introduction

To ensure that the governing equations were implemented correctly results were compared against either experimental, numerical, or analytical results previously done in literature. The first benchmark compares numerical results for a lid driven cavity problem. Lid driven cavity simulations are common for testing fluid flow due to shear from the uniform movement of a lid. Next a backward-facing step simulations was compared to experimental data. A backward-facing step problem provides validation for convective terms by determining the separation point in the flow and comparing to experimental data. These experiments are highly controlled such that the flow can be assumed to be 2D and fully developed. Next a simulation of the mass transport in the through-plane direction of a GDL was performed by comparing results to experimental values. This was done to validate the volume averaging and accuracy of the model when handling a channel and porous media domain simultaneously. Finally, a Stefan tube diffusion simulation was performed and results were compared to the analytical Maxwell-Stefan solution. This test provides confirmation that the governing equations can accurately describe this purely diffusive type of mass transport, as well as the multi-component aspect of the governing equations.

3.2 Lid Driven Cavity

Lid driven cavity flow is a very common numerical simulation used for validating fluid flow software. This is because the square geometry and boundary conditions are simple to implement and accurate results can be achieved quickly to compare against the work of others. The fluid flow provides interesting results as the shearing effect from the uniform velocity of the moving lid results in multiple vortices forming inside the square cavity. Validation

was done by comparing numerical results of the velocity profiles from OpenFCST along the geometric centers against the tabulated numerical results of Ghia et al. [112].

3.2.1 Domain

A 2D square domain was considered. Figure 3.1 displays a schematic of the domain considered. The moving lid is represented by a constant velocity along the upper wall of the domain, while the rest of the boundaries are treated as walls. The one issue with the boundary conditions is that they do not provide any necessary information about the density of the fluid. To resolve this, a small segment of the mesh along the lower boundary has a density boundary condition applied instead. Ghia et al. used uniform meshes of either 128×128 or 256×256 cells. To best compare numerical results an initial mesh of 128×128 cells is used, then the mesh is globally refined and final values of the 256×256 cell mesh were used for comparison to Ghia et al.

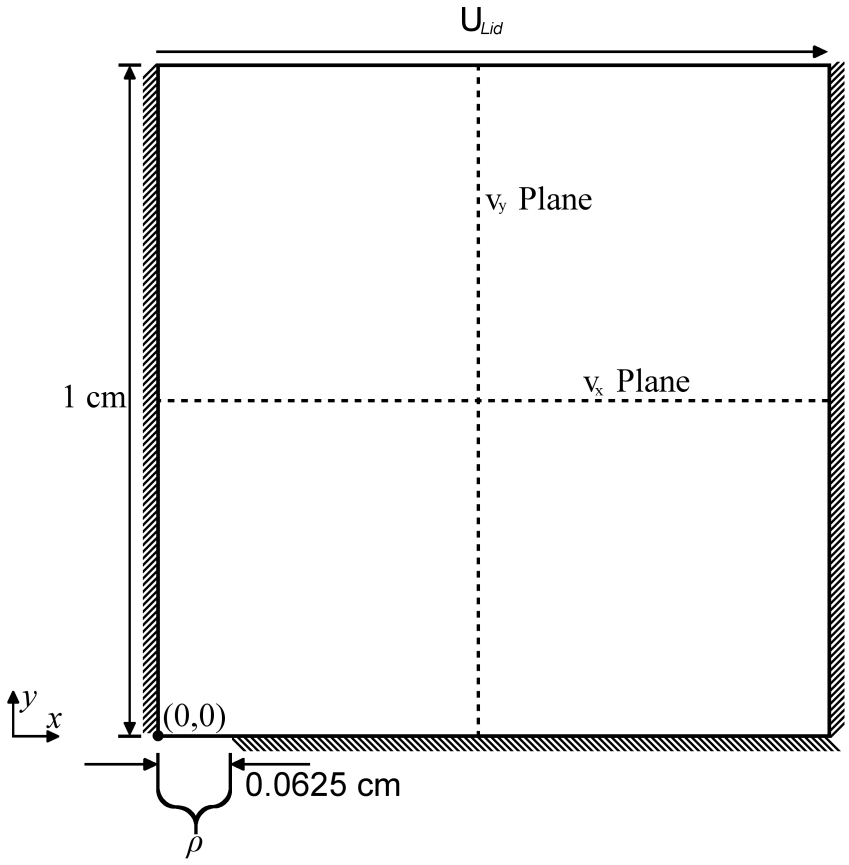

Figure 3.1 – Lid driven cavity domain (not to scale)

Ghia et al. reported results for a range of Reynolds numbers from $100 \leq Re \leq 10000$.

The Reynolds number is defined as:

$$Re = \frac{\rho\, U_{Lid}\, d_h}{\eta^0} \tag{3.1}$$

where U_{Lid} is the uniform velocity along the top wall ($\mathrm{cm\,s^{-1}}$), and d_h is the hydraulic diameter. For this case, the hydraulic diameter is the length of one side of the square, i.e. 1 cm. It was found that convergence was more easily achieved if density was held constant, and the velocity of the upper boundary was changed to give the necessary Reynolds number. Air was selected as the gas species and the temperature and pressure was held constant at 293.15 K and 101 325 Pa.

3.2.2 Boundary Conditions

In a lid driven cavity flow the fluid is pulled across the top of the cavity resulting in flow due to shearing forces. During this process no flow leaves the cavity, so this can be represented by prescribing a uniform velocity in the x-direction while using $0\,\mathrm{cm\,s^{-1}}$ in the y-direction. This is represented mathematically as:

$$v_x = U_{Lid} \qquad \text{on } x \in [0.0, 1.0],\ y = 1.0 \tag{3.2}$$

$$v_y = 0\,\mathrm{cm\,s^{-1}} \qquad \text{on } x \in [0.0, 1.0],\ y = 1.0 \tag{3.3}$$

where U_{Lid} is 15.05, 60.21, 150.5, and $481.7\,\mathrm{cm\,s^{-1}}$ for Reynolds numbers of 100, 400, 1000, and 3200 respectively.

The side walls and bottom walls had a no-slip and no-penetration boundary condition prescribed, i.e. $v_x = v_y = 0\,\mathrm{cm\,s^{-1}}$. A density boundary condition was also required for a convergent unique solution. This was done by applying a Dirichlet density boundary condition on a small segment of the lower boundary adjacent to the origin, expressed as:

$$\rho = 0.001\,204\,\mathrm{g\,cm^{-3}} \qquad \text{on } x \in [0.0, 0.0625],\ y = 0.0 \tag{3.4}$$

3.2.3 Results

Figure 3.2 displays the normalized velocity profiles along the geometric center of the domain for each Reynolds number. To properly compare velocity profiles with the data from Ghia et al. the velocity in the solutions was normalized by dividing by U_{Lid}. In Figure 3.2, the velocity profiles in the x and y-direction were actually taken along different planes. The x-component of velocity was plotted along the vertical geometric center of the cavity, i.e. along the y-axis at $x = 0.5$, while the y-component of velocity was plotted along the horizontal geometric center of the cavity, i.e. along the x-axis at $y = 0.5$. These planes, for each component of the velocity, are shown on Figure 3.1.

Figure 3.2 shows good agreement with the tabulated values from Ghia et al. There are two points where there is a discrepancy from the results of Ghia et al. In Figure 3.2d) the x-component of velocity near the center of the square shows a jump from the expected linear profile of this region. Ghia et al. makes no mention of this odd jump in the x-component of velocity near the center. As well, their own figures, that graphically display the velocity profiles, do not display this. Instead they say, "The near-linearity of these velocity profiles in the central core of the cavity is indicative of the uniform vorticity region that develops here for large Re" [112]. This suggests that this data point is the result of a mistake in the table data and not representative of the actual velocity they obtained at this point.

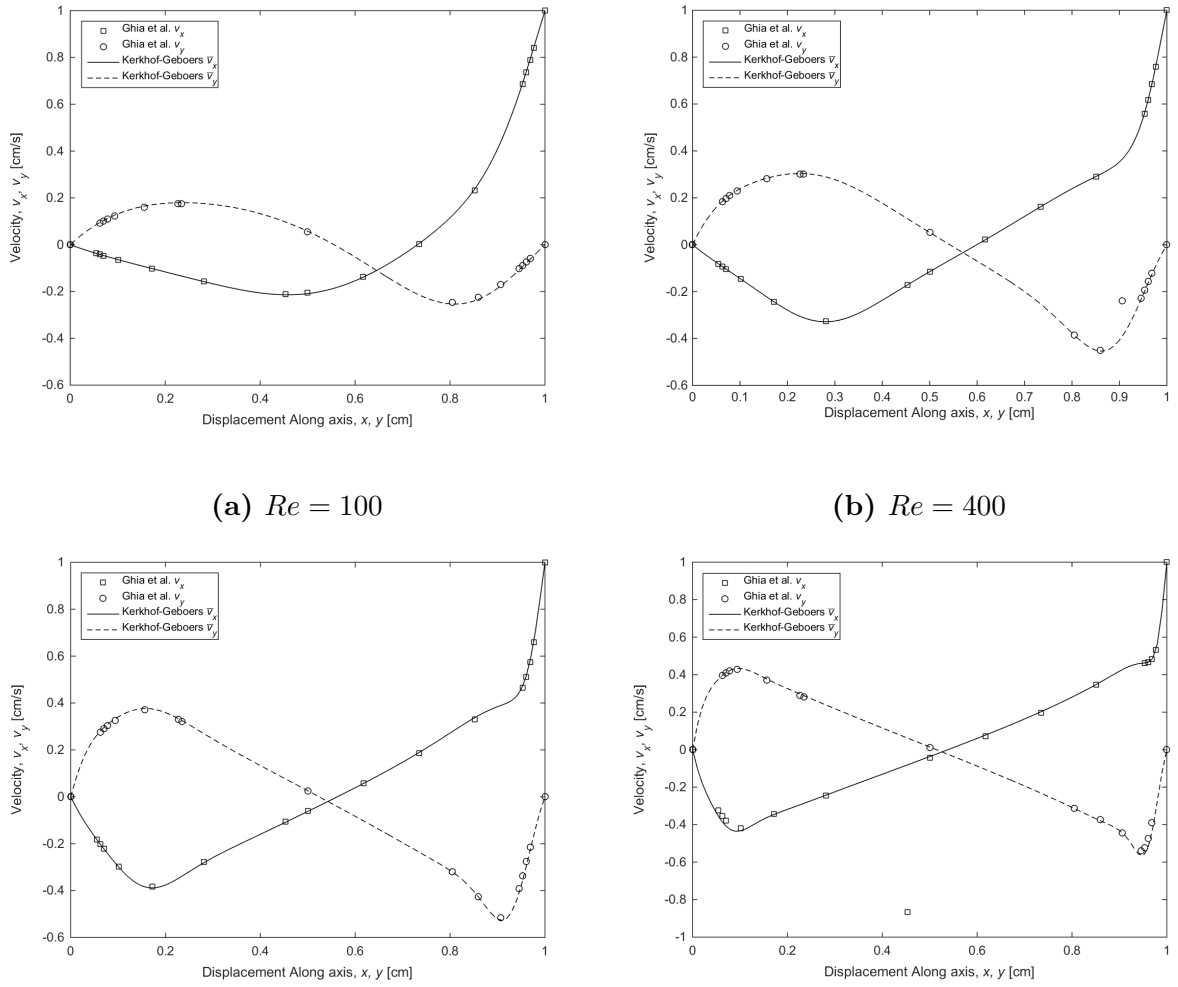

(a) $Re = 100$ **(b)** $Re = 400$

(c) $Re = 1000$ **(d)** $Re = 3200$

Figure 3.2 – Comparison of Ghia et al. numerical results and implementation of Kerkhof-Geboers equations in OpenFCST for a lid driven cavity flow for low Reynolds numbers

The other discrepancy is in Figure 3.2b) where Ghia et al. gave a value of $(0.9063, -0.23827)$ for the y-component of velocity. This point does not follow the trend for the y-component of velocity in this region and once gain is not displayed in their graphical representation of the data points. Further this jump does not appear at higher or lower Reynolds numbers, rather a linear profile is also seen in these regions.

With the exception of these two points the results from the simulation done in OpenFCST show very good approximation to that of Ghia et al. A maximum error in the velocity components compared to Ghia et al.'s reported results was found to be $0.05\,\mathrm{cm\,s^{-1}}$, the points associated with the largest error were the data points closest to the walls. This error is most likely attributed to sharp gradients near the wall surfaces where a much finer mesh is required. Differences in values can be attributed to the different numerical schemes used to solve the governing equations. Ghia et al. used a finite difference method with an upwind differencing scheme on the convective terms, which can lead to artificial diffusion.

Figure 3.3 displays the contours and magnitude of velocity profile for the domain of the lid driven cavity simulation at a Reynolds number of 3200. Figure 3.3 shows good agreement with the work of Ghia et al., as it shows all the same features as Ghia et al.'s contour plot. These results suggest that the Kerkhof and Geboers equations have been implemented correctly.

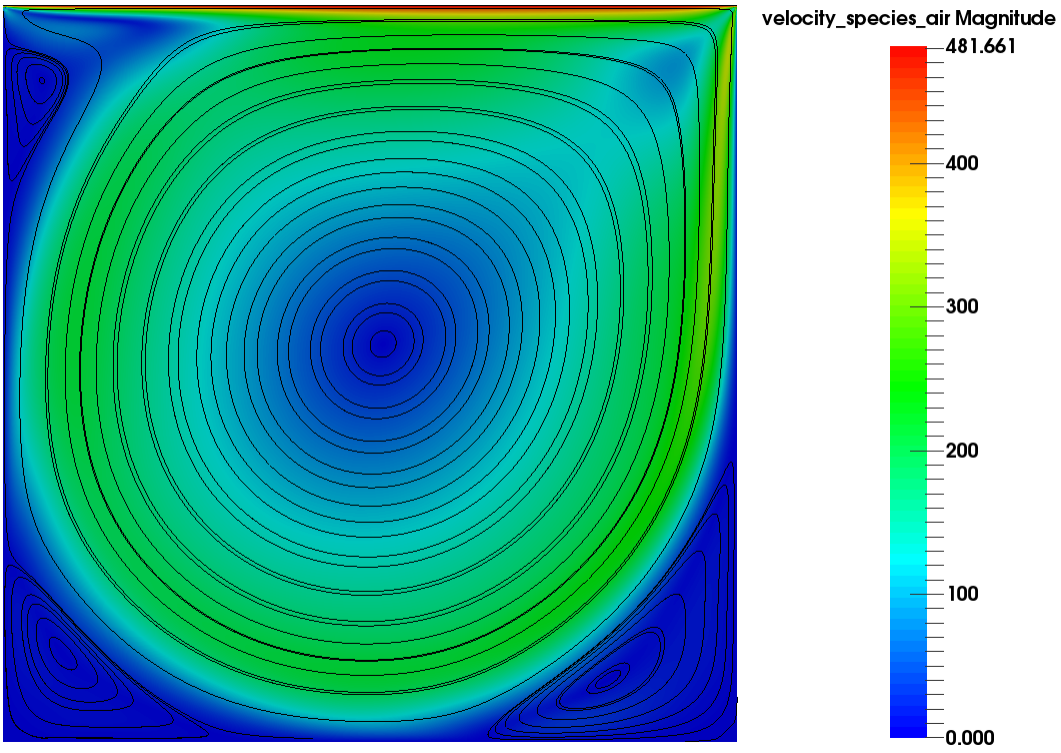

Figure 3.3 – Lid driven cavity contours and velocity magnitude, $Re = 3200$

3.3 Backward-facing Step

Flow separation is a phenomenon where the boundary layer detaches from the object resulting in a recirculation region where vortices form. Armaly et al. [113] provides data for a wide range of Reynolds number ($70 < Re < 8000$). They also setup the experiment such that at low Reynolds numbers ($Re \lesssim 400$) the flow is purely 2D and enters the experiment as fully developed and leaves fully developed. These results are therefore ideal to validate the governing equations.

3.3.1 Domain

For simplicity only a 2D simulation was considered, and quantitative comparisons were done with Armaly et al.'s experimental data up to a Reynolds number of 400. Figure 3.4 displays a schematic of the domain considered. With the exception of the entrance length to the backward-facing step length, these dimensions are the same as those used by Armaly et al. They designed the experiment such that the velocity profile before the backwards step was always 2D and fully developed from $70 < Re < 8000$. To reduce computational cost, the correct parabolic velocity profile was prescribed at the inlet.

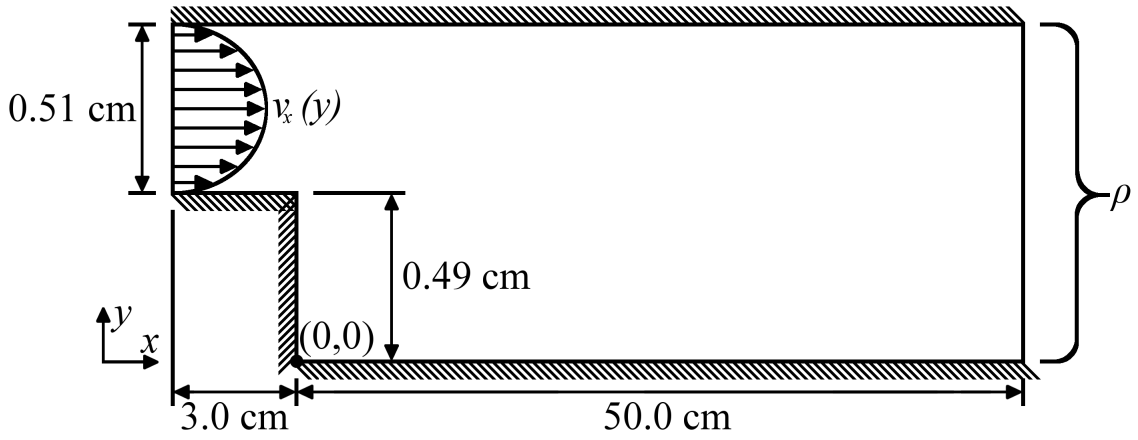

Figure 3.4 – Backward-facing step domain (not to scale)

The full exit length of the channel after the backwards step, was considered to ensure that the flow achieves fully developed flow far down from the backwards step. A much more refined mesh was used in the first 15 cm after the backwards step. This was because this region is where flow is most likely to separate based on Armaly et al.'s experimental results. Figure 3.5 shows the mesh for the entrance and a portion of the separation region for the backward-facing step simulation. An initial level of global refinement was performed on this mesh before numerically solving. Adaptive refinment was used, where 30% of the cells with

the largest error where refined at each adaptive step. Adaptive refinement was done five times giving a final mesh of at least 168 000 cells.

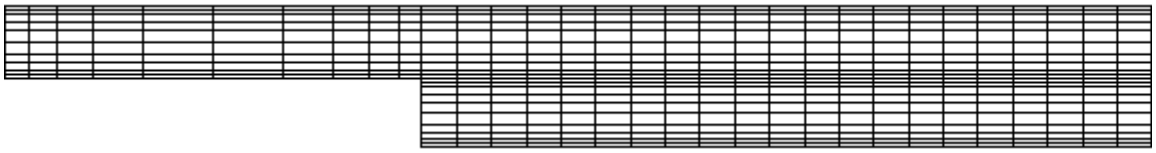

Figure 3.5 – Backward-facing step entrance and a portion of the separation region of mesh

Armaly et al. reports all experimental data as a function of the Reynolds number, for this reason any gas species, density, and velocity can be used as long as they produce the same Reynolds number. The Reynolds number for a backward-facing step is defined as follows:

$$Re = \frac{\rho\, U_{avg}\, d_h}{\eta^0} \tag{3.5}$$

where U_{avg} is the average inlet velocity ($\mathrm{cm\,s^{-1}}$). For a backwards-facing step the hydraulic diameter is equivalent to twice the height of the channel inlet, i.e. $d_h = 1.02\,\mathrm{cm}$. Air was used as the gas in the backward-facing step at a temperature and pressure of 293.15 K and 101 325 Pa. This gave a constant density and viscosity for all Reynolds numbers in the simulation, and as a result the velocity at the inlet was adjusted to give the necessary Reynolds number.

3.3.2 Boundary Conditions

A parabolic velocity profile was prescribed at the inlet as follows:

$$v_x(y) = U_{max}(-7.321006 + 22.189349\,y - 14.792899\,y^2) \quad \text{on } x = -3,\ y \in [0.49, 1.01] \tag{3.6}$$

$$v_y = 0\,\mathrm{cm\,s^{-1}} \quad \text{on } x = -3,\ y \in [0.49, 1.01] \tag{3.7}$$

where U_{max} is the maximum velocity at the center of the parabola ($\mathrm{cm\,s^{-1}}$). The Reynolds number was used to determine the required average velocity, then the relation $U_{max} = \frac{3}{2}U_{avg}$ was used to calculate the maximum velocity.

A Dirichlet density boundary condition was prescribed at the outlet. As mentioned previously, air was assumed to be at a temperature and pressure of 293.15 K and 101 325 Pa. This gives a density at the outlet of:

$$\rho = 0.001\,204\,\mathrm{g\,cm^{-3}} \quad \text{on } x = 50,\ y \in [0.00, 1.01] \tag{3.8}$$

Finally, for all other boundaries a no-slip and no-penetration boundary conditions was applied, i.e. $u_x = u_y = 0\,\mathrm{cm\,s^{-1}}$.

3.3.3 Results

To validate the implementation of the governing equations the ratio of the lower reattachment length, x_1, to the height of the backwards-facing step, S, was compared to experimental results for $Re < 400$. The reattachment length was obtained during post-processing using Paraview [114]. The x-component of velocity was plotted along the x-axis at $y = 0.001\,\text{cm}$, and the position where the velocity intercepted $0\,\text{cm}\,\text{s}^{-1}$ was determined.

The backward-facing step results are shown in Figure 3.6. At a Reynolds number of approximately 400 a secondary separation region appears along the upper channel wall, resulting in the flow no longer being 2D. For this reason, only experimental data below a Reynolds number of 400 was compared. For Reynolds numbers less than 350, the numerical results show good agreement with the experimental values. Similarly to Armaly et al.'s own numerical results, between $350 \leq Re \leq 400$ the numerical results under-predicted the reattachment length from the experimental data. Although grid independence was not performed for these results, it should be noted that Armaly et al's numerical results where obtained in the grid independent region for Re$\leq$ 400 with a grid density of 45 by 45. This is significantly less nodes than the dofs used to solve this problem here.

Figure 3.7 displays the magnitude of velocity profile for the entrance and separation region for a Reynolds number of 390. Figure 3.7 shows a parabolic velocity profile in the entrance region and begins to become fully developed after the separation region as expected from Armaly et al.'s results. As well, the separation region can clearly be seen.

3.4 Permeability of a GDL

The anisotropic properties of a gas diffusion layer (GDL) was recently tested at the Energy Systems Design Laboratory (ESDL) [115, 116]. Mangal used a diffusion bridge to determine the through-plane permeability of a GDL [115, 116]. The domain consists of two different materials with volume averaging required in the GDL layer. This tests the governing equations ability to be valid in two different domains, and confirms volume averaging was applied correctly. Mangal's data for a Toray 090 (untreated) GDL with a thickness of 262 µm was used for validation, as this sample has the most data provided for the necessary boundary conditions.

The through-plane permeability experiment determined the material properties of the GDL in its thickness direction. This was done by varying the flow rate at the inlet between 0 and $2\,\text{L}\,\text{min}^{-1}$ in 10 equal intervals. The pressurized nitrogen then flowed through the GDL to the low pressure channel, which was open to ambient conditions of approximately 298.15 K and 101 000 Pa. This setup allowed for the pressure difference between the high

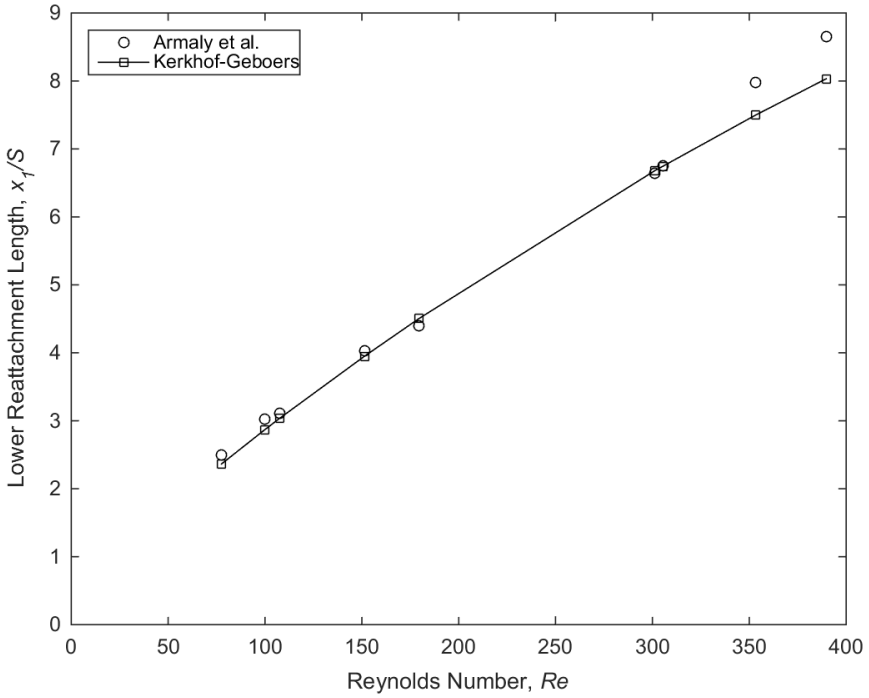

Figure 3.6 – Comparison of experimental results and implementation of Kerkof-Geboers equations for a backward-facing step

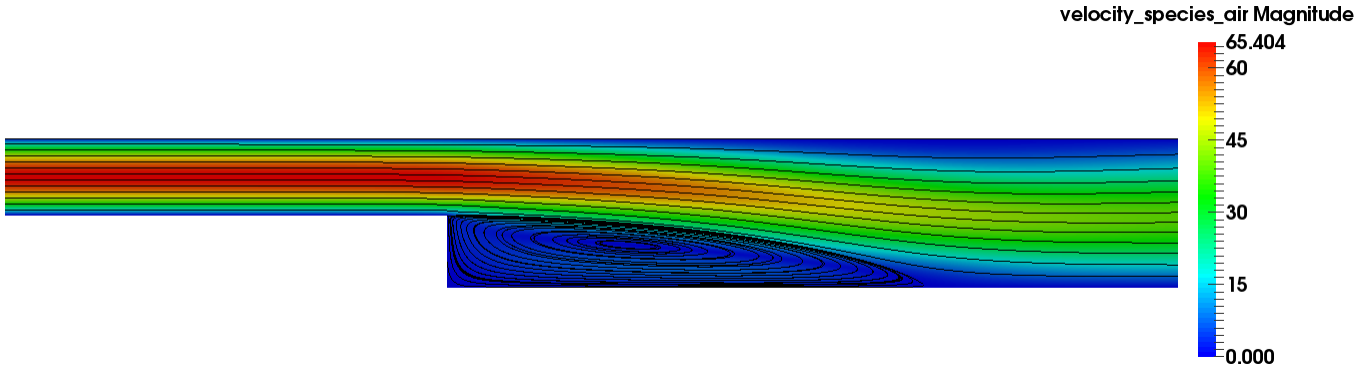

Figure 3.7 – Backward-facing step magnitude of velocity profile at $Re = 300$

and low pressure channels to be determined. Using this information with a 1D model of the governing equations in the GDL Mangal calculated the through-plane permeability. This permeability with the boundary conditions discussed below were used, and the model was validated by comparing the inlet pressure from the simulations to the experimental values.

3.4.1 Material Properties

The porosity and permeability are required for the Toray 090 (untreated) GDL. Mangal determined experimental values assuming a 1D model of the diffusion bridge. When Mangal determined the permeability and he did not account for volume averaging in his equations. This leads to a discrepancy between the permeability tensor values Mangal obtained, from those that are required for OpenFCST. As a result, based on equation (2.101) the following permeability tensors were used instead:

$$\hat{\mathbf{K}} = \varepsilon \hat{\mathbf{K}}_{Mangal} = \begin{bmatrix} 7.125 \times 10^{-8} & 0.0 & 0.0 \\ 0.0 & 7.125 \times 10^{-8} & 0.0 \\ 0.0 & 0.0 & 6.0 \times 10^{-8} \end{bmatrix} \tag{3.9}$$

$$\hat{\boldsymbol{\beta}} = \frac{\hat{\boldsymbol{\beta}}_{Mangal}}{\varepsilon^2} = \begin{bmatrix} 2222 & 0.0 & 0.0 \\ 0.0 & 2222 & 0.0 \\ 0.0 & 0.0 & 4558 \end{bmatrix} \tag{3.10}$$

where the subscript $\hat{\mathbf{K}}_{Mangal}$ and $\hat{\boldsymbol{\beta}}_{Mangal}$ represents the intrinsic and forchheimer permeability tensor values reported by Mangal in [115, 116] respectively.

3.4.2 Domain

Figure 3.8 displays a schematic of the domain considered. For the experiments, Mangal stacked three GDLs on top of each other, and reported a thickness of 0.083 cm for the Toray 090 (untreated). In the numerical simulations this was represented in the simulation by a single GDL of the equivalent thickness and no contact effects between the the individual GDL layers was assumed. The diffusion bridge consists of two long rectangular channels. Resulting in fully developed flow before entering the GDL stack and far down the channel after leaving the stack. In the experiment, Mangal laminated three square GDLs on top of each with a circular hole on both side of the lamination sheet. This allowed for the nitrogen to pass through a circular hole in the lamination sheet and across the GDL. In the numerical simulations this is represented by the the two channels being separated by a cylindrically shaped GDL. This cylindrical GDL has a diameter of 0.95 cm and a height of 0.083 cm. To reduce computational expense, less of the channel was considered in the entrance region, and a parabolic profile was prescribed as the flow should be fully developed before it reaches the GDL. A symmetric boundary condition was also applied, reducing the domain considered by half.

The initial mesh used can be seen in Figure 3.9. Adaptive refinement was used, where 10% of the cells with the largest error where refined at each adaptive step. The reason for not using 30%, as done in previous simulations, is because this is a 3D simulation and using 10% has a similar effect as using 30% in 2-dimensions, i.e. the number of dofs approximately

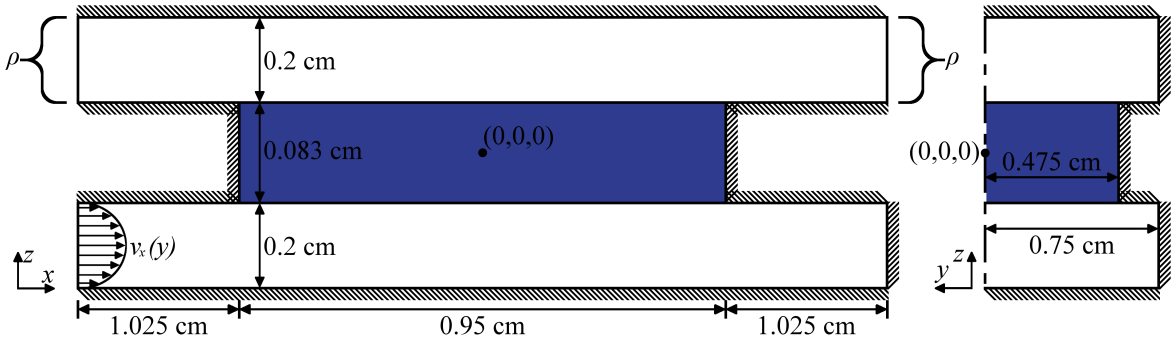

Figure 3.8 – Domain for through-plane diffusion bridge with a cylindrically shaped GDL (not to scale)

doubles at each refinement level. To be more precise, in the 3D case it is closer to a factor of 1.75 rather than 2. Adaptive refinement was done three times giving a final mesh of approximately 37 500 cells.

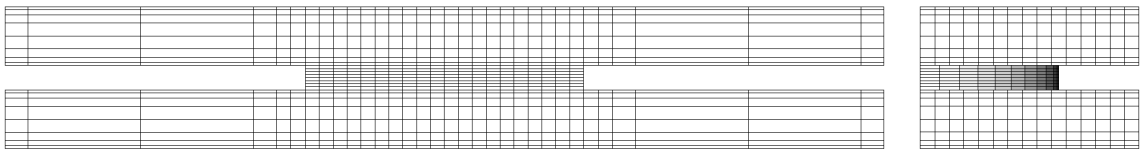

(a) Mesh in XZ-plane **(b)** Mesh in YZ-plane

Figure 3.9 – Initial mesh for the through-plane permeability simulation

3.4.3 Boundary Conditions

A parabolic velocity profile was prescribed at the inlet as follows:

$$v_x(z) = U_{max}(-1.002225 - 28.3\,z - 100\,z^2) \qquad \text{on } x = -1.5,\ y \in [-0.75, 0],\ z \in [-0.2415, -0.0415] \tag{3.11}$$

$$v_y = v_z = 0\,\mathrm{cm\,s^{-1}} \qquad \text{on } x = -1.5,\ y \in [-0.75, 0],\ z \in [-0.2415, -0.0415] \tag{3.12}$$

where U_{max} is 16.67, 33.33, 50.00, 66.67, 83.33, 100.0, 116.7, 133.3, 150.0, and 166.67 $\mathrm{cm\,s^{-1}}$ for flow rates of 0.2, 0.4, 0.6, 0.8, 1.0, 1.2, 1.4, 1.6, 1.8, and 2.0 $\mathrm{L\,min^{-1}}$ respectively. As previously discussed, U_{max} is the maximum velocity at the center of the parabola and can be related to the average velocity calculated from the flow rate at the inlet.

A Dirichlet density boundary condition was prescribed at the outlet. As mentioned previously, nitrogen was assumed to be at an approximate temperature and pressure of

293.15 K and 101 000 Pa. This gives a density at the outlet of:

$$\rho = 0.001\,141\,\mathrm{g\,cm^{-3}} \qquad \text{on } x = 50,\ y \in [0.00, 1.01] \tag{3.13}$$

Only half of the domain was considered, so a symmetric boundary condition for the z-component of velocity was prescribed along this boundary. The boundary condition can be represented mathematically as:

$$\frac{\partial v_z}{\partial z} = 0 \qquad \text{on } x \in [-1.5, 1.5],\ y \in [-0.2415, 0.2415],\ z = 0.0 \tag{3.14}$$

Finally, for all other boundaries a no-slip and no-penetration boundary conditions was applied, i.e. $u_x = u_y = 0\,\mathrm{cm\,s^{-1}}$.

3.4.4 Results

To validate the model the pressure determined at the inlet from the simulations were plotted against the different flow rates and compared to the experimental results. Figure 3.10 displays the through-plane permeability results from the experiment and simulation. Mangal reported that the error, as reported by the manufacturers, in the pressure transducers is 0.05%. The numerical results agree with the experimental values, validating the governing equations. As well, this confirms that the use of a 1D model for determining the through-plane permeability of the GDL is accurate.

Figure 3.11 displays the total pressure and velocity profiles at the symmetric boundary surface. The pressure drop occurs entirely through the GDL and there is no significant drop in pressure through the channels themselves. The velocity profiles show a circulation region at the far end of the GDL-channel interface region. Figure 3.12 gives a better visualization of why this is occurring. The flow is circulating around the edge of the GDL-channel interface, and then moving towards the center of this interface. It should be noted that the 1D model never accounted for these velocity effects that occur in channel effects into account and still show accurate comparable results to the numerical simulations.

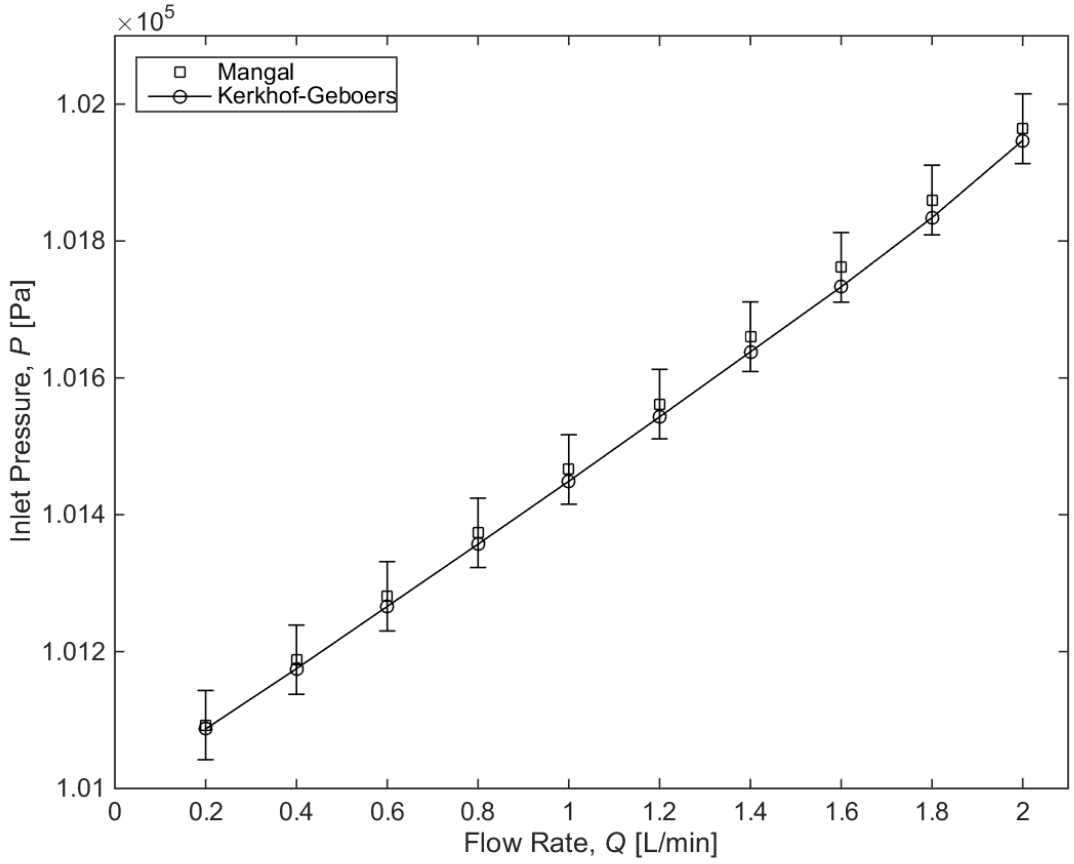

Figure 3.10 – Comparison of experimental results and implementation of Kerkof-Geboers equations for through-plane permeability of a GDL

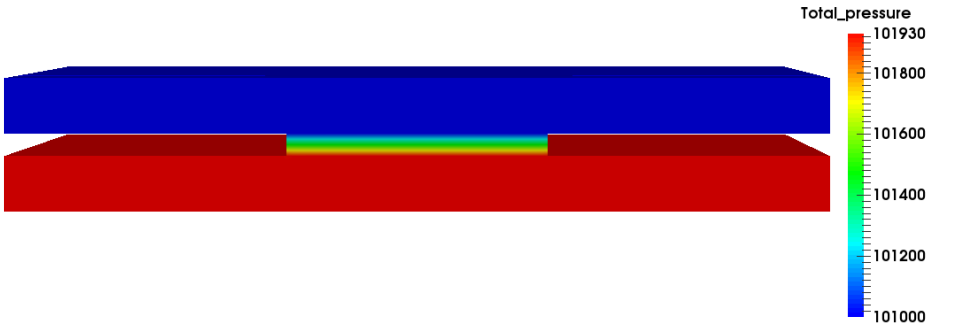

(a) Total Pressure (Pa)

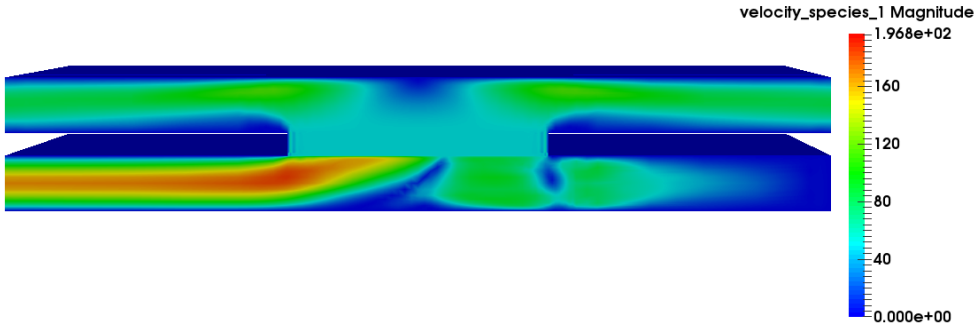

(b) Magnitude of velocity ($\mathrm{cm\,s^{-1}}$)

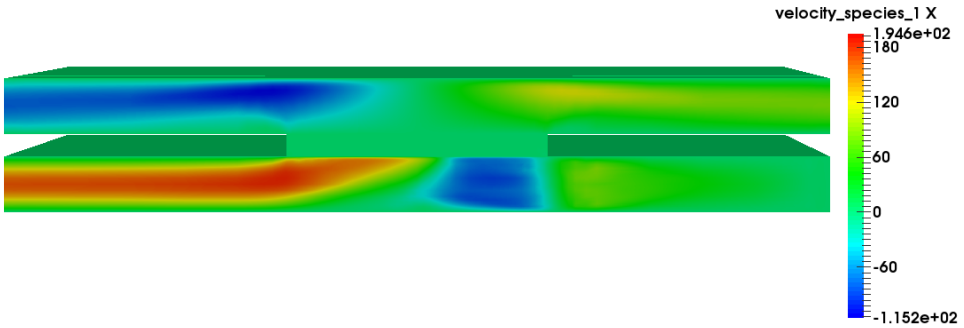

(c) X-component of velocity ($\mathrm{cm\,s^{-1}}$)

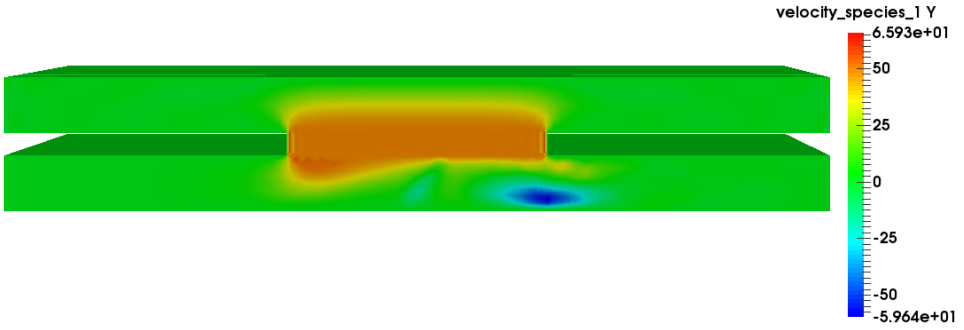

(d) Y-component of velocity ($\mathrm{cm\,s^{-1}}$)

Figure 3.11 – Numerical results in XZ-plane at origin for through-plane permeability simulation at $2.0\,\mathrm{L\,min^{-1}}$

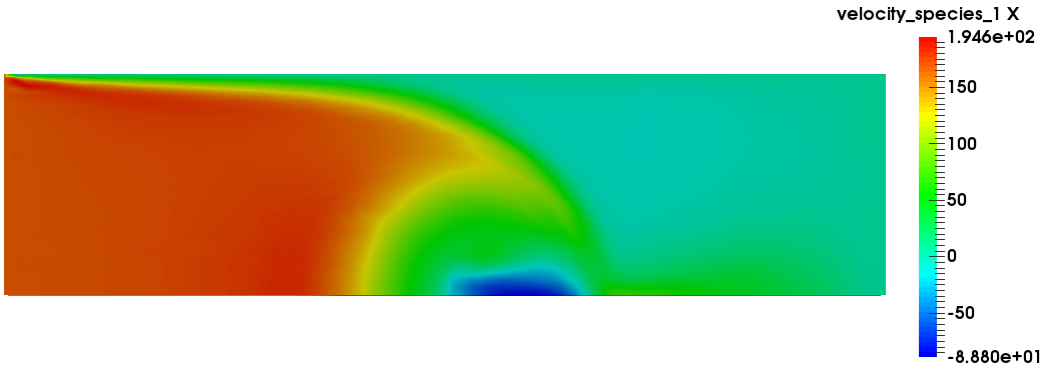

Figure 3.12 – X-component of velocity in XY-plane at $z = -0.1415\,\text{cm}$ for through-plane permeability simulation at $2.0\,\text{L}\,\text{min}^{-1}$

3.5 Stefan Tube Diffusion

Stefan tube experiments are useful for experimentally determining the diffusion coefficients between species. They also serve as good experimental data for validating the multi-component mass transport aspect of the governing equations. Due to the flow in the Stefan tube not containing significant inertial, convection, or shear stress effects a 1D analytical solution to the Maxwell-Stefan equations can be derived that shows good approximation to the experimental data.

Carty and Schrodt [117] experimentally investigated the isothermal steady-state diffusion of an acetone-methanol-air mixture in a Stefan tube to determine the validity of the Maxwell-Stefan equations. Since their intention was validating the Maxwell-Stefan equations, they provide all the necessary data and boundary conditions to reproduce their results numerically. The reason Carty and Schrodt used an acetone-methanol-air mixture was because of the dissimilarities between the binary diffusion coefficients for all gas species, so the problem cannot be simplified to a binary diffusion problem.

3.5.1 Domain

Figure 3.13a) displays a schematic of the domain. For the experimental data the length of the Stefan tube was 24.25 cm. However, when Carty and Schrodt plotted their data they used a length of 23.8 cm to remove entrance effects. The boundary conditions assume no entrance effects, for this reason in the simulations a Stefan tube length of 23.8 cm was used. The width of the Stefan tube in the experiment was 5.08 cm.

If polar coordinates are used, the system can be assumed to be axisymmetric and a 2D domain can be considered. Due to the fact that only the Cartesian coordinates form of

Kerkhof and Geboers' model has been implemented, then a 3D simulation would normally be required. Markham and Rosenberger determined from numerical simulations that radial deviations deviated from the 1D model by less than 1% up to a Peclet number of 1 [118]. For this reason, it is expected that if Cartesian coordinates are used to represent this problem then the results should still collapse to the results of the 1D, which the model is being compared to. As well, symmetry was applied, so only the right half of the domain of the tube was considered. Stefan tube experiments are setup so that the diffusing species exist as a liquid at the bottom of the tube and evaporate out of the tube. This can create problems in numerical simulations, since the domain of the problem changes with time as the liquid-vapour interface level changes. Carty and Schrodt took care to ensure that as the acetone-methanol liquid mixture evaporated, the liquid-vapour interface level was held constant. For this reason, this does not need to be considered.

The initial mesh used can be seen in Figure 3.13b). Adaptive refinement was used, where 30% of the cells with the largest error where refined at each adaptive step. Adaptive refinement was done four times giving a final mesh with 6288 cells.

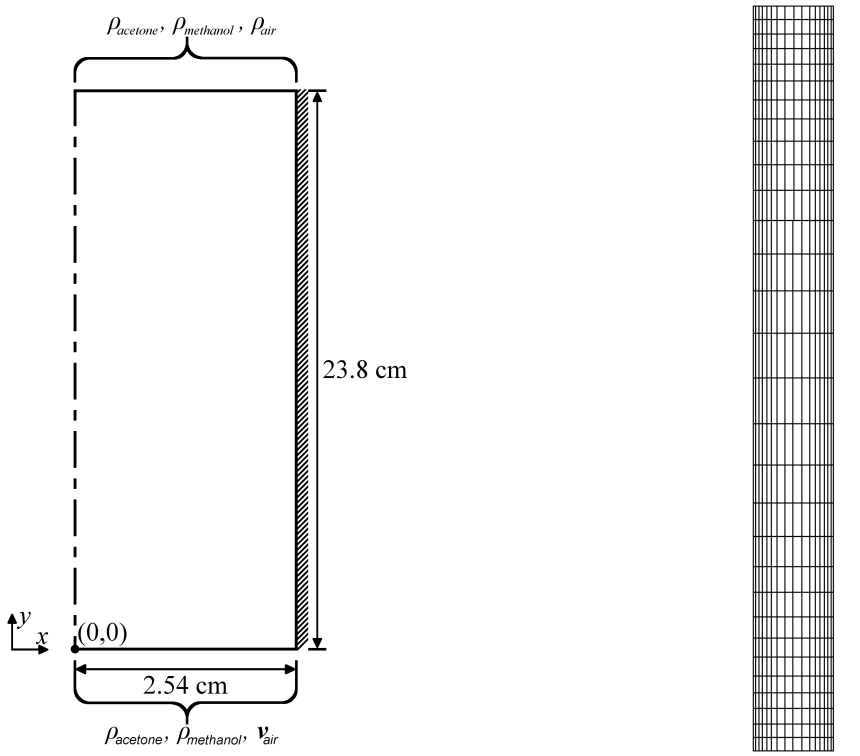

(a) Domain (not to scale) **(b)** Mesh

Figure 3.13 – Stefan tube domain and mesh

3.5.2 Boundary Conditions

Carty and Schrodt maintained a constant temperature and pressure of 328.5 K and 745.2 mmHg (99 335.15 Pa [119]), and considered air as a pure component due to the diffusion coefficients for acetone and methanol in oxygen and nitrogen being nearly the same. Three species are therefore considered for diffusion: acetone, methanol, and air.

Carty and Schrodt assumed that there was neither acetone or methanol at the entrance, only air. As discussed earlier, the length of tube used was 23.8 cm to remove entrance effects so Dirichlet density boundary conditions were prescribed for all gas species at the inlet as follows:

$$\rho_{acetone} = \rho_{methanol} = 0\,\mathrm{g\,cm^{-3}} \qquad \text{on } x \in [0, 2.54],\ y = 23.8 \tag{3.15}$$

$$\rho_{air} = 1.0534 \times 10^{-3}\,\mathrm{g\,cm^{-3}} \qquad \text{on } x \in [0, 2.54],\ y = 23.8 \tag{3.16}$$

Carty and Schrodt estimated the molar fractions of acetone and methanol at the liquid-vapour interface to be 0.319 and 0.528 respectively. Dirichlet boundary conditions for the acetone and methanol were prescribed at the liquid-vapour interface. Since air cannot pass into the liquid-vapour interface, a Dirichlet velocity no-slip and no-penetration boundary condition was prescribed. This gave the following set of boundary conditions at the liquid-vapour interface.

$$\rho_{acetone} = 6.7381 \times 10^{-4}\,\mathrm{g\,cm^{-3}} \qquad \text{on } x \in [0, 2.54],\ y = 0 \tag{3.17}$$

$$\rho_{methanol} = 6.1530 \times 10^{-4}\,\mathrm{g\,cm^{-3}} \qquad \text{on } x \in [0, 2.54],\ y = 0 \tag{3.18}$$

$$v_{x,air} = v_{y,air} = 0\,\mathrm{cm\,s^{-1}} \qquad \text{on } x \in [0, 2.54],\ y = 0 \tag{3.19}$$

As mentioned previously by Mills and Chang [79], a diffusion slip boundary condition is required along the wall of the tube. However, OpenFCST does not currently have the ability to apply a diffusion slip boundary condition. Mills and Chang, also mention that when a no-slip boundary condition is used 2D flow features do not significantly effect the radial concentration [79]. As a result, a no-slip and no-penetration Dirichlet velocity boundary conditions was prescribed along the Stefan tube wall for all gas species. This is not expected to significantly effect the concentration along the Stefan tube, but will most likely effect the velocity distributions. For this reason, only the concentration along the center of the Stefan tube was considered in the analysis. The no-slip and no-penetration boundary conditions are expressed as:

$$\boldsymbol{v}_{acetone} = \boldsymbol{v}_{methanol} = \boldsymbol{v}_{air} = 0\,\mathrm{cm\,s^{-1}} \qquad \text{on } x = 2.54,\ y \in [0, 23.8] \tag{3.20}$$

The final side is the center of the Stefan tube so a symmetry boundary condition was applied

for all gas species. This is expressed as:

$$\left.\frac{\partial v_x}{\partial x}\right|_{acetone} = \left.\frac{\partial v_x}{\partial x}\right|_{methanol} = \left.\frac{\partial v_x}{\partial x}\right|_{air} = 0 \qquad \text{on } x = 0,\ y \in [0, 23.8] \tag{3.21}$$

3.5.3 Gas Properties

Certain properties of each gas are required for calculating the partial viscosities and diffusion coefficients. Table 3.1 displays molar mass, collision diameter, and the molecular energy parameter divided by the Boltzmann constant for these gases implemented in OpenFCST.

Table 3.1 – Gas Properties for Carty and Schrodt Stefan Tube Experiment

Property	Acetone	Methanol	Air	Units	Reference
M	58.078	32.042	28.97	$\mathrm{g\,mol^{-1}}$	[45]
σ	4.6	3.626	3.711	Å	[86]
ε/k	560.2	481.8	78.6	K	[86]

3.5.3.1 Results

Figure 3.14 displays a comparison of Carty and Schrodt's experiment data with the implementation of Kerkhof and Geboers' mass transport equation. The molar fractions for the gas species calculated from the analytical solution of the 1D Maxwell-Stefan equations, provided by Carty and Schrodt [117], are also shown.

Figure 3.14 shows that there is very little difference between the solutions from Maxwell-Stefan and Kerkhof-Geboers. In fact, the maximum molar fraction error, from the Maxwell-Stefan analytical solution, is 0.007 (1.6%). This validates that the new model was implemented correctly to account for multi-species mass transport.

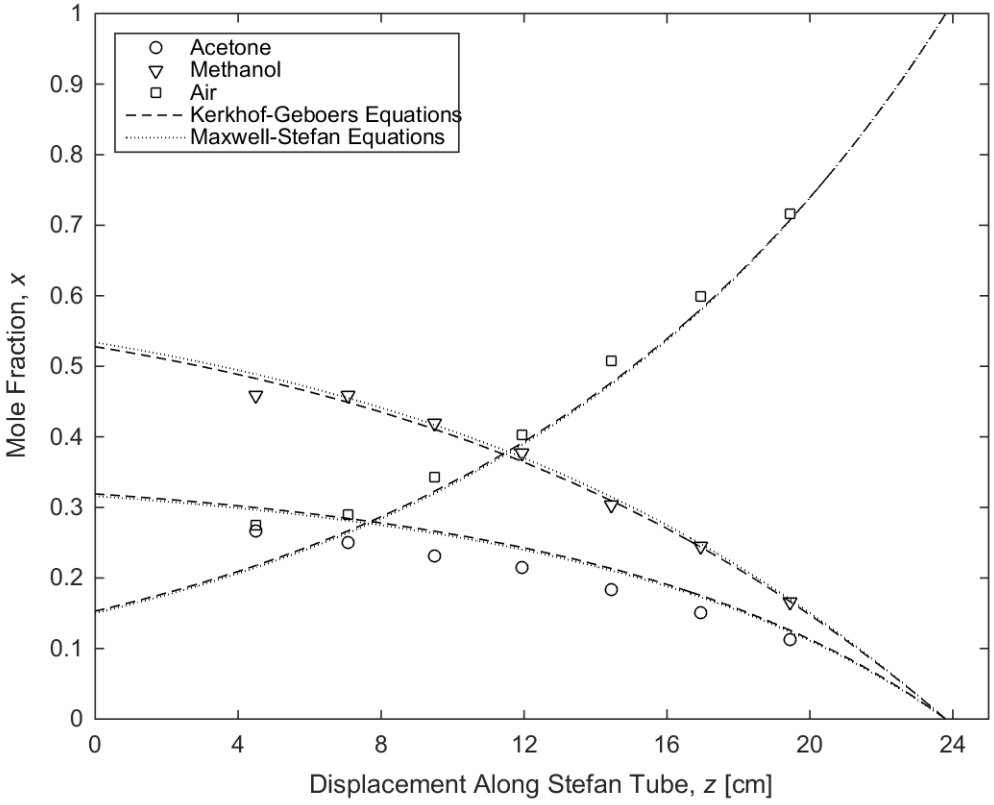

Figure 3.14 – Comparison of Maxwell-Stefan and Kerkhof-Geboers equations for a three species Stefan tube experiment

Chapter 4

Cathode Electrode Model Governing Equations

4.1 Introduction

In the previous chapters Kerkhof and Geboers' multi-component equations were volume averaged, linearized, and the weak formulations were derived. The implemented equations in OpenFCST were then validated against benchmark tests. In this chapter, the equations are coupled to electrochemical reaction kinetics so they can be used in fuel cell simulations. This was done by the addition of sink/source terms to the continuity equations of the gas species to account for electro-chemical reactions. Electron conducting and electrolyte potentials control the rate of the reaction. Therefore, electrolyte and electron transport equations are also implemented.

4.2 Cathode Model

4.2.1 Governing Equations

The ORR occurring in the cathode CL is:

$$\frac{1}{2}O_2 + 2H^+ + 2e^- \rightleftharpoons H_2O \tag{4.1}$$

This electro-chemical reaction shows that oxygen, protons, and electrons, are consumed while water is formed in the CL. In the previous chapters, electro-chemical reactions were not considered. To resolve this a source/sink term must be applied to the continuity equations for each species as follows:

$$\nabla \cdot \boldsymbol{F}_{mass_\alpha} = S_\alpha \tag{4.2}$$

where S_α is a source/sink term for species α. For the case of a cathode PEFC the source/sink terms for each species are:

$$S_{O_2} = \begin{cases} -\frac{M_{O_2}}{4F} J & \text{in } \Omega_{CL} \\ 0 & \text{in } \Omega_c,\ \Omega_{GDL},\ \Omega_{MPL} \end{cases} \tag{4.3}$$

$$S_{H_2O} = \begin{cases} \frac{M_{H_2O}}{2F} J & \text{in } \Omega_{CL} \\ 0 & \text{in } \Omega_c,\ \Omega_{GDL},\ \Omega_{MPL} \end{cases} \tag{4.4}$$

$$S_{N_2} = 0 \tag{4.5}$$

where F is Faraday's constant ($96\,485\,\mathrm{C\,mol^{-1}}$), and J is the volumetric current density ($\mathrm{A\,cm^{-3}}$). The volumetric current density is a function of the oxygen concentration, membrane electrical potential, ϕ_m, and solid electrical potential, ϕ_s.

Although the source/sink terms are now defined for the production/consumption of water and oxygen there are two new unknowns, i.e. ϕ_m and ϕ_s. Transport equations are required for these two new species, i.e. protons and electrons. As derived by Secanell [18], the protonic and electronic transport equations are expressed respectively as:

$$\nabla \cdot (\sigma_m^{eff} \nabla \phi_m) = -\frac{J_m}{F} = \frac{J}{F} \tag{4.6}$$

$$\nabla \cdot (\sigma_s^{eff} \nabla \phi_s) = -\frac{J}{F} \tag{4.7}$$

where σ_m^{eff} and σ_s^{eff} are the effective protonic and electronic conductivity respectively, and J_m is the volumetric current density in the electrolyte phase.

4.2.2 Closure Equations

4.2.2.1 Kinetic Model

The ORR is a complex reaction with many elementary reaction steps that researchers are continuously trying to understand better. Wang et al. proposed the double trap kinetic model to more accurately account for this reaction [120]. Moore extended the model such that oxygen depletion and backwards reactions were better accounted for [20]. A more detailed description of this model can be found in [21].

The micro-scale structure of the CL is modeled assuming an ionomer covered catalyst particle (ICCP) structure. Figure 4.1 displays a diagram of the ICCP model. For the ICCP model it is assumed that:

1. The local CL microstructure is idealized by a single spherical carbon particle covered uniformly with platinum and is surrounded by a thin ionomer film, and

2. The oxygen is assumed to first dissolve into the ionomer film, then diffuse through the film, and finally react at the surface of the carbon particle where the platinum is located.

A more detailed description of this model can be found in [25, 121].

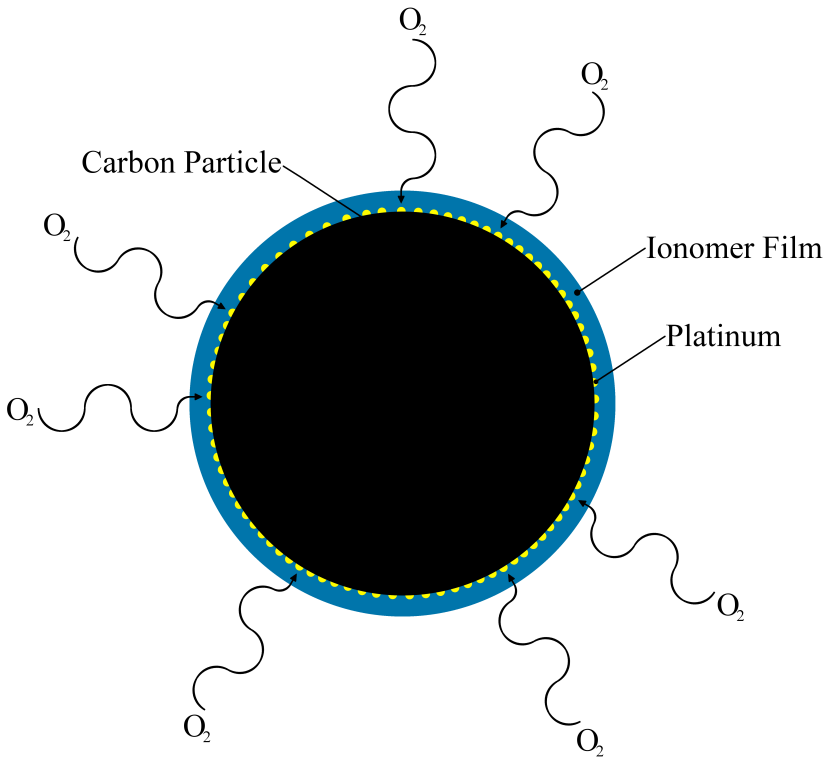

Figure 4.1 – Carbon-platinum structure in the ICCP model

4.2.2.2 Effective Transport Properties

In section 2.4.3.2, the effect of a porous domain on the diffusion coefficients was discussed. Similarly, the other transport properties must also account for the differences in a porous domain through the porosity and tortuosity. Like the diffusion coefficient, this was done using percolation theory, i.e. equation (2.85) but applied to other properties instead of $\mathscr{D}_{\alpha\beta}$.

4.2.2.3 Viscosity Model

The partial viscosity model used was Wilke's model. This is because the partial viscosity of the gases in the cathode can be modeled fairly accurately with Wilke's model as discussed in section 2.4.3.3.1. As well, the simulations are already computationally expensive with three gas species and the use of the ICCP micro-scale model.

4.2.3 Linearization

The linearization is straightforward, and is performed in a similar fashion as shown in section 2.5.2. The only difference is that an additional source/sink term is included. The final results for the linearization of the transport equations are expressed as:

$$\nabla \cdot \delta \boldsymbol{F}_{mass_\alpha} - \zeta_\alpha \delta J = -\nabla \cdot \boldsymbol{F}^n_{mass_\alpha} + \zeta_\alpha J \tag{4.8}$$

$$\nabla \cdot (\sigma_m^{eff} \nabla \delta\phi_m) - \frac{1}{F}\delta J = -\nabla \cdot (\sigma_m^{eff} \nabla \phi_m) + \frac{1}{F} J \tag{4.9}$$

$$\nabla \cdot (\sigma_s^{eff} \nabla \delta\phi_s) + \frac{1}{F}\delta J = -\nabla \cdot (\sigma_s^{eff} \nabla \phi_s) - \frac{1}{F} J \tag{4.10}$$

$$\delta J = \frac{\partial J}{\partial \phi_m}\delta\phi_m + \frac{\partial J}{\partial \phi_s}\delta\phi_s + \frac{\partial J}{\partial \rho_{O_2}}\delta\rho_{O_2} \tag{4.11}$$

$$\zeta_\alpha = \begin{cases} -\frac{M_{O_2}}{4F} & \text{if } \alpha = O_2 \\ \frac{M_{H_2O}}{2F} & \text{if } \alpha = H_2O \\ 0 & \text{if } \alpha = N_2 \end{cases} \tag{4.12}$$

where equation (4.8) is the linearized form that describes the transport of the individual gas species, and equation (4.10) is the linearized form that describes the transport of the the electrons and protons.

4.2.4 Weak Formulation

The weak formulation for the mass transport of the individual species is done the same as in section 2.6. The only difference is that there is now a source term included. Typically, the process used in weakening a PDE in FEA is by transfering the derivatives from the solution variable to the test function. This is typically done by using equation (2.148) and the divergence theorem. Due to the fact that there is no derivatives on this source term there is no need to do any of this to the source term. As a result, the derivation of the weak formulations is done the same as in section 2.6 with the extra source term. As well, using the same rational as in section 2.7.1, first order Lagrangian shape functions were used for the membrane and solid electrical potential. In summary, the final set of weak formulations used to solve this multi-component multi-physics problem are expressed as:

$$\begin{aligned} -\int_{\Omega^e} \delta \boldsymbol{F}_{mass_\alpha} \cdot \nabla \Psi^q_\alpha + \zeta_\alpha \Psi^q_\alpha \delta J \, \mathrm{d}\Omega^e + \oint_{\Gamma^e} \Psi^q_\alpha \delta \boldsymbol{F}_{mass_\alpha} \cdot \boldsymbol{n} \, \mathrm{d}\Gamma^e \\ = \int_{\Omega^e} \boldsymbol{F}^n_{mass_\alpha} \cdot \nabla \Psi^q_\alpha + \zeta_\alpha \Psi^q_\alpha J^n \, \mathrm{d}\Omega^e - \oint_{\Gamma^e} \Psi^q_\alpha \boldsymbol{F}^n_{mass_\alpha} \cdot \boldsymbol{n} \, \mathrm{d}\Gamma^e \end{aligned} \tag{4.13}$$

$$
\begin{aligned}
-\int_{\Omega^e} \sigma_m^{eff} \nabla \delta\psi_m \cdot \nabla \Psi_m^q + \frac{1}{F}\Psi_m^q \delta J \,\mathrm{d}\Omega^e + \oint_{\Gamma^e} \sigma_m^{eff} \Psi_m^q \nabla \delta\psi_m \cdot \boldsymbol{n} \,\mathrm{d}\Gamma^e = \\
\int_{\Omega^e} \sigma_m^{eff} \nabla \phi_m^n \cdot \nabla \Psi_m^q + \frac{1}{F}\Psi_m^q J^n \,\mathrm{d}\Omega^e - \oint_{\Gamma^e} \sigma_m^{eff} \Psi_m^q \nabla \phi_m^n \cdot \boldsymbol{n} \,\mathrm{d}\Gamma^e
\end{aligned} \tag{4.14}
$$

$$
\begin{aligned}
-\int_{\Omega^e} \sigma_s^{eff} \nabla \delta\psi_s \cdot \nabla \Psi_s^q - \frac{1}{F}\Psi_s^q \delta J \,\mathrm{d}\Omega^e + \oint_{\Gamma^e} \sigma_s^{eff} \Psi_s^q \nabla \delta\psi_s \cdot \boldsymbol{n} \,\mathrm{d}\Gamma^e = \\
\int_{\Omega^e} \sigma_s^{eff} \nabla \phi_s^n \cdot \nabla \Psi_s^q - \frac{1}{F}\Psi_s^q J^n \,\mathrm{d}\Omega^e - \oint_{\Gamma^e} \sigma_s^{eff} \Psi_s^q \nabla \phi_s^n \cdot \boldsymbol{n} \,\mathrm{d}\Gamma^e
\end{aligned} \tag{4.15}
$$

$$
\begin{aligned}
-\int_{\Omega^e} \nabla \boldsymbol{\Psi}_\alpha^w : \left(\delta \hat{\boldsymbol{F}}_{mom_\alpha} + \delta P_\alpha \hat{\mathbf{I}} - \delta \hat{\boldsymbol{\tau}}_\alpha\right) + \boldsymbol{\Psi}_\alpha^w \cdot \left(\delta \boldsymbol{F}_{por_\alpha} + \delta\psi_\alpha^\rho \boldsymbol{g} + \delta \boldsymbol{D}_\alpha\right) \mathrm{d}\Omega^e \\
+ \oint_{\Gamma^e} \left(\delta \hat{\boldsymbol{F}}_{mom_\alpha} + \delta P_\alpha \hat{\mathbf{I}} - \delta \hat{\boldsymbol{\tau}}_\alpha\right) \boldsymbol{\Psi}_\alpha^w \cdot \boldsymbol{n} \,\mathrm{d}\Gamma^e \\
= \int_{\Omega^e} \nabla \boldsymbol{\Psi}_\alpha^w : \left(\hat{\boldsymbol{F}}_{mom_\alpha}^n + P_\alpha^n \hat{\mathbf{I}} - \hat{\boldsymbol{\tau}}_\alpha^n\right) + \boldsymbol{\Psi}_\alpha^w \cdot \left(\boldsymbol{F}_{por_\alpha}^n + \psi_\alpha^\rho \boldsymbol{g} + \boldsymbol{D}_\alpha^n\right) \mathrm{d}\Omega^e \\
- \oint_{\Gamma^e} \left(\hat{\boldsymbol{F}}_{mom_\alpha}^n + P_\alpha^n \hat{\mathbf{I}} - \hat{\boldsymbol{\tau}}_\alpha^n\right) \boldsymbol{\Psi}_\alpha^w \cdot \boldsymbol{n} \,\mathrm{d}\Gamma^e
\end{aligned} \tag{4.16}
$$

$$
\delta \boldsymbol{F}_{mass_\alpha} = \delta\psi_\alpha^\rho \boldsymbol{v}_\alpha^n + \rho_\alpha^n \delta \boldsymbol{\psi}_\alpha^v \tag{4.17}
$$

$$
\boldsymbol{F}_{mass_\alpha} = \rho_\alpha^n \boldsymbol{v}_\alpha^n \tag{4.18}
$$

$$
\delta J = \frac{\partial J}{\partial \phi_m}\delta\phi_m + \frac{\partial J}{\partial \phi_s}\delta\phi_s + \frac{\partial J}{\partial \rho_{O_2}}\delta\rho_{O_2} \tag{4.19}
$$

$$
\delta \hat{\boldsymbol{F}}_{mom_\alpha} = \delta\psi_\alpha^\rho \boldsymbol{v}_\alpha^n \otimes \boldsymbol{v}_\alpha^n + \rho_\alpha^n \delta\boldsymbol{\psi}_\alpha^v \otimes \boldsymbol{v}_\alpha^n + \rho_\alpha^n \boldsymbol{v}_\alpha^n \otimes \delta\boldsymbol{\psi}_\alpha^v \tag{4.20}
$$

$$
\hat{\boldsymbol{F}}_{mom_\alpha} = \rho_\alpha^n \boldsymbol{v}_\alpha^n \otimes \boldsymbol{v}_\alpha^n \tag{4.21}
$$

$$
\delta P_\alpha = \delta\psi_\alpha^\rho \frac{R T_{mix}}{M_\alpha} \tag{4.22}
$$

$$
P_\alpha = \rho_\alpha^n \frac{R T_{mix}}{M_\alpha} \tag{4.23}
$$

$$
\delta \hat{\boldsymbol{\tau}}_\alpha = \delta\eta_\alpha \left(2\nabla_s \boldsymbol{v}_\alpha^n - \frac{2}{3}(\nabla \cdot \boldsymbol{v}_\alpha^n)\hat{\mathbf{I}}\right) + \eta_\alpha \left(2\nabla_s \delta\boldsymbol{\psi}_\alpha^v - \frac{2}{3}(\nabla \cdot \delta\boldsymbol{\psi}_\alpha^v)\hat{\mathbf{I}}\right) \tag{4.24}
$$

$$
\hat{\boldsymbol{\tau}}_\alpha = 2\eta_\alpha \nabla_s \boldsymbol{v}_\alpha^n - \frac{2}{3}\eta_\alpha \nabla \cdot \boldsymbol{v}_\alpha^n \hat{\mathbf{I}} \tag{4.25}
$$

$$
\delta \boldsymbol{F}_{por_\alpha} = \begin{cases}
0 & \text{in } \Omega_c \\
-\hat{\mathbf{K}}^{-1} \varepsilon \left(\boldsymbol{v}_\alpha^n \delta\eta_\alpha + \eta_\alpha \delta\boldsymbol{\psi}_\alpha^v\right) & \\
\quad - \hat{\boldsymbol{\beta}} \left(\delta\psi_\alpha^\rho |\varepsilon \boldsymbol{v}_\alpha^n| \varepsilon \boldsymbol{v}_\alpha^n + \rho_\alpha^n \dfrac{\varepsilon \boldsymbol{v}_\alpha^n \varepsilon \delta\boldsymbol{\psi}_\alpha^v}{|\varepsilon \boldsymbol{v}_\alpha^n|} \varepsilon \boldsymbol{v}_\alpha^n \right. & \text{in } \Omega_p \\
\quad \left. + \rho_\alpha^n |\varepsilon \boldsymbol{v}_\alpha^n| \varepsilon \delta\boldsymbol{\psi}_\alpha^v \right) &
\end{cases} \tag{4.26}
$$

$$
\boldsymbol{F}_{por_\alpha} = \begin{cases}
0 & \text{in } \Omega_c \\
-\eta_\alpha \hat{\mathbf{K}}^{-1} \varepsilon \boldsymbol{v}_\alpha^n - \hat{\boldsymbol{\beta}} \rho_\alpha^n |\varepsilon \boldsymbol{v}_\alpha^n| \varepsilon \boldsymbol{v}_\alpha^n & \text{in } \Omega_p
\end{cases} \tag{4.27}
$$

$$\delta \boldsymbol{D}_\alpha = \sum_{\beta=1}^{N} (\delta P_\alpha P_\beta + P_\alpha \delta P_\beta) \hat{\boldsymbol{D}}_{\alpha\beta} (\boldsymbol{v}_\beta^n - \boldsymbol{v}_\alpha^n) + P_\alpha P_\beta \hat{\boldsymbol{D}}_{\alpha\beta} (\delta \boldsymbol{\psi}_\beta^v - \delta \boldsymbol{\psi}_\alpha^v) \tag{4.28}$$

$$\boldsymbol{D}_\alpha = \sum_{\beta=1}^{N} P_\alpha P_\beta \hat{\boldsymbol{D}}_{\alpha\beta} (\boldsymbol{v}_\beta^n - \boldsymbol{v}_\alpha^n) \tag{4.29}$$

$$\hat{\boldsymbol{D}}_{\alpha\beta} = \left(P_t \mathscr{D}_{\alpha\beta}^{eff} \right)^{-1} \hat{\mathbf{I}} \tag{4.30}$$

$$\varepsilon = \begin{cases} 1 & \text{in } \Omega_c \\ 0 < \varepsilon \leq 1 & \text{in } \Omega_p \end{cases} \tag{4.31}$$

$$\Psi_\alpha^q = \psi_{\alpha,i}^\rho \tag{4.32}$$

$$\Psi_m^q = \psi_{m,i} \tag{4.33}$$

$$\Psi_s^q = \psi_{s,i} \tag{4.34}$$

$$\delta \psi_\alpha^\rho = \sum_{j=1}^{N} \delta \rho_{\alpha,j} \psi_{\alpha,j}^\rho \tag{4.35}$$

$$\delta \psi_m = \sum_{j=1}^{N} \delta \phi_{m,j} \psi_{m,j} \tag{4.36}$$

$$\delta \psi_s = \sum_{j=1}^{N} \delta \phi_{s,j} \psi_{s,j} \tag{4.37}$$

$$\delta \boldsymbol{\psi}_{\alpha,v} = \begin{bmatrix} \sum_{l=1}^{N} \delta v_{\alpha,l}^x \psi_{\alpha,l}^{v_x} \\ \sum_{r=1}^{N} \delta v_{\alpha,r}^y \psi_{\alpha,r}^{v_y} \end{bmatrix} \tag{4.38}$$

$$\boldsymbol{\Psi}_\alpha^w = \begin{bmatrix} \psi_{\alpha,k}^{v_x} \\ \psi_{\alpha,p}^{v_y} \end{bmatrix} \tag{4.39}$$

4.3 Base Parameters

Tables 4.1 and 4.2 display the properties for the GDL and MPL used in the simulations respectively. It is difficult to measure properties for the MPL separate from the GDL. In the following simulations through-plane permeability data reported by Lalit et al. [122] was used. In their study, SGL 34 BA (only GDL) and SGL 34 BC (GDL+MPL included) were investigated. The SGL 34 BA was used to determine the properties of the GDL alone. Using these values for the GDL and assuming constant velocity through the porous medium they estimated the properties of the MPL in the SGL 34 BC. The values used in this work were taken by averaging the results from the two samples reported by Lalit et al. Lalit et al. only considered the through-plane permeability, so for in-plane permeability data, values reported by Mangal [115] for an SGL 34 BA were used. The permeability values shown in Tables 4.1

Table 4.1 – Composition and transport properties of the GDL

Parameter	Variable	Value
Gas diffusion layer type		DesignFibrousGDL
Generic data		
Porosity	ε	0.83 [122]
Permeability_XX (cm^2)	K_{XX}	2.1746×10^{-7} [122]
Permeability_YY (cm^2)	K_{YY}	1.7098×10^{-7} [115]
Composition		
Anisotropic transport		true
Method effective transport properties in pores		Percolation
Method effective transport properties in solid phase		Percolation
Gas transport properties		
Porosity threshold X	$\varepsilon_{th,X}$	0.118 [132]
Porosity threshold Y	$\varepsilon_{th,Y}$	0.118 [132]
Porosity network constant X	μ_X	0.785 [97, 133]
Porosity network constant Y	μ_Y	0.521 [97, 133]
Electron transport properties		
Electrical conductivity X ($S\,cm^{-1}$)	$\sigma_{s,X}$	16.03 [132]
Electrical conductivity Y ($S\,cm^{-1}$)	$\sigma_{s,Y}$	272.78 [132]
Solid network threshold X	$\varepsilon_{th,X}$	0.0 [11, 22]
Solid network threshold Y	$\varepsilon_{th,Y}$	0.0 [11, 22]
Solid network constant X	μ_X	1.5 [11, 22]
Solid network constant Y	μ_Y	1.0 [11, 22]

and 4.2 have been corrected for volume averaging as shown in section 3.4.1.

Table 4.3 and 4.4 display the properties for the CL used in the simulations. A thickness of 10 µm for the CL was chosen as this is similar in magnitude to other papers in literature [26, 34, 123–128]. There are not many reported values for the permeability of the CL. Ismail et al. [129], Kim et al. [130], and Sui et al. [131] used a value of $1.0 \times 10^{-9}\,cm^2$. This value seems questionable considering that Kim et al. and Sui et al. used the same permeability for the GDL, and Ismail et al. used a through-plane GDL permeability of the same order of magnitude. Eikerling predicted a range for the absolute permeability of the CL between approximately 0.375×10^{-14} and $2 \times 10^{-14}\,cm^2$. Due to the range of values used in papers depending on the source, the CL permeability was varied and compared to see the effect of this value on results.

Table 4.2 – Composition and transport properties of the MPL

Parameter	Variable	Value
Micro porous layer type		DesignMPL
Generic data		
Porosity	ε	0.4 [132]
Permeability_XX (cm^2)	K_{XX}	5.4×10^{-10} [122]
Permeability_YY (cm^2)	K_{YY}	5.4×10^{-10} [122]
Composition		
Anisotropic transport		false
Method effective transport properties in pores		Percolation
Method effective transport properties in solid phase		Percolation
Gas transport properties		
Porosity threshold	ε_{th}	0.118 [132]
Porosity network constant	μ	2 [134]
Electron transport properties		
Electrical conductivity ($S\,cm^{-1}$)	σ_s	88.84 [132]
Solid network threshold	ε_{th}	0.118 [132]
Solid network constant	μ	2.0 [134]

Table 4.3 – Composition and transport properties of the CL

Parameter	Variable	Value
Catalyst layer type		MultiScaleCL
Catalyst type		Platinum
Catalyst support type		CarbonBlack
Electrolyte type		Nafion
Kinetics type		DoubleTrapKinetics
MultiScaleCL		
Microscale type		ICCP
Radius (nm)		50 [121]
Film Thickness (nm)		5.0 [121]
Use non equilibrium BC		true
Non Equilibrium BC Rate constant		0.001 [121]
Composition		
Method effective transport properties in pores		Percolation
Method effective transport properties in solid phase		Percolation
Method effective transport properties in electrolyte phase		Iden11
Platinum loading on support (%wt)		46 [132]
Platinum loading per unit volume ($\mathrm{mg\,cm^{-3}}$)		400 [22]
Electrolyte loading (%wt)		30 [132]
Method to compute active area		given
Active area ($\mathrm{cm^2\,cm^{-3}}$)		2.0×10^5 [26, 132]
Gas transport properties		
Porosity threshold	ε_{th}	0.259 [11]
Porosity network constant	μ	2.0 [11]
Electron transport properties		
Solid network threshold	ε_{th}	0.118 [11, 22]
Solid network constant	μ	2.0 [11, 22]

Table 4.4 – Bulk properties of CL materials

Parameter	Variable	Value
Nafion®		
Method to compute proton conductivity		Iden11
Henry's Law Constant for Oxygen ($Pa\,cm^3\,mol^{-1}$)		3.1664×10^{10} [123, 135]
Henry's Law Constant for Hydrogen ($Pa\,cm^3\,mol^{-1}$)		6.94×10^{10} [135]
CarbonBlack		
Density ($g\,cm^{-3}$)		1.69 [136]
Electrical conductivity ($S\,cm^{-1}$)		88.84 [132]
Platinum		
Method for kinetics parameters (ORR)		Double_trap
Density ($g\,cm^{-3}$)		21.5 [137]

4.4 Through the Channel Cathode Model

OpenFCST already has a Cathode model implemented that uses a Fickian transport model. Results from this model are compared to the new CathodeKG model. The two models are as objectively compared as possible by prescribing the same boundary conditions and using the same base parameters. The differences are:

1. The Cathode model assumes isobaric conditions, as a result it does not account for pressure drops due to the permeability of the porous layers,
2. The Cathode model assumes an infinitely dilute solution, so only the diffusion coefficient of Oxygen-Nitrogen is required for the transport of oxygen,
3. The Cathode model only accounts for oxygen transport and using Fick's law, therefore it solves for the molar fraction of oxygen for determining transport.

The two models are first compared at an oxygen molar fraction of 1% (before humidification) at the inlet. This was done to validate the CathodeKG model. At this concentration the infinitely dilute solution assumption should be valid, and the two models should coincide with one another. At this oxygen concentration, the CL permeability was also varied to see the effects. Next, the inlet oxygen concentration is varied to determine the validity of the infinitely dilute solution at typical inlet oxygen concentrations is studied. Next, the change in density is analyzed. Finally, the flow profile of each of the individual gas species is discussed.

4.4.1 Domain

Figure 4.2 displays a schematic of the domain considered. Colours are used to show the different materials, the GDL is blue, MPL is gray, and the CL is red. Symmetry boundary conditions were applied such that only half of the channel and bipolar plate were considered. The width of the channel and bipolar plate are based on the dimensions of the bipolar plate used in the ESDL, which is $0.031''$ (0.079 cm). The initial mesh used can be seen in Figure 4.3. The MPL and CL are composed of eight and ten cells each along the x-direction respectively.

4.4.2 Boundary Conditions

4.4.2.1 CathodeKG Model

A Dirichlet density boundary condition for each species was prescribed at the inlet. The protons and electrons are unable to pass into the gas channel, so a no flux boundary condition

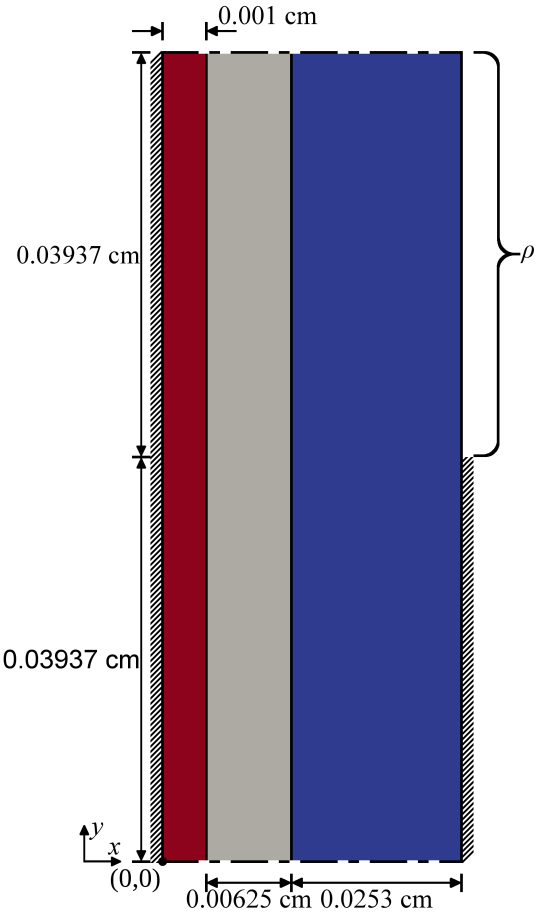

Figure 4.2 – Through-channel PEFC cathode domain (not to scale)

is prescribed for these species. This is expressed mathematically as follows:

$$\rho^0_{O_2},\, \rho^0_{N_2},\, \rho^0_{H_2O} \qquad \text{on } x = 0.0326,\, y \in [0.0395, 0.079] \tag{4.40}$$

$$\boldsymbol{N}_{H^+} \cdot \boldsymbol{n} = \boldsymbol{N}_{e^-} \cdot \boldsymbol{n} = 0 \qquad \text{on } x = 0.0326,\, y \in [0.0395, 0.079] \tag{4.41}$$

where $\boldsymbol{N}_{H^+}$ and $\boldsymbol{N}_{e^-}$ are the flux of the protons and electrons respectively. The densities of the individual species are calculated from ideal gas law in OpenFCST using the `Operating Conditions` class at 101 325 Pa, 353.15 K, 50% relative humidity (RH), and an initial oxygen mole fraction (prior to humidification) of 0.01, 0.10, and 0.21.

A symmetric boundary condition, for each species, was prescribed along the upper and lower boundary. The boundary condition can be represented mathematically as,

$$\boldsymbol{N}_{H^+} \cdot \boldsymbol{n} = \boldsymbol{N}_{e^-} \cdot \boldsymbol{n} = 0 \qquad \text{on } x \in [0, 0.0326],\, y = 0 \text{ and } 0.079 \tag{4.42}$$

$$\oint_\Gamma (\hat{\boldsymbol{F}}_{mom,\alpha} + P_\alpha \hat{\mathbf{I}} - \hat{\boldsymbol{\tau}}_\alpha)\boldsymbol{w}_\alpha \cdot \boldsymbol{n}\, \mathrm{d}\Gamma = 0 \qquad \text{on } x \in [0, 0.0326],\, y = 0 \text{ and } 0.079 \tag{4.43}$$

For all other boundaries a no-slip and no-penetration boundary conditions was applied,

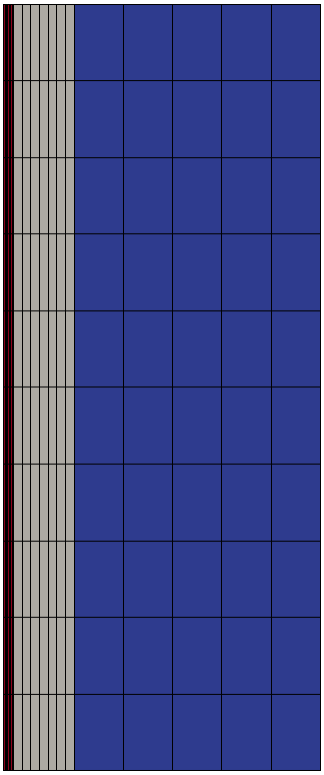

Figure 4.3 – Initial mesh for the through-channel PEFC cathode simulation

i.e:

$$\boldsymbol{v}_{O_2} = \boldsymbol{v}_{N_2} = \boldsymbol{v}_{H_2O} = 0\,\mathrm{cm\,s^{-1}} \tag{4.44}$$

For the protons and electrons Dirichlet boundary conditions are prescribed. Knowing that only protons can pass through the membrane, and electrons pass through the bipolar plate current collector these boundary conditions are prescribed as follows:

$$\phi_m = 0 \qquad \text{on } x = 0,\ y \in [0, 0.079] \tag{4.45}$$

$$\boldsymbol{N}_{e^-} \cdot \boldsymbol{n} = 0 \qquad \text{on } x = 0,\ y \in [0, 0.079] \tag{4.46}$$

$$\boldsymbol{N}_{H^+} \cdot \boldsymbol{n} = 0 \qquad \text{on } x = 0.079,\ y \in [0, 0.0395] \tag{4.47}$$

$$\phi_s^0 \qquad \text{on } x = 0.0326,\ y \in [0, 0.0395] \tag{4.48}$$

$$\boldsymbol{N}_{e^-} \cdot \boldsymbol{n} = 0 \qquad \text{on } x = 0,\ y \in [0.0395, 0.079] \tag{4.49}$$

where ϕ_0 is the voltage (V) applied.

4.4.2.2 Cathode Model

The same boundary conditions for the protons and electrons are prescribed in the Cathode model. The difference between the two model's is the gas species boundary conditions.

This is because no momentum equation is used in the Cathode model, resulting in a purely diffusive transport, so a velocity boundary condition is not necessary. Further, the Cathode model uses molar fraction, x, to describe mass transport instead of density. The resulting boundary conditions for oxygen in this model are no flux at impermeable walls and a Dirichlet boundary condition at the inlet. This is expressed mathematically as follows:

$$x_{O_2}^0 \qquad \text{on } x = 0.0326,\ y \in [0.0395, 0.079] \tag{4.50}$$

$$\nabla x_{O_2} \cdot \boldsymbol{n} = 0 \qquad \text{on } x = 0.0326,\ y \in [0, 0.0395] \tag{4.51}$$

$$\nabla x_{O_2} \cdot \boldsymbol{n} = 0 \qquad \text{on } x = 0,\ y \in [0, 0.079] \tag{4.52}$$

Neither water vapour or oxygen is accounted for in the Cathode model, as mentioned previously, because it is assumed that the oxygen is infinitely dilute in the nitrogen. As well, nitrogen is inert in the reaction and is assumed not to pass through the membrane. As a result, at steady-state there would be no diffusion of nitrogen using the Cathode model.

Symmetry boundary conditions are also prescribed along the upper and lower boundary as discussed in the previous section. This is expressed mathematically for the oxygen molar fraction as follows:

$$\nabla x_{O_2} \cdot \boldsymbol{n} = 0 \qquad \text{on } x \in [0, 0.0326],\ y = 0 \text{ and } 0.079 \tag{4.53}$$

4.4.3 Grid Independence and Adaptive Refinement Study

A global grid independence study (GIS) was performed on the Cathode and CathodeKG models to confirm that the mesh is in the grid independent region. The CL, MPL, and GDL were one cell thick and two cells were used in the y-direction. For the GIS an oxygen inlet concentration of 21%, CL permeability of $1.0 \times 10^{-13}\,\mathrm{cm}^2$, and the current density at $0.2\,\mathrm{V}$ was used. This was done because at these conditions the results are in the mass transport region, resulting in the largest gradients across the cathode. For this reason, it is assumed that if the mesh is in the grid independent region for this case it will be in the grid independent region for all cases analyzed.

An adaptive refinement study (ARS) was also performed. This is because adaptive refinement is preferable to use in order to reduce the computational expense of the simulations, as only the cells with the largest error are refined. When the adaptive refinement is set such that 30% of the cells with the largest error are refined, this leads to an approximate doubling of the number of degrees of freedom. The ARS was done under the same conditions as the GIS.

Figures 4.4 and 4.5 display the GIS and ARS for the Cathode and CathodeKG model respectively. The GIS solutions are systematically and asymptotically converging for the

Cathode and CathodeKG simulations. This suggests that the mesh is in the grid independent region. Figure 4.4 shows that adaptive refinement is refining areas that do not significantly effect the current density for a large portion of the ARS, while Figure 4.5 displays that adaptive refinement is beneficial for the CathodeKG model. The initial mesh used, as shown in Figure 4.3, is much more refined and has approximately 20 times more dofs then the mesh used in this GIS and ARS. Based on these results the mesh in Figure 4.3 should be in the grid independent region when running simulations. Based on these observation one level of adaptive refinement was used for the CathodeKG model simulations, while two levels of global refinement were used for the Cathode model simulations. Giving a final mesh with 11 931 and 15 050 dofs for the Cathode and CathodeKG model's respectively.

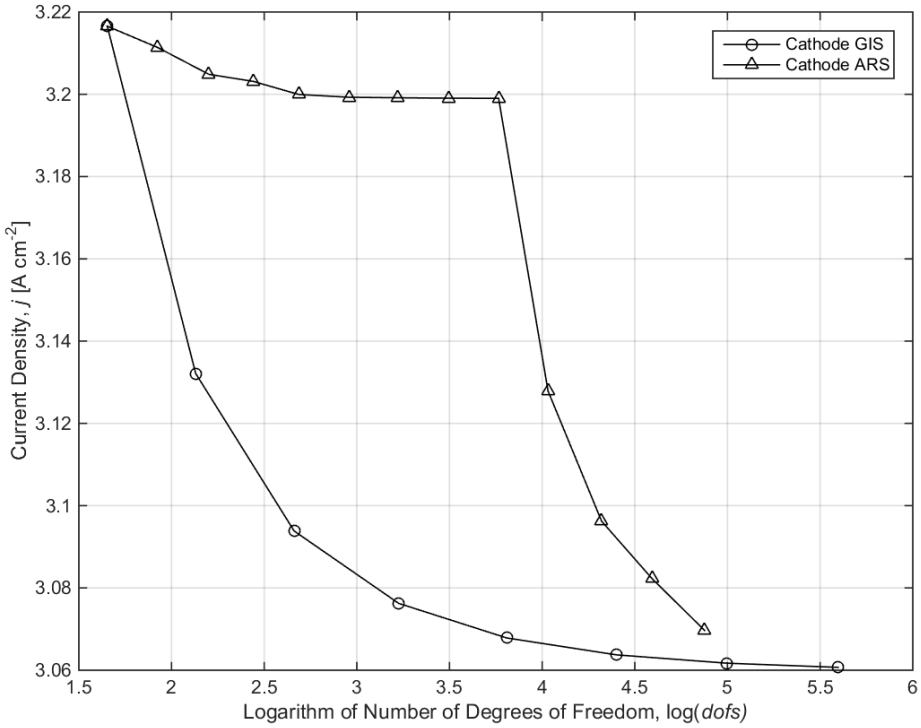

Figure 4.4 – Through-channel global grid independence study (GIS) and adaptive refinement study (ARS) for the Cathode model

4.4.4 Results

As stated in section 4.4.2.1 the inlet is at a temperature and pressure of 353.15 K and 101 325 Pa. As well, the O_2-N_2 mixture is humidified resulting in an RH of 50% before entering the inlet. To properly compare the effects of changing the CL permeability, results were compared when the current density was the same. This is because the current density

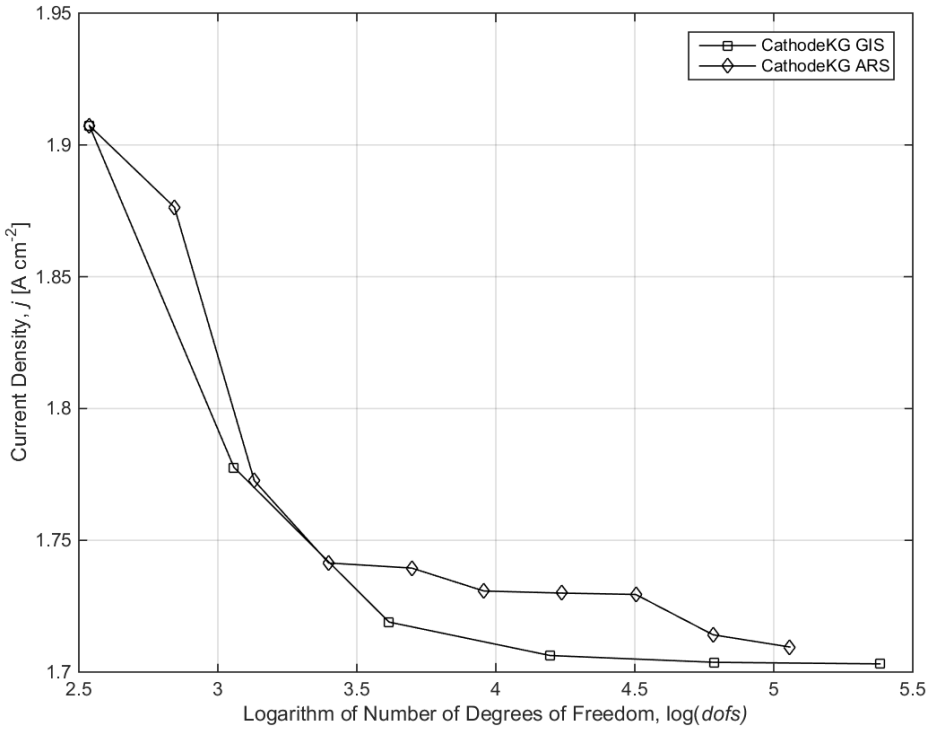

Figure 4.5 – Through-channel global grid independence study (GIS) and adaptive refinement study (ARS) for the CathodeKG model

defines the amount of oxygen consumed and water produced. This results in similar fluxes for each species through the cathode at steady-state. Dr. Shukla has provided polarization curve results that were used in [136] for comparison to the different models. This experimental data was performed under similar conditions with an SGL 24 BC instead of the SGL 34 BC used in the following simulations. The SGL 24 BC and SGL 34 BC have similar properties, but the SGL 34 BC was used in simulations because the properties were more available. Testing protocol and MEA properties for the experimental data can be found in [2]. Input parameters, other than GDL thickness are similar to experiments as discussed in [26].

4.4.4.1 Molar Fraction With 1% Oxygen (Before Humidification) at Inlet

Figure 4.6 displays a polarization curve comparing the two models. For the numerical polarization curves, every fifth point is shown with a marker. This was done so the figure would not become unreadable from having data points every 0.01 V. The Cathode model is able to do the full polarization curve without difficulty, however the CathodeKG model has difficulties at lower permeabilities. This is seen by the $1.0 \times 10^{-14}\,\mathrm{cm}^2$ case where the developed model is unable to determine the current for cell voltages below 0.80 V. A possible reason

for this will be discussed later. The experimental data from Shukla et al. [136] is iR-free and corrected for cross-over because the CathodeKG model does not include PEM ohmic losses and contact resistances.

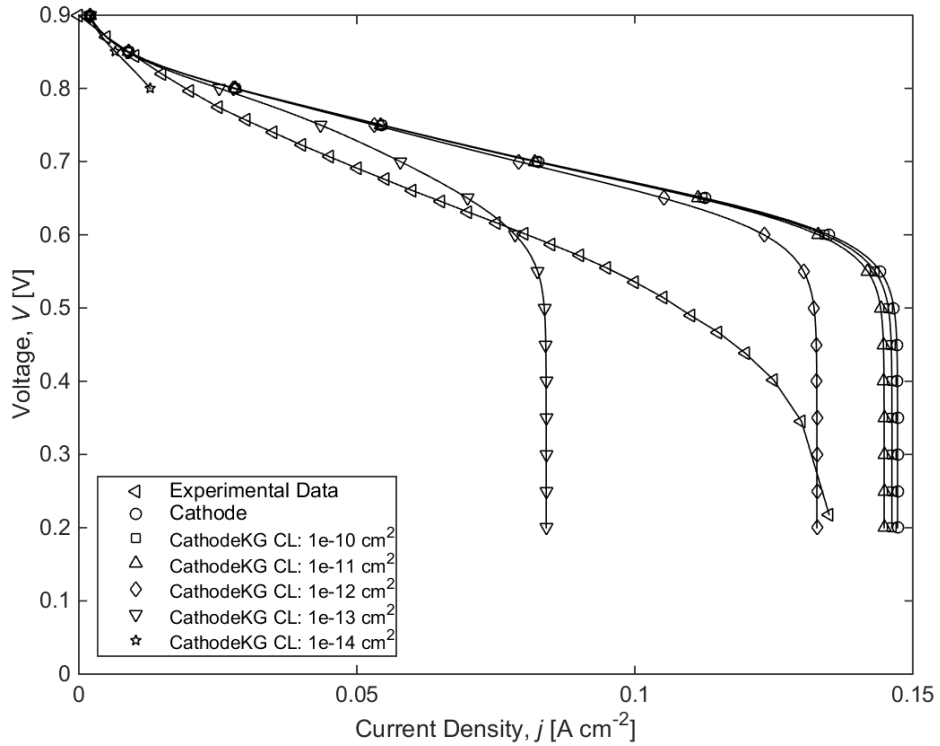

Figure 4.6 – Polarization curves comparing the Cathode model to the CathodeKG model at various CL permeabilities

Figure 4.6 validates the infinitely dilute solution at low oxygen concentration. As one would expect, at low oxygen concentrations the dominant form of transport for the oxygen is diffusion and both the Cathode and CathodeKG models nearly coincide for the entire polarization curve. The small difference between results for permeabilities 1.0×10^{-10} and $1.0 \times 10^{-11}\,\mathrm{cm}^2$ in the CathodeKG model suggest that the model is in the limiting case when Darcy's law is not a significant factor in the transport. As the permeability of the CL decreases the permeability's influence on the performance increases. This is the result of more frictional losses due to the low permeability of the CL accounted for by Darcy's law. The simulation results shown in Figure 4.6 follows a similar trend as the experimental data, but the simulation results differ considerably from experimental data. This is most likely because of unique effects occurring at 1% oxygen, as even at the lowest current densities mass transport effects have a significant effect along the entire channel.

Figure 4.7 displays the oxygen molar fraction on a horizontal line along the middle of

the cathode for different models and permeabilities at a current density of $0.06\,\mathrm{cm}^2$. Using the CathodeKG model with different permeabilities Figure 4.7 displays that the oxygen concentration in the MPL and GDL is independent of the CL permeability. At the same current density, the molar fraction of oxygen in the CL using the CathodeKG model is always lower than the Cathode model. As the CL permeability decreases so does the molar fraction of oxygen in the CL. This is most likely because the Darcy term couples the pressure and velocity to the permeability term. As the permeability decreases the CL becomes more impermeable. This results in slower velocities, thus less oxygen is able to penetrate into the CL. This explains why at a CL permeability of $1.0 \times 10^{-14}\,\mathrm{cm}^2$ the CathodeKG model has difficulty converging to a solution as the CL is becoming more impermeable.

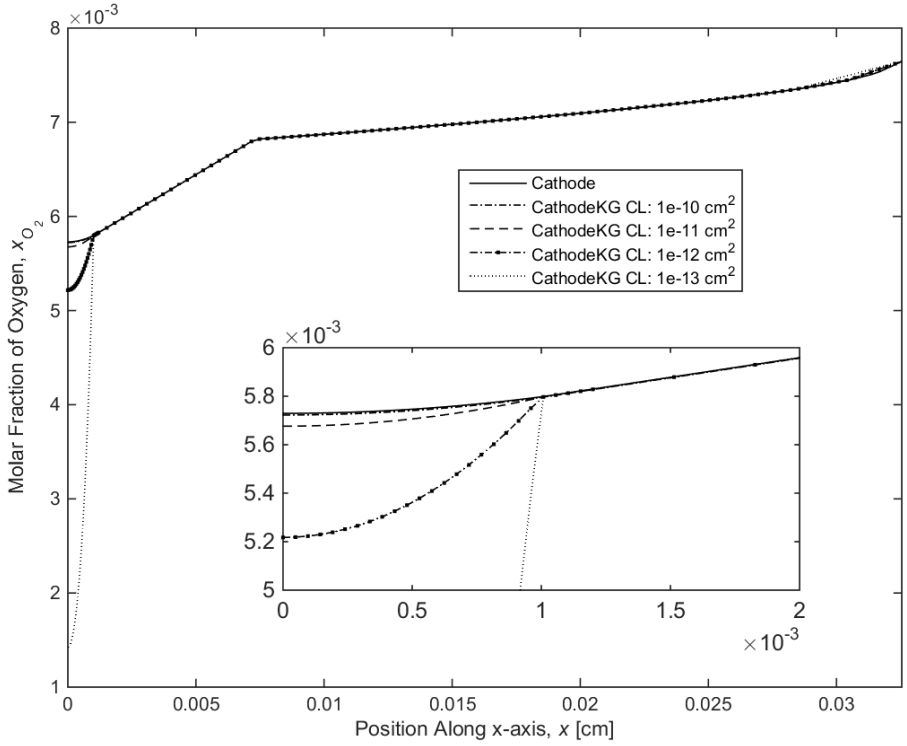

Figure 4.7 – Molar fraction of oxygen at $y = 0.0395\,\mathrm{cm}$ for various permeabilities at $0.06\,\mathrm{A\,cm}^{-2}$

Considering the entire cathode domain, Figures 4.8a) through c) display the oxygen molar fraction through the cathode using the Cathode model. At high cell voltages when little oxygen is required to produce the small currents necessary, there is an abundance of oxygen in the CL. As the current density increases more oxygen is consumed, till the CL is "starved" of oxygen because it is unable to reach the CL fast enough for the reaction to occur. As well, the lowest concentrations of oxygen occur close to the bottom boundary of

the Cathode. This intuitively makes sense as this point is furthest from the channel and is more difficult for oxygen to be transported to this location.

Figure 4.8d) through i) displays the oxygen through the cathode using the CathodeKG model at different permeability values. Similar trends are noticed as in the Cathode model discussed above. Comparing Figure 4.8 a) to d), b) to e) and c) to f) the Cathode and CathodeKG model have almost identical molar fractions throughout the entire cathode. Small differences in scales are due to a lower oxygen molar fraction in the CL of the CathodeKG model as shown earlier in Figure 4.7. Figures 4.8g) through i) also have the same oxygen molar fraction in the CL and GDL, however it is difficult to see due to how much less oxygen is available in the CL at the same current density.

Figure 4.7 showed that the oxygen molar fraction on a horizontal line along the middle of the cathode in the MPL and GDL is independent of the CL permeability when the same current density is considered. Figure 4.9 shows the oxygen, water vapour, and nitrogen molar fraction in the MPL and GDL. These figures show this same trend extends to the entire MPL and GDL for each gas species.

Figure 4.10 shows the molar fraction of each gas species in the CL. The figures are scaled in the x-direction by a factor of 30 to increase the visibility. The molar fraction of oxygen and water vapour do not use the same scale for each CL permeability, because the spans for each figure are so small, that using the same scale will make the others appear to have a constant molar fraction. Oxygen molar fraction displays different distributions throughout the CL depending on the permeability. At high permeabilities, it is more difficult to transport the oxygen to the bottom boundary furthest away from the inlet. At low permeabilities, it is more difficult for the oxygen to be transported into the CL and oxygen reacts at the GDL-CL interface. This results in wasted platinum reaction sites preventing higher current densities. The nitrogen molar fraction shows a similar distribution as the oxygen at different permeabilities. The gradient in nitrogen molar fraction is most likely because it is an inert gas and the nitrogen molecules are being dragged out of the electrode by the water vapour.

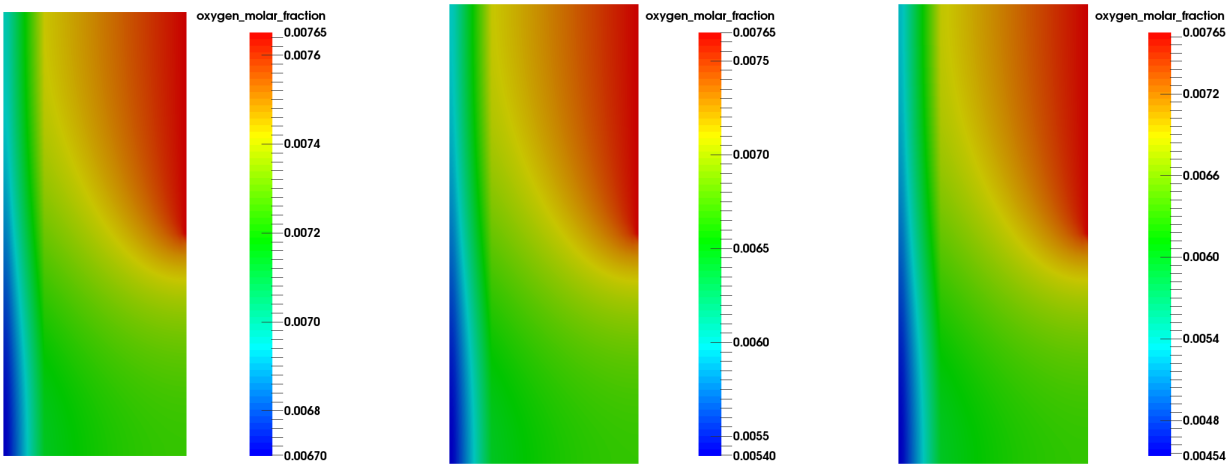

(a) 0.025 A cm^{-2} **(b)** 0.06 A cm^{-2} **(c)** 0.084 A cm^{-2}

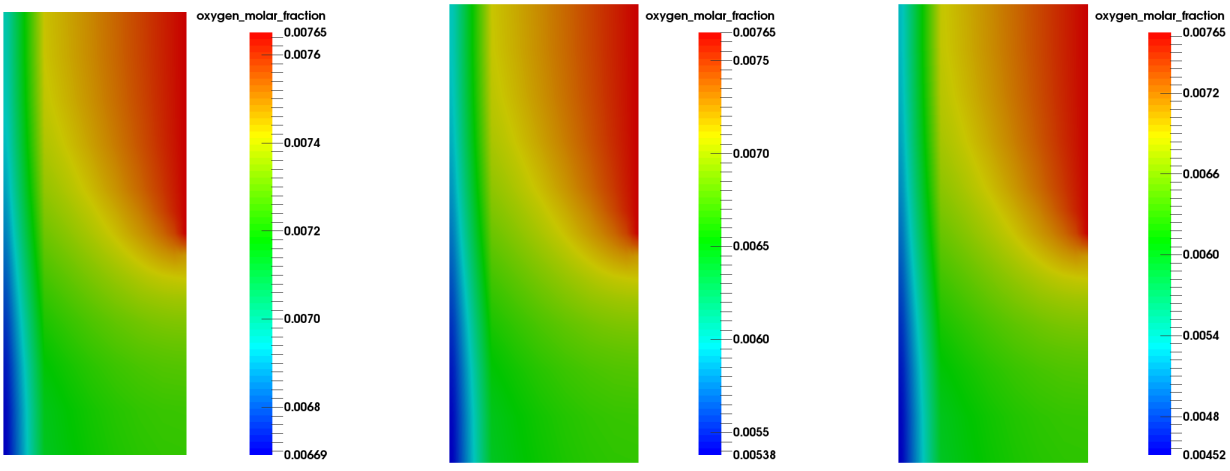

(d) 0.025 A cm^{-2} **(e)** 0.06 A cm^{-2} **(f)** 0.084 A cm^{-2}

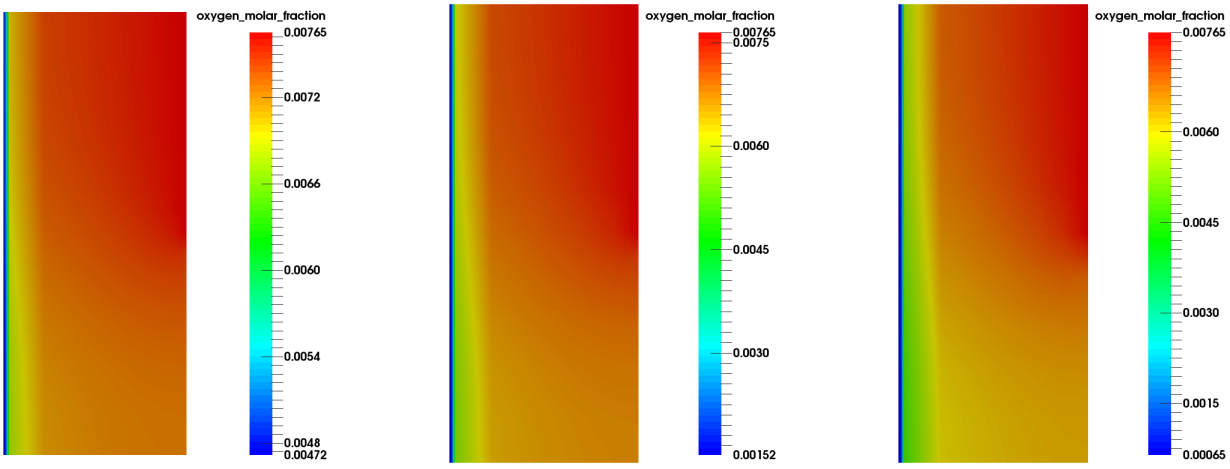

(g) 0.025 A cm^{-2} **(h)** 0.06 A cm^{-2} **(i)** 0.084 A cm^{-2}

Figure 4.8 – Comparison of oxygen molar fraction in cathode at the same currents densities under different parameters: Cathode model (top), CathodeKG model with a CL permeability of 1.0×10^{-10} cm^2 (middle), and CathodeKG model with a CL permeability of 1.0×10^{-13} cm^2 (bottom)

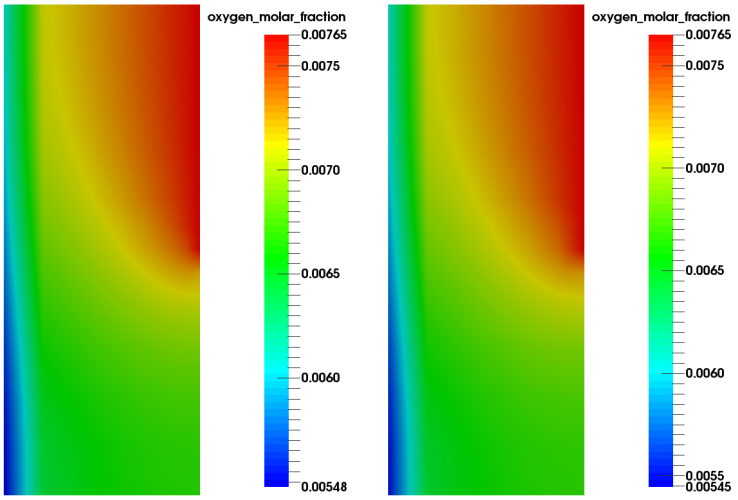

(a) $1.0 \times 10^{-10}\,\mathrm{cm}^2$ **(b)** $1.0 \times 10^{-13}\,\mathrm{cm}^2$

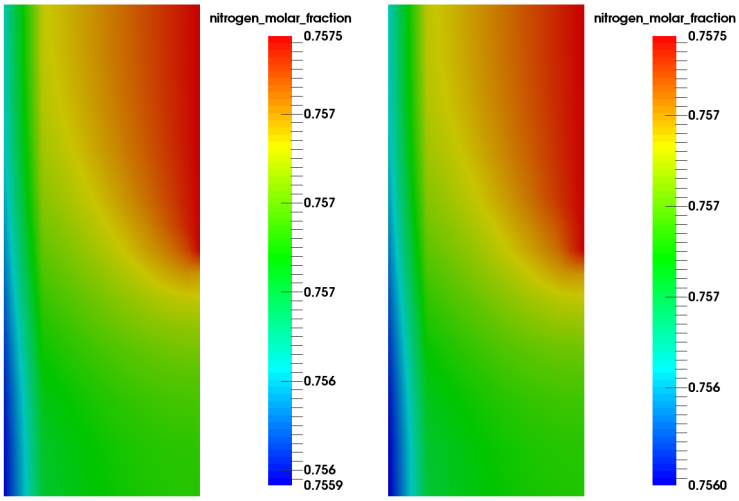

(c) $1.0 \times 10^{-10}\,\mathrm{cm}^2$ **(d)** $1.0 \times 10^{-13}\,\mathrm{cm}^2$

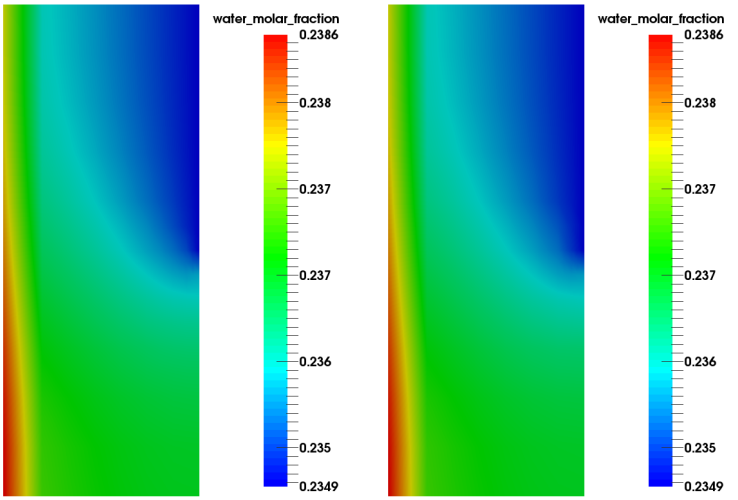

(e) $1.0 \times 10^{-10}\,\mathrm{cm}^2$ **(f)** $1.0 \times 10^{-13}\,\mathrm{cm}^2$

Figure 4.9 – CathodeKG model oxygen (top), nitrogen (middle), and water vapour (bottom) molar fraction in the MPL and GDL at different permeabilities at $0.06\,\mathrm{A\,cm}^{-2}$

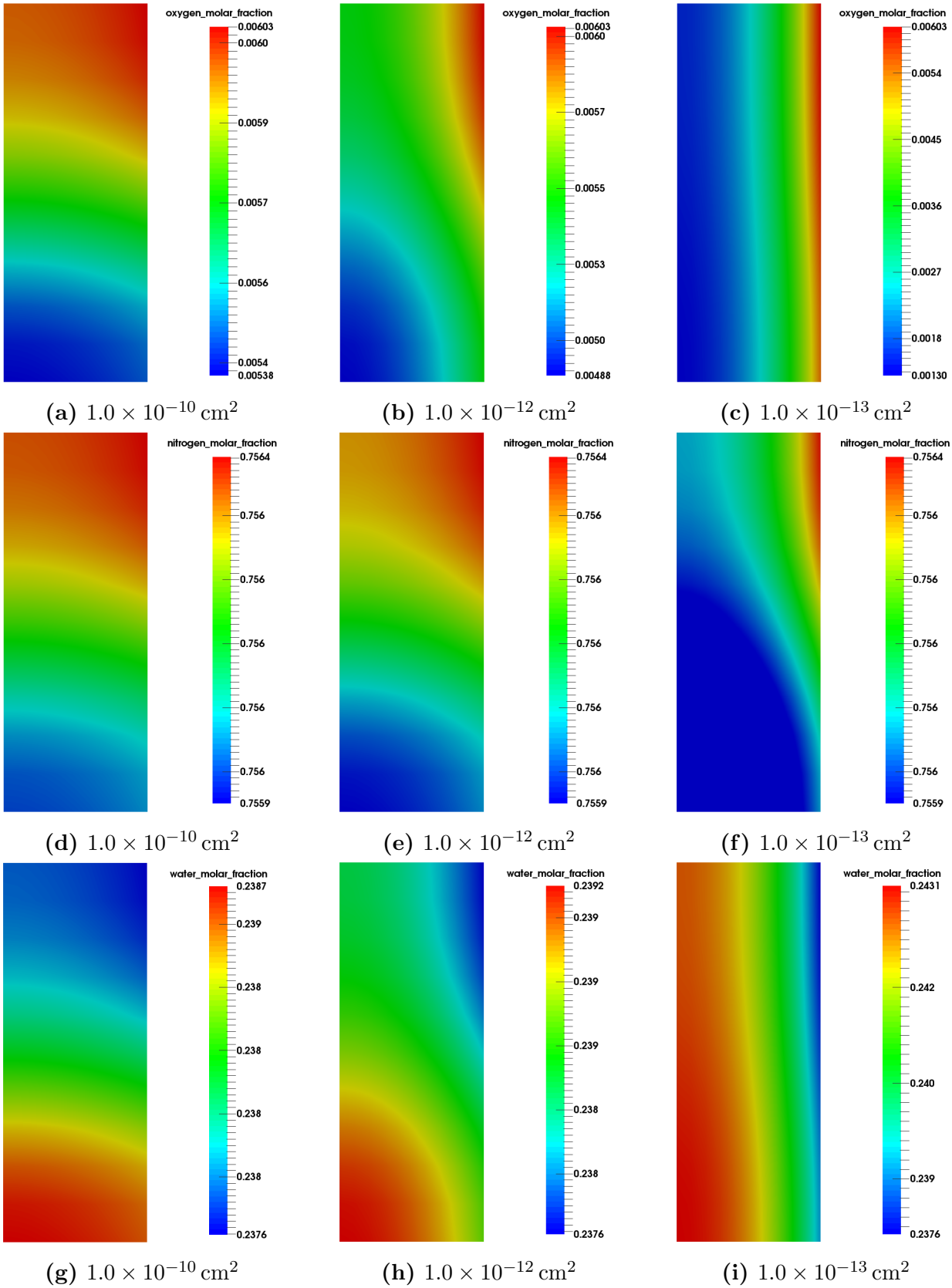

(a) $1.0 \times 10^{-10}\,\mathrm{cm}^2$ **(b)** $1.0 \times 10^{-12}\,\mathrm{cm}^2$ **(c)** $1.0 \times 10^{-13}\,\mathrm{cm}^2$

(d) $1.0 \times 10^{-10}\,\mathrm{cm}^2$ **(e)** $1.0 \times 10^{-12}\,\mathrm{cm}^2$ **(f)** $1.0 \times 10^{-13}\,\mathrm{cm}^2$

(g) $1.0 \times 10^{-10}\,\mathrm{cm}^2$ **(h)** $1.0 \times 10^{-12}\,\mathrm{cm}^2$ **(i)** $1.0 \times 10^{-13}\,\mathrm{cm}^2$

Figure 4.10 – CathodeKG model oxygen (top), nitrogen (middle), and water vapour (bottom) molar fraction in the CL at different permeabilities at $0.06\,\mathrm{A\,cm}^{-2}$

In a reverse trend from oxygen and nitrogen, Figures 4.10g) through i) display that more water exists in the CL at lower permeabilities. Using the same argument that oxygen has a difficult time permeating through the CL at lower permeabilities, water vapour has a difficult time leaving the CL at lower permeabilities. This further compounds the problem with oxygen entering the CL, as the water vapour blocks the platinum reaction sites and prevents the oxygen from permeating into the CL.

Due to the fact that both models assume that water is only in the vapour phase the relative humidity needs to be considered. If the relative humidity inside the cathode is above a value of 1.0 then the water is condensing and forming into a liquid, and a two-phase model would be required to properly model the transport of water inside the cathode. Figure 4.11 shows the relative humidity for the two extreme permeability cases at the lowest voltage considered (0.2 V). At this extreme case, both permeabilities show that the assumption that water is in the vapour phase is valid.

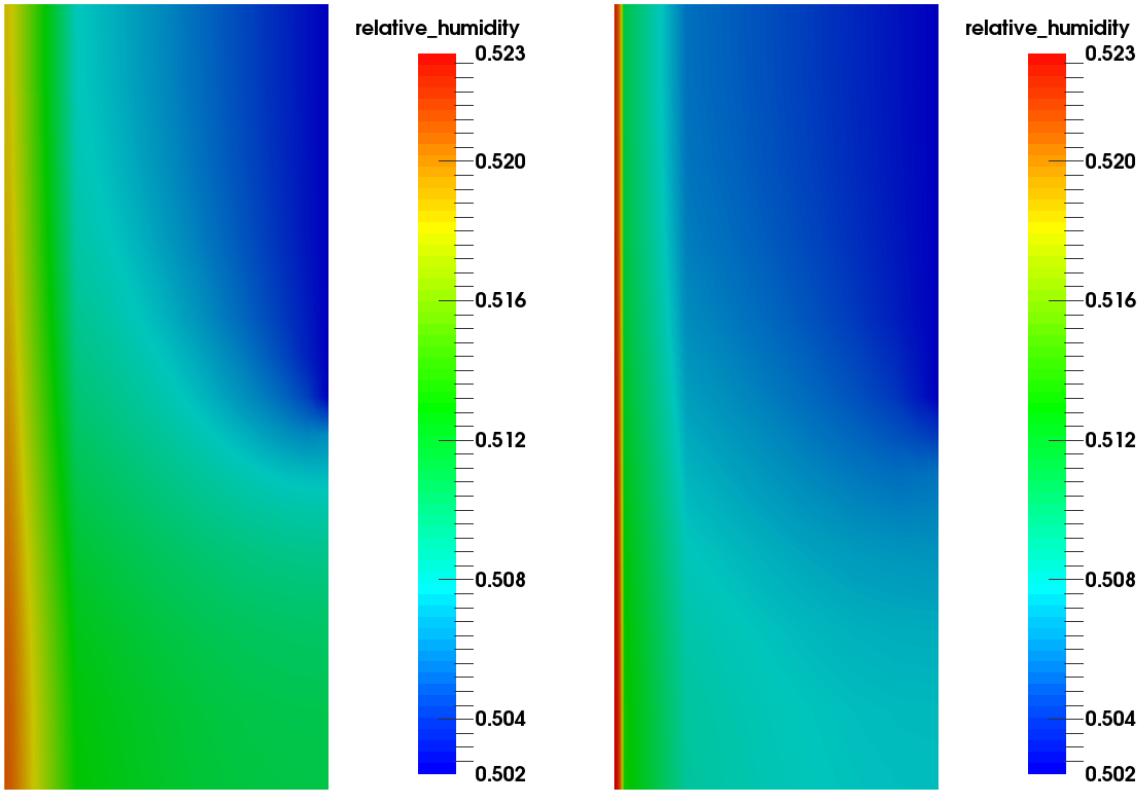

(a) $1.0 \times 10^{-10}\,\mathrm{cm}^2$ **(b)** $1.0 \times 10^{-13}\,\mathrm{cm}^2$

Figure 4.11 – Relative humidity in cathode at 0.2 V for different CL permeabilities using the CathodeKG model

4.4.4.2 Varying the Concentration of Oxygen at the Inlet

Simulations were done to determine the effect of oxygen concentration at the inlet on the CathodeKG model. Oxygen concentrations of 10% and 21% (before humidification) were used. 21% was used as the upper limit because this is the molar fraction in air, and typical fuel cells use air as the source of oxygen for the cathode. 10% was selected because this point is approximately half-way between 1%, previously studied, and 21%. For these figures, every other point is shown with a marker. This was done so the figure would not become unreadable from having data points every 0.025 V.

Figures 4.12 and 4.13 display experimental polarization curves from [136] corrected for membrane Ohmic losses and cross-over losses, and predicted polarization curves from the Cathode and CathodeKG model at these oxygen inlet concentrations. Once again the permeability of the CL was varied to see its effect.

The previous section discussed how at 1% oxygen (before humidification) the transport is binary diffusion dominated and the two models should converge. This was shown in Figure 4.6 where the predictions at a CL permeability of $1.0 \times 10^{-10}\,\mathrm{cm}^2$ with the CathodeKG model nearly coincided with the Cathode model. Figures 4.12 and 4.14 once again show that for a CL permeability of $1.0 \times 10^{-10}\,\mathrm{cm}^2$ the polarization curve is closest to the results of the Cathode model. However, as the oxygen concentration at the inlet is increased the difference between the limiting current increases between the two cases. This difference in limiting currents demonstrates the errors associated with 1) not including a momentum equation in the cathode, and 2) assuming an infinitely dilute solution of oxygen in nitrogen. At 21% in the limiting current density region (0.1 V) this error is approximately 5.9%. This value is similar to the difference noticed by Martínez et al. [49] mentioned in section 1.3.1. Martínez et al. noticed a maximum error of 5% [49] from the Maxwell-Stefan equations, however they were considering a full MEA in the commercial code STAR CD. As well, it was the approximated multi-component (AMC) model, which is based on Fick's law, that was being compared to the Maxwell-Stefan equations.

Figure 4.14 displays the molar fraction of oxygen on a horizontal line along the middle of the cathode. Unlike Figure 4.7, which was at 1%, the error of the infinitely dilute solution assumption begins occurring in the GDL. From Figures 4.13 through 4.14 it is seen that Fick's law over-predicts the results as the infinitely dilute assumption becomes less accurate. With the current Cathode model, the error due to not accounting for Darcy's law and assuming an infinitely dilute solution cannot be separated to determine their individual contribution to the error. For this reason, it would be beneficial if the Cathode model was implemented with Darcy's law so these errors can be analyzed individually.

At 10% oxygen (before humidification) the simulation results shown in Figure 4.12 once

again shows similar trends as the experimental data, but the values are still lower than those from the simulations. At 21% oxygen (before humidification) the simulation results now coincide with the experimental data in the Kinetic and Ohmic regions of the polarization curve. This could be because the oxygen concentration is high and current densities are sufficiently low such that the oxygen concentration along the channel does not change significantly along the channel. Thus, validating the assumption used in through the channel simulations. The experimental data in Figure 4.13 even shows similar results in the Mass Transport region of the polarization curve as the simulation results for the $1.0 \times 10^{-13}\,\mathrm{cm}^2$ CL permeability.

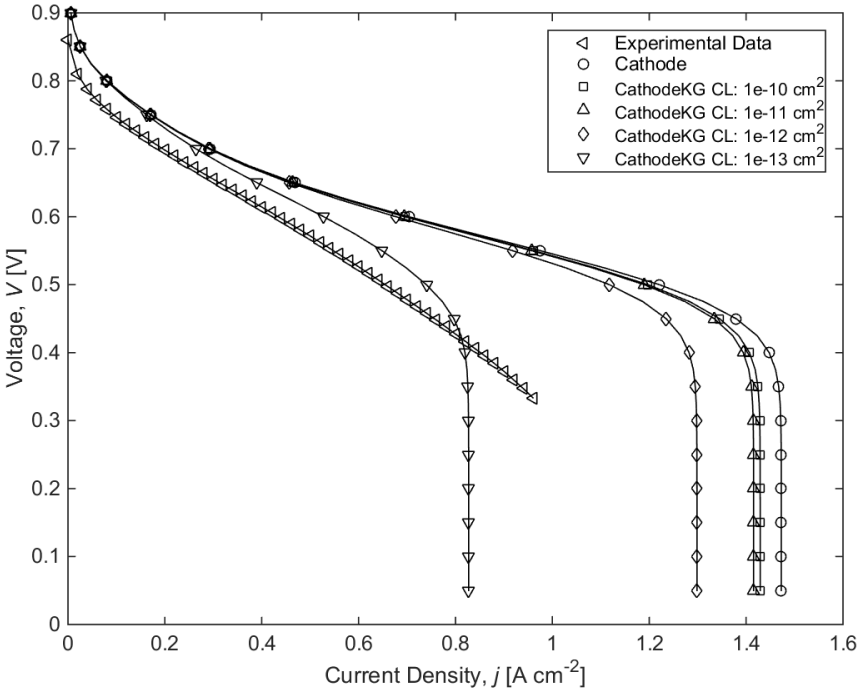

Figure 4.12 – Polarization curves comparing the Cathode and CathodeKG model with 10% oxygen at the inlet (before humidification)

Once again the relative humidity needs to be considered. Figure 4.15 displays the results for 21% oxygen (before humidification) at the inlet. Figure 4.15 was done at the highest current density simulated for this case (0.05 V) and does not show a relative humidity above a value of 1.0. These results confirm that the use of a single phase model is acceptable under the operating conditions simulated.

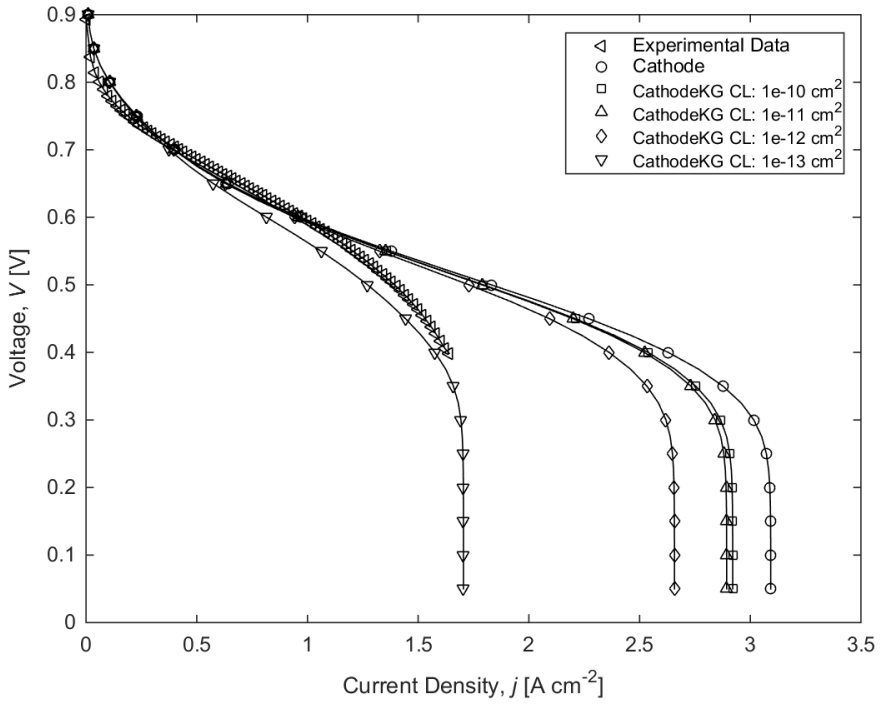

Figure 4.13 – Polarization curves comparing the Cathode and CathodeKG model with 21% oxygen at the inlet (before humidification)

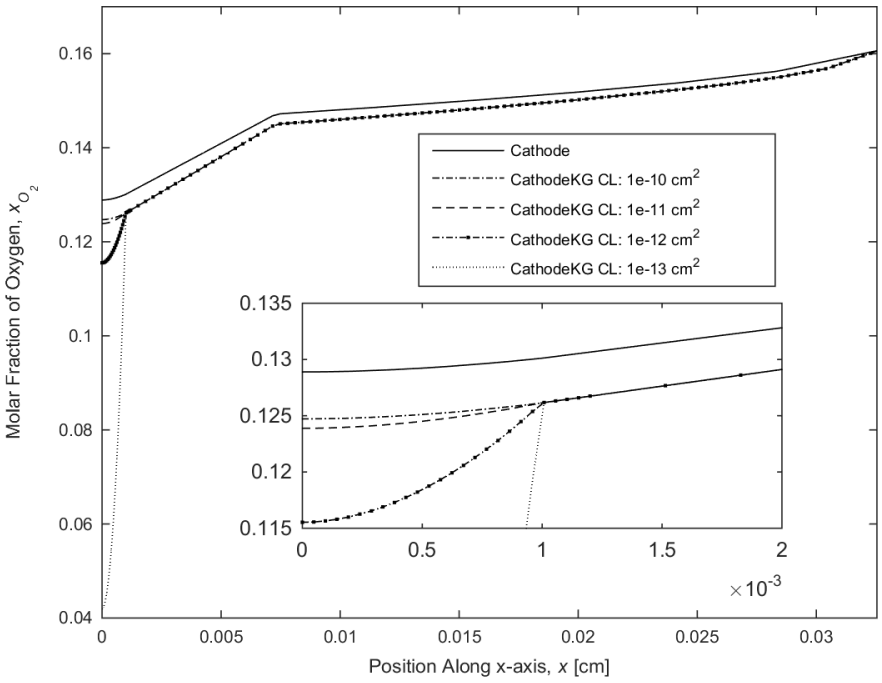

Figure 4.14 – Molar fraction of oxygen at $y = 0.0395\,\mathrm{cm}$ with 21% oxygen at the inlet (before humidification) at $1.0\,\mathrm{A\,cm^{-2}}$

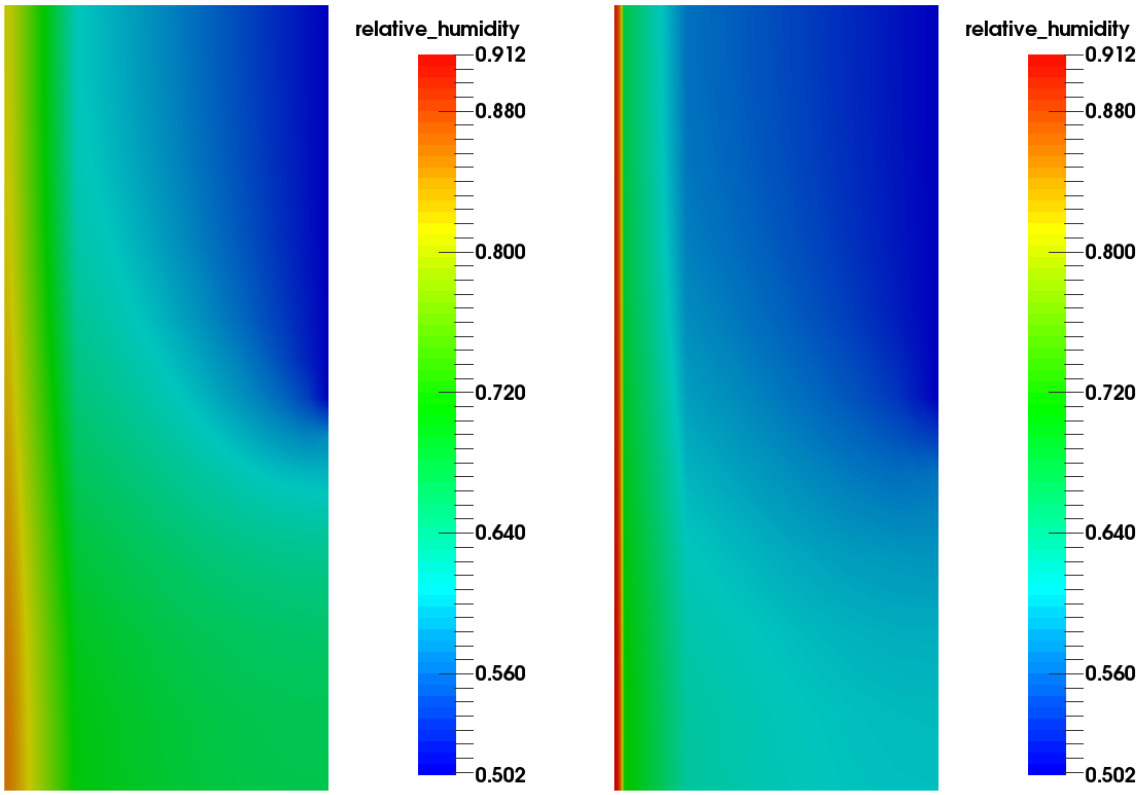

(a) $1.0 \times 10^{-10}\,\mathrm{cm}^2$ **(b)** $1.0 \times 10^{-13}\,\mathrm{cm}^2$

Figure 4.15 – Relative humidity in cathode at 0.05 V for different CL permeabilities using the CathodeKG model for 21% oxygen (before humidification) at the inlet

4.4.4.3 Velocity of Individual Gas Species in Cathode

Kerkhof and Geboers' model predicts the transport of the individual species in the cathode. In this section, the flow profile of the individual gas species is analyzed. Figure 4.16 displays the velocity of the individual gas species in the cathode at $1.0\,\mathrm{A\,cm^{-2}}$ with 21% oxygen (before humidification) at the inlet. The arrow length is not scaled by the velocity magnitude, instead the arrows are coloured based on the velocity magnitude. The colour of the background represents the different layers. This was done so the effects of the species entering or leaving the different porous layers can more easily be seen. As well, the square meshing is shown in the background. This was done so the areas selected for refinement can be seen in relation to the velocity profile.

Figures 4.16a) and b) show the oxygen and water vapour velocities the oxygen. The oxygen flows towards the CL and the water vapour flows in the opposite direction to leave through the channel. Both the oxygen and water vapour tend to travel in a straight line near the upper symmetric boundary. The water near the bottom symmetric boundary gradually curves to leave through the inlet, while the oxygen displays a similar trend in the opposite direction to enter the regions with the least amount of oxygen. As well, at the CL-MPL interface the flow is nearly parallel as the oxygen and water are furthest away from the inlet and entrance effects have less of an affect on the flow. The magnitude of velocity for the water vapour is greater than the oxygen near the channel. This is because for every one oxygen molecules entering the domain there are two molecules of water vapour leaving the domain. The larger total mass of water vapour leaving the cathode is possibly dragging the oxygen out of the channel, thus reducing the speed of the oxygen entering. It should be remembered that, because only the cathode is being modeled, mass is not conserved in the system. This is because from the ORR occurring in the cathode:

$$\frac{1}{2}O_2 + 2H^+ + 2e^- \rightleftharpoons H_2O \tag{4.54}$$

that protons are entering the domain from the PEM-CL interface.

Figure 4.16c) displays the velocity of nitrogen. The velocity of nitrogen is significantly lower than the other species as it is an inert gas. It may be difficult to see all of them, but there are three recirculation regions in the flow of the nitrogen. These flow profiles are more easily seen in Figure 4.16d) where the nitrogen streamlines are shown in the cathode. The recirculation regions are most likely due to the competing effects of the transport of oxygen and water in the porous layers. Due to the fact that nitrogen is inert in the reaction, at steady-state it is pulled in the same direction as the species that dominates the flow in that region. When the nitrogen flows up towards the inlet the water is the significant factor in determining mass transport. When nitrogen flows down to the lower symmetric boundary, oxygen is the significant factor in determining mass transport.

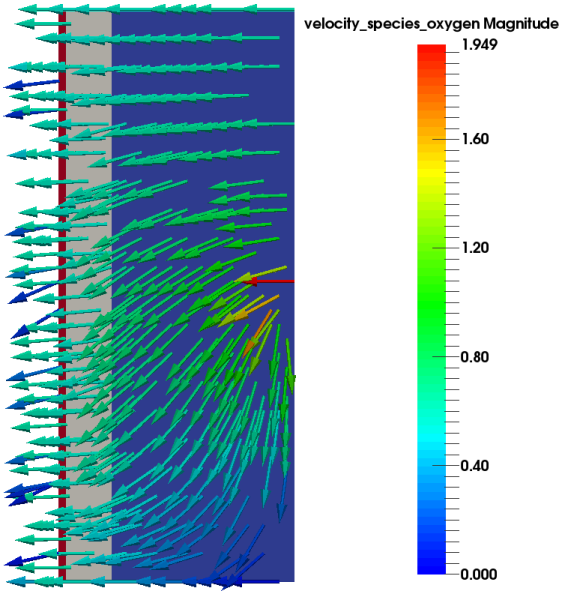

(a) Velocity profile of oxygen

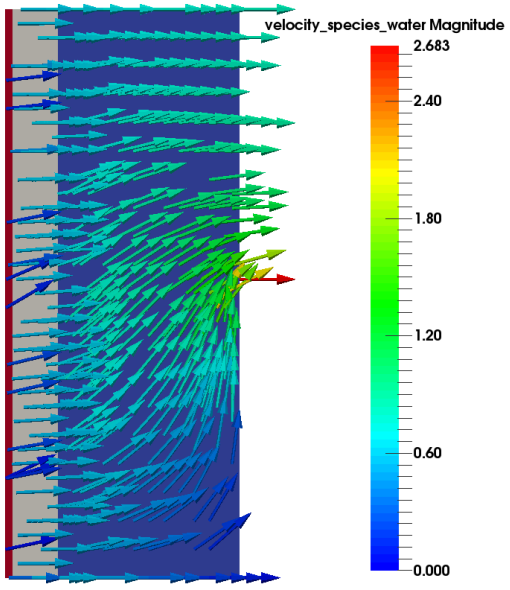

(b) Velocity profile of water vapour

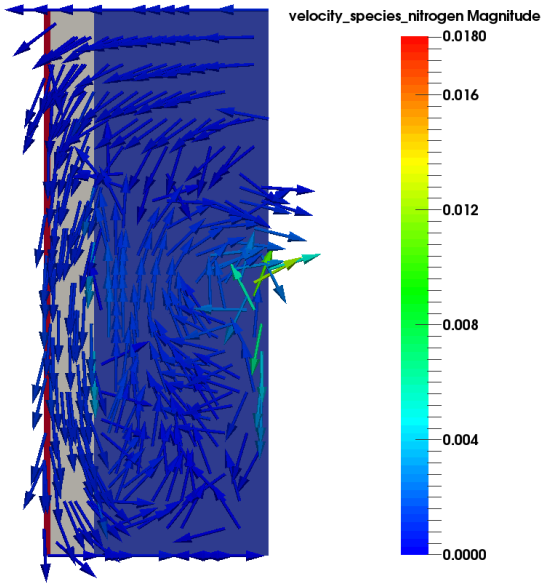

(c) Velocity profile of nitrogen

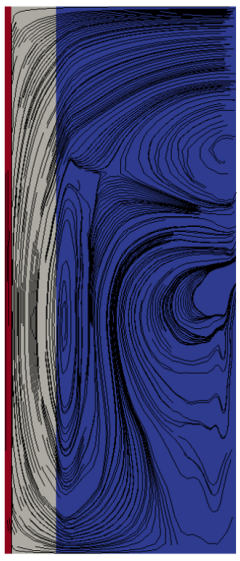

(d) Nitrogen streamlines

Figure 4.16 – Velocity of each species in the CathodeKG model at a CL permeability of $1.0 \times 10^{-10}\,\mathrm{cm}^2$ and $1.0\,\mathrm{A\,cm}^{-2}$

4.4.4.4 Changes in Density

A few models have accounted for the compressibility of gases [70, 77, 138], however it is not usually discussed significantly. The most that is said on this topic in [70, 77, 138] is that the density varies so a "compressible gas technique was used to determine the density of the gas mixture" [138]. Thus far a quantification of the changes in mixture density has not been reported.

A CL permeability of $1.0 \times 10^{-10}\,\mathrm{cm}^2$ was used as this is the limiting case that most closely matches the Cathode model. If a lower permeability was used, based on the previous discussions, it is expected that the the effects in change in density would be even more significant. Figure 4.17a) displays the change in total density across the cathode at the limiting current density. The change in total density across the cathode is approximately 8.6%. Figures 4.17b) through d) show the change in partial density throughout the cathode for each gas species at the limiting current density. The smallest change in partial density occurs for nitrogen, with a change of approximately 8.8%. The oxygen and water have a change in partial density across the cathode of 68.6% and 69.7% respectively. The change in density for oxygen and water vapour is quite significant. Future work should be done to compare simulations using the classical approach and the new CathodeKG model. Only then can it be determined how sensitive the transport and performance results are to this different assumption.

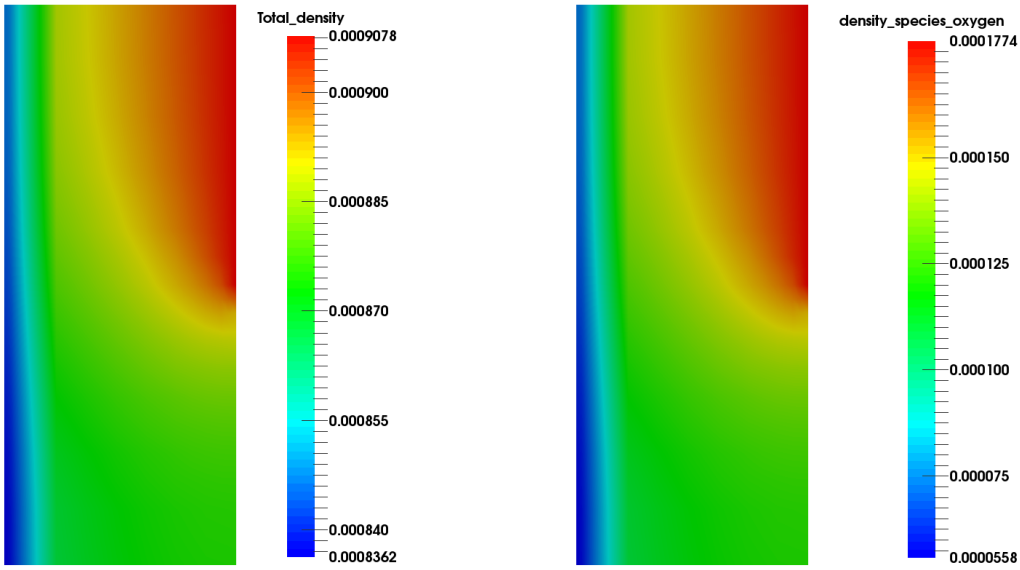

(a) Total density of the mixture

(b) Partial density of oxygen

(c) Partial density of water vapour

(d) Partial density of nitrogen

Figure 4.17 – Change in density of CathodeKG model at a CL permeability of $1.0 \times 10^{-10}\,\mathrm{cm}^2$ and 0.05 V and $2.92\,\mathrm{A\,cm}^{-2}$

4.5 Along the Channel Cathode Model

Through the channel simulations assume that there is a sufficient supply of oxygen along the entire channel. This can only be achieved at very high air flow rates. In reality, air flow rates are small and more oxygen is available near the entrance of the channel than at the outlet of the channel. Along the channel simulations aim at predicting the distribution of oxygen along the entire channel. This means that unlike in the through the channel simulation the channel, which is dominated by convective transport, must also be included in the domain. The Cathode model, is unable to consider this domain because it only considers a Fickian transport model. For this reason, it cannot account for the convective transport in the channel.

To see the effects of the distribution of oxygen along the channel the flow rate at the inlet was varied such that λ_{stoic} was varied from 2 to 10. A λ_{stoic} of one means that all oxygen entering the channel would be consumed. As λ_{stoic} increases there is excess oxygen in the channel.

4.5.1 Domain

Figure 4.18 displays a schematic of the domain considered. A straight through bipolar plate design is used, with similar dimensions to those in section 4.4.1. The length of the channel is based on the dimensions of the bipolar plate used by the ESDL, which is 0.81″ (2.1 cm). To reduce computational expense, less of the channel was considered in the entrance and exit regions, and a parabolic profile was prescribed at the outlet. The final mesh consisted of 8 cells for the each of the different layers in the x-direction.

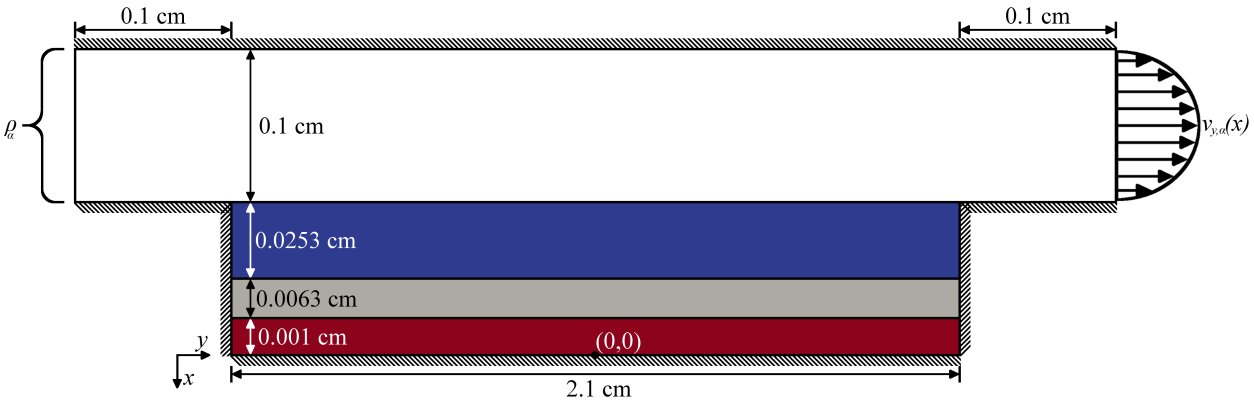

Figure 4.18 – Along-channel PEFC cathode domain (not to scale)

4.5.2 Boundary Conditions

For a stable convergent solution it was found that the outlet boundary condition had to be Dirichlet velocity and the inlet boundary conditions had be a Dirichlet density and normal shear stress free. At the inlet and outlet a no-flux boundary condition is used for the protonic and electronic potentials. The outlet boundary conditions are expressed mathematically as follows:

$$v_{y,\alpha}(x) = -U_{max}(1.729104 + 66.08\,x + 400\,x^2) \text{ on } x \in [-0.0326, -0.1326],\ y = 1.15 \tag{4.55}$$

$$v_{x,\alpha} = 0\,\mathrm{cm\,s^{-1}} \qquad \text{on } x \in [-0.0326, -0.1326],\ y = 1.15 \tag{4.56}$$

$$\boldsymbol{N}_{H^+} \cdot \boldsymbol{n} = \boldsymbol{N}_{e^-} \cdot \boldsymbol{n} = 0 \qquad \text{on } x \in [-0.0326, -0.1326],\ y = 1.15 \tag{4.57}$$

where U_{max} is calculated for different λ_{stoic} values based on the calculations shown Appendix C. The inlet boundary conditions are expressed mathematically as follows:

$$\oint_\Gamma \left(P_\alpha \hat{\mathbf{I}} - \hat{\boldsymbol{\tau}}_\alpha\right) \boldsymbol{w}_\alpha \cdot \boldsymbol{n}\,\mathrm{d}\Gamma = 0 \qquad \text{on } x \in [-0.0326, -0.1326],\ y = -1.15 \tag{4.58}$$

$$\rho^0_{O_2},\ \rho^0_{N_2},\ \rho^0_{H_2O} \qquad \text{on } x \in [-0.0326, -0.1326],\ y = -1.15 \tag{4.59}$$

$$\boldsymbol{N}_{H^+} \cdot \boldsymbol{n} = \boldsymbol{N}_{e^-} \cdot \boldsymbol{n} = 0 \qquad \text{on } x \in [-0.0326, -0.1326],\ y = -1.15 \tag{4.60}$$

where the densities of the individual species are calculated from ideal gas law by the `Operating Conditions` class at 101 325 Pa, 353.15 K, 50% RH, and an initial oxygen mole fraction (prior to humidification) of 21%.

For the upper wall the boundary conditions for the protonic and electronic potentials are done similar to section 4.4.2.1. The difference is that this time there is no bipolar plate boundary to apply the electronic and protonic potential boundary conditions. Instead the roof of the channel is treated as the bipolar plate, and this point will be used to regulate the voltage. As a result, the channel is treated as having an effective electronic conductivity of $1000\,\mathrm{S\,cm^{-1}}$. The boundary conditions for the bipolar plate boundary and the CL-membrane interface are expressed mathematically as:

$$\boldsymbol{N}_{H^+} \cdot \boldsymbol{n} = 0 \qquad \text{on } x = -0.1326,\ y \in [-1.15, 1.15] \tag{4.61}$$

$$\phi_s = \phi_0 \qquad \text{on } x = -0.1326,\ y \in [-1.15, 1.15] \tag{4.62}$$

$$\phi_m = 0 \qquad \text{on } x = 0,\ y \in [-1.05, 1.05] \tag{4.63}$$

$$\boldsymbol{N}_{e^-} \cdot \boldsymbol{n} = 0 \qquad \text{on } x = 0,\ y \in [-1.05, 1.05] \tag{4.64}$$

where ϕ_0 is the voltage (V) applied.

Finally, for all other boundaries not mentioned a no-slip and no-penetration velocity boundary condition and a no flux potential boundary condition was applied, i.e. $\boldsymbol{v}_{O_2} = \boldsymbol{v}_{N_2} = \boldsymbol{v}_{H_2O} = 0\,\mathrm{cm\,s^{-1}}$ and $\boldsymbol{N}_{H^+} \cdot \boldsymbol{n} = \boldsymbol{N}_{e^-} \cdot \boldsymbol{n} = 0$.

4.5.3 Grid Independence and Adaptive Refinement Study

Similar to section 4.4.3 a grid independence study was performed on the CathodeKG model to confirm that the along the channel mesh is in the grid independent region. A λ_{stoic} of 1.78 was used for the GIS and ARS. This λ_{stoic} was chosen because the conditions for $\lambda_{stoic} = 2$ were used and the voltage was lowered to 0.55 V. As well, by using a lower λ_{stoic} the gradients are larger. A permeability of $1.0 \times 10^{-10}\,\mathrm{cm^2}$ was used as all results were done with this permeability. An ARS was then performed on the same mesh to see the effects of using adaptive refinement compared to global refinement. This is because adaptive refinement only refines the mesh where the gradients in solution variables are greatest. This reduces the number of dofs at each refinement level, leading to a less computationally expensive simulation.

Figure 4.19 displays the results for the GIS and ARS. With the exception of the coarsest mesh, all grill levels increased asymptotically. Two levels of global refinement were applied to the mesh before the ARS was performed. This is due to how coarse the initial mesh was. The ARS also converges towards the same solution as the GIS but at a slower rate. As a result, it took less computational time to simply perform three levels of global refinement than to use adaptive refinement and achieve the same accuracy. Based on these results, three levels of global refinement was used in all the following simulations.

4.5.4 Results

As discussed in section 4.4.4, to make a proper comparison when changing a parameter it is best to keep the current density the same. A current density of $1.0\,\mathrm{A\,cm^{-2}}$ was chosen, and the inlet velocity was calculated using the methodology in Appendix C. The problem is that these calculations are based on inlet velocity, but as seen in section 4.5.2 the velocity needs to be specified at the outlet for a stable convergent solution. This is a problem because the velocity and density of oxygen changes along the channel as the oxygen is consumed. For this reason, an iterative process is required to get the necessary inlet velocity for the required λ_{stoic}. The iterative process was found to take two cycles to converge to the correct λ_{stoic}, and the process used was:

1. Set outlet velocity boundary condition to the value desired at the inlet and scan polarization curve to find voltage required for $1.0\,\mathrm{A\,cm^{-2}}$

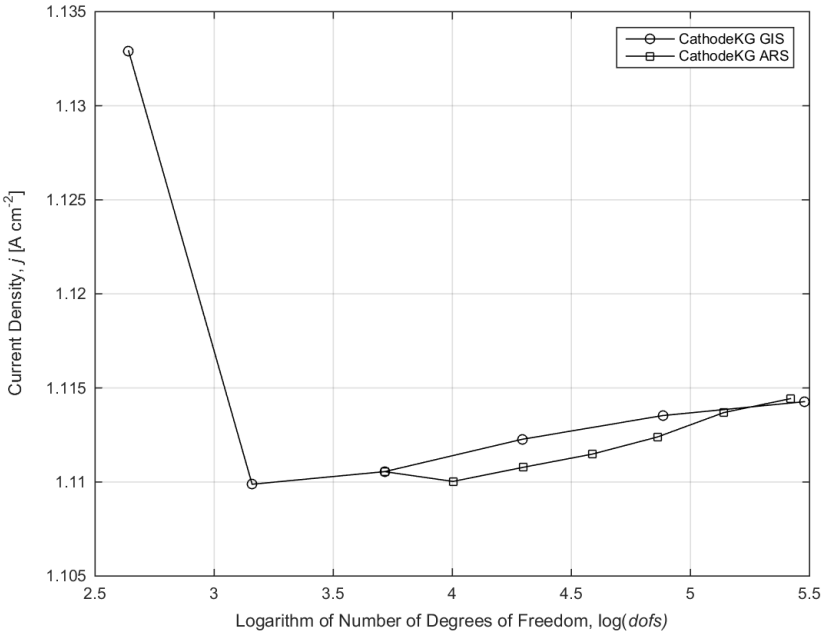

Figure 4.19 – Along the channel global grid independence study (GIS) and adaptive refinement study (ARS) for the CathodeKG model

2. Interpolate voltage to get voltage at $1.0\,\mathrm{A\,cm^{-2}}$ and re-run simulations
3. At $1.0\,\mathrm{A\,cm^{-2}}$ take the difference in velocity at the inlet and outlet and add to outlet
4. Repeat

The final average inlet and outlet velocities for the different λ_{stoic}'s are shown in Table 4.5.

Table 4.5 – Inlet and outlet velocities at various λ_{stoic} values

λ_{stoic}	Average Velocity ($\mathrm{cm\,s^{-1}}$)	
	Inlet	Outlet
2.0	19.62	20.89
3.0	29.41	30.55
5.0	49.01	49.87
10.0	97.99	98.16

As mentioned in section 2.7.2, MUMPS has stability issues when solving problems involving multiple species with convective transport. For this reason, UMFPACK was used for all along the channel simulations, which only uses one thread. Lower λ_{stoic} values took longer to solve. In the case of $\lambda_{stoic} = 2.0$, the final parametric study (four points) to get the results at $1.0\,\mathrm{A\,cm^{-2}}$ took approximately 9 minutes to run. The polarization curve for a $Q_{avg,outlet} = 0.139\,\mathrm{L\,min^{-1}}$ took approximately six hours to run.

4.5.4.1 Polarization Curve

Figure 4.20 displays the polarization curves using the determined outlet boundary conditions from Table 4.5. For the numerical polarization curves, every fifth point is shown with a marker. This was done so the figure would not become unreadable from having data points every 0.01 V. As well, the flow rates were calculated from the velocities in Table 4.5 assuming the fuel cell consists of 14 channels as this is the through channel design used in the ESDL.

At high voltages, the current densities in Figure 4.20 coincide and are independent of the outlet velocity used. This makes sense as the λ_{stoic} is very large and so there are no significant losses from the available amount of oxygen along the channel. This is seen in Figure 4.21 where the λ_{stoic} is plotted for different current densities. The results from the through the channel simulation under the same conditions are also plotted in Figure 4.20. This was done as the through the channel simulation reflects the polarization curve as $\lambda_{stoic} \to \infty$. This displays the upper limit that can be achieved as the flow rate in the cathode is increased. Figure 4.21 displays that at the limiting current there is sufficient oxygen in the channel for higher current densities. However, this is not possible because of mass transport losses that prevent the oxygen from enter the CL fast enough for the reaction to occur at higher current densities.

Figures 4.22 through 4.24 display the molar fraction of the gas species at different λ_{stoic} values. The oxygen molar fraction decreases along the channel, while the water vapour increases along the channel. This is expected because there is less oxygen available further downstream as the oxygen is consumed. Similarly, water vapour has the opposite trend because it accumulates at the outlet as it is being removed from the PEFC. The nitrogen molar fraction, and by extension partial density, decreases along the channel but because nitrogen is inert mass is still conserved. This is done by an increase in the velocity of the nitrogen at the outlet. Figures 4.22 through 4.24 clearly show that the through plane assumption of constant concentration in the channel is not valid even at $\lambda_{stoic} = 10.0$. This is one benefit of along the channel and 3D simulations as they are able to account for this effect that is not accounted for in through the channel simulations.

RH also needs to be considered to ensure that water is not being formed. If the RH is above a value of 1 then the water is condensing into a liquid and the assumption that the water is in the vapour phase is no longer valid. In this case a two-phase model is required to accurately predict the transport of water. Figure 4.25 displays that the RH in the along the channel simulation is always below 1 at a current density of $1.0\,\mathrm{A\,cm^{-2}}$. Figure 4.25 suggests that, if water were formed, it would occur in both the channel and porous layers near the outlet of the channel. Figure 4.26 displays the relative humidity at the limiting current. Although the RH is below 1 for all cases, the lowest flow rate case has a relative

humidity very close to one and water is possibly beginning to form.

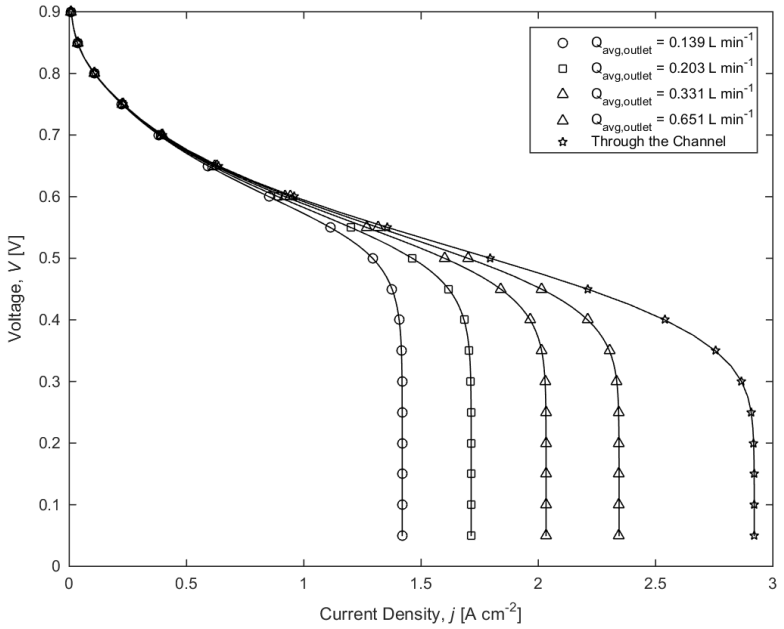

Figure 4.20 – Polarization curve of the along the channel CathodeKG model at different outlet speeds

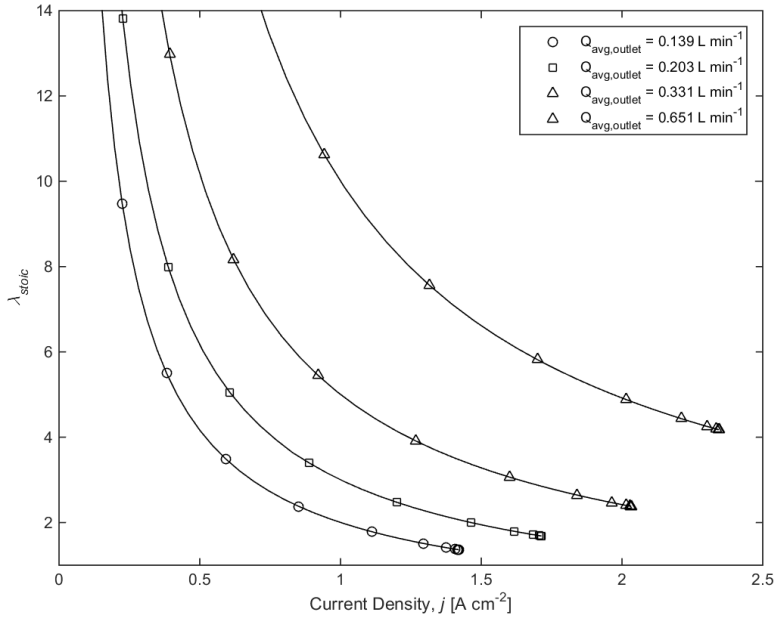

Figure 4.21 – λ_{stoic} of the along the channel the Cathode model to the CathodeKG model at different outlet speeds

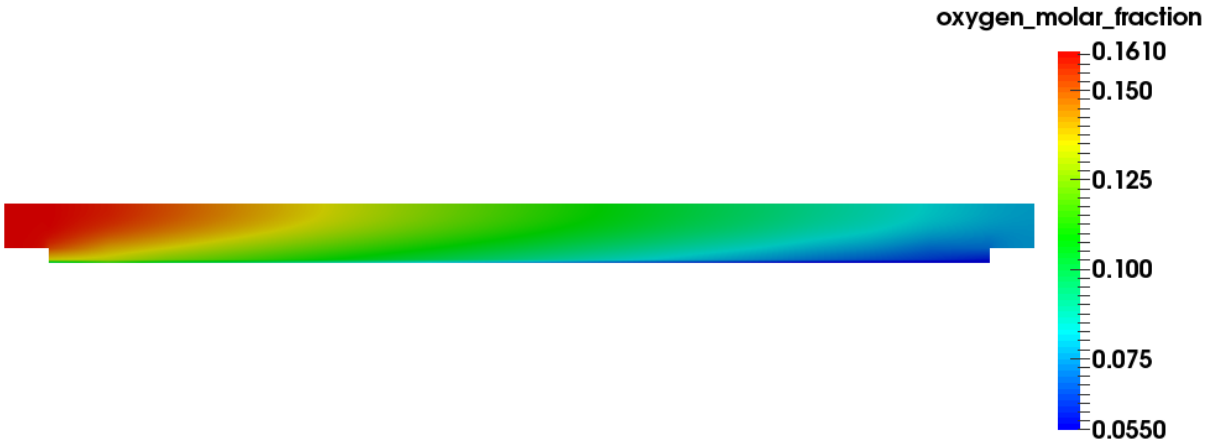

(a) $\lambda_{stoic} = 2.0$

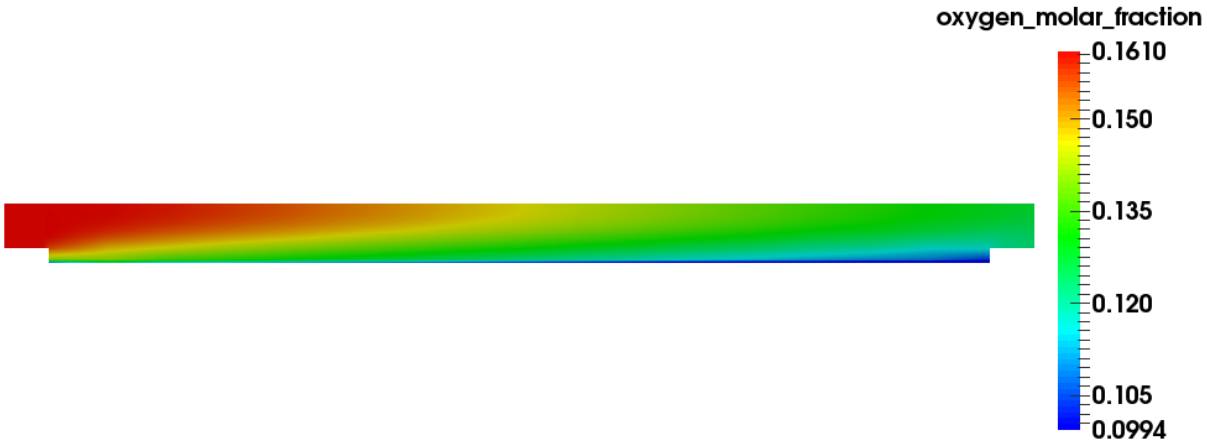

(b) $\lambda_{stoic} = 5.0$

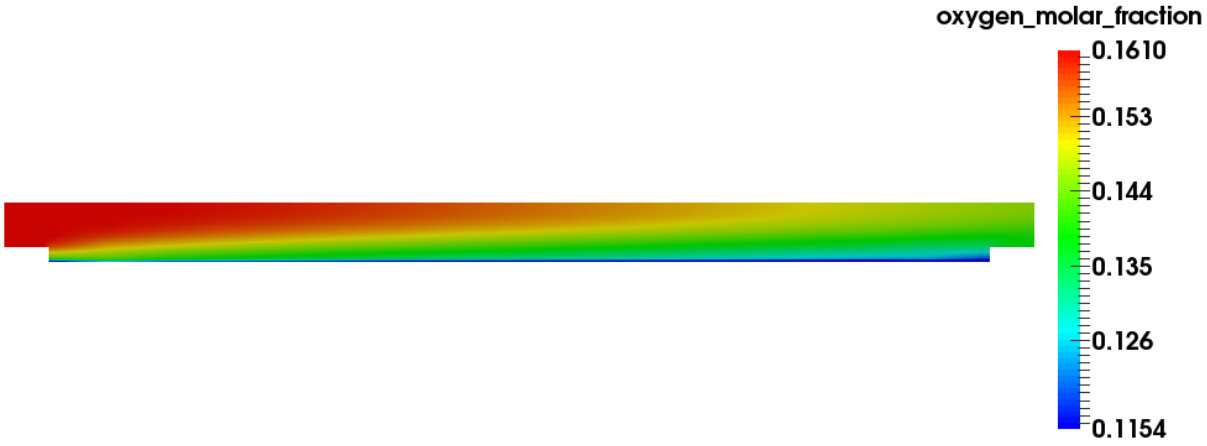

(c) $\lambda_{stoic} = 10.0$

Figure 4.22 – Along Channel CathodeKG model oxygen molar fractions at $1.0\,\mathrm{A\,cm^{-2}}$ for various λ_{stoic} ratios

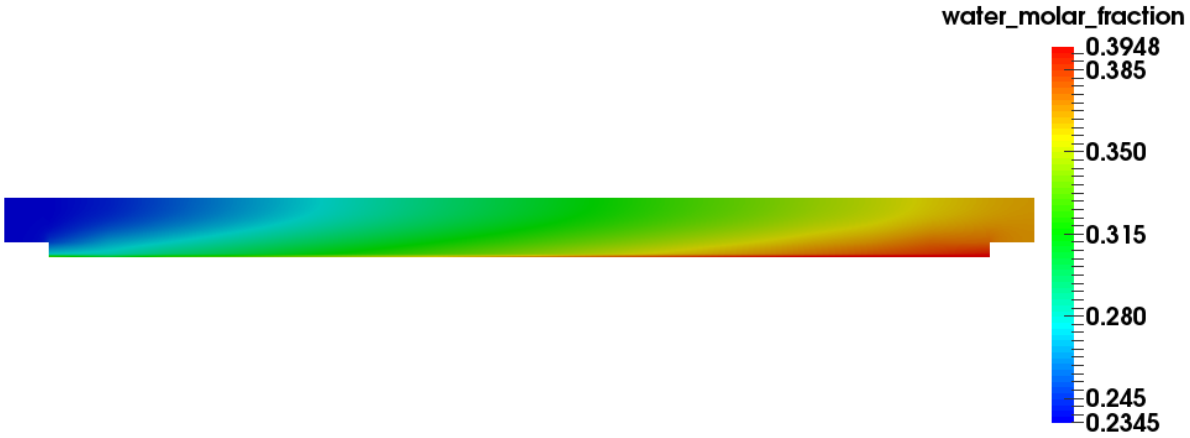

(a) $\lambda_{stoic} = 2.0$

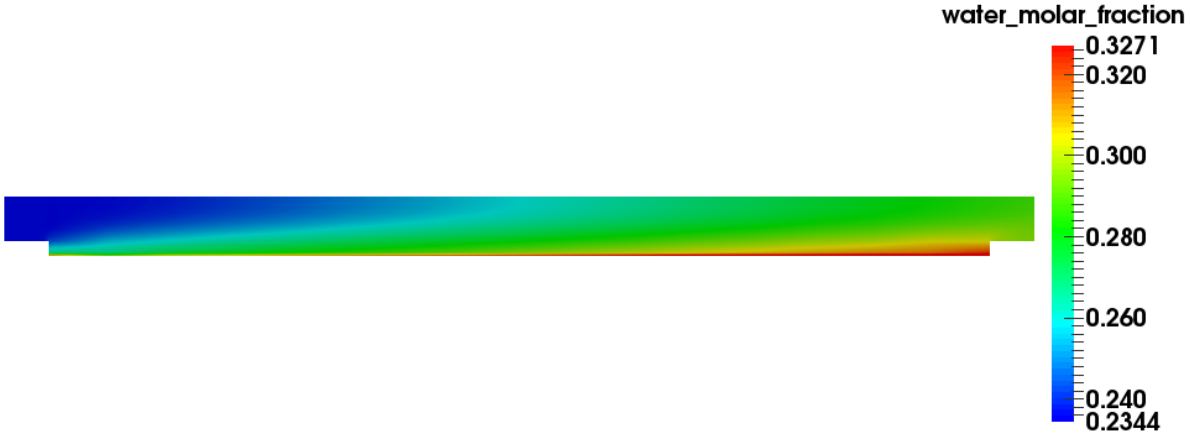

(b) $\lambda_{stoic} = 5.0$

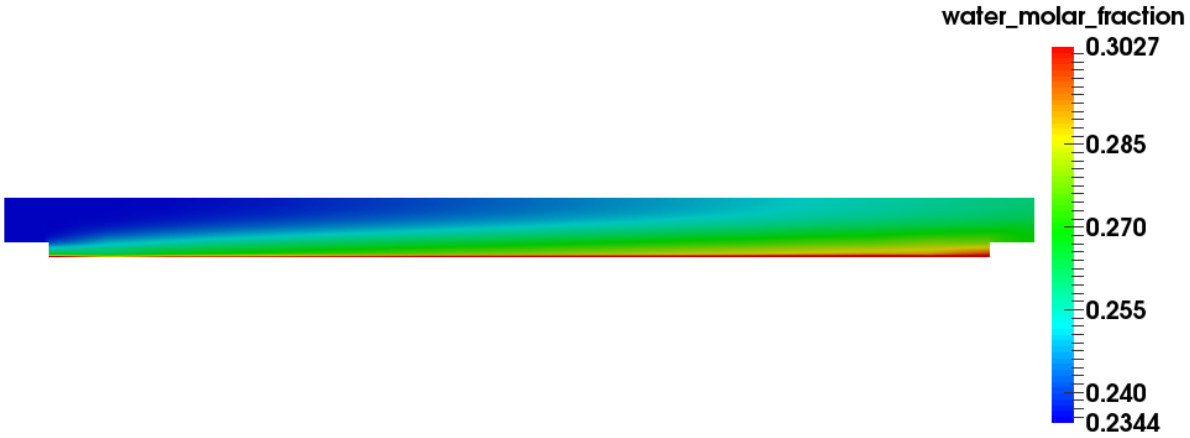

(c) $\lambda_{stoic} = 10.0$

Figure 4.23 – Along Channel CathodeKG model water vapour molar fractions at $1.0\,\mathrm{A\,cm^{-2}}$ for various λ_{stoic} ratios

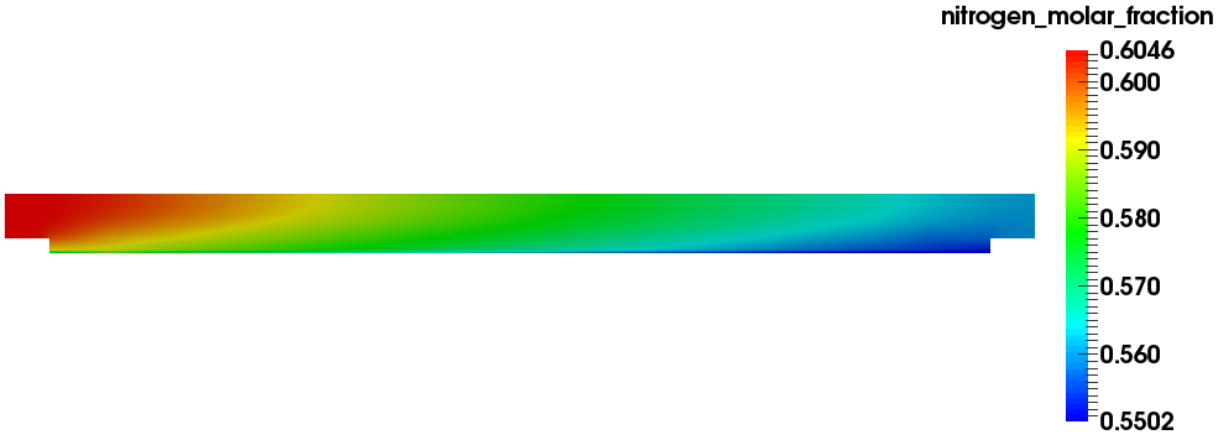

(a) $\lambda_{stoic} = 2.0$

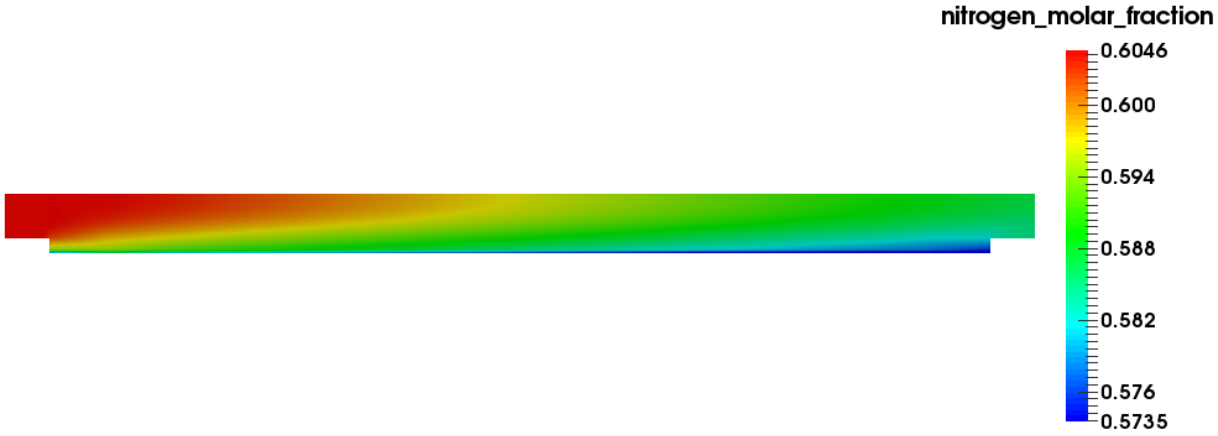

(b) $\lambda_{stoic} = 5.0$

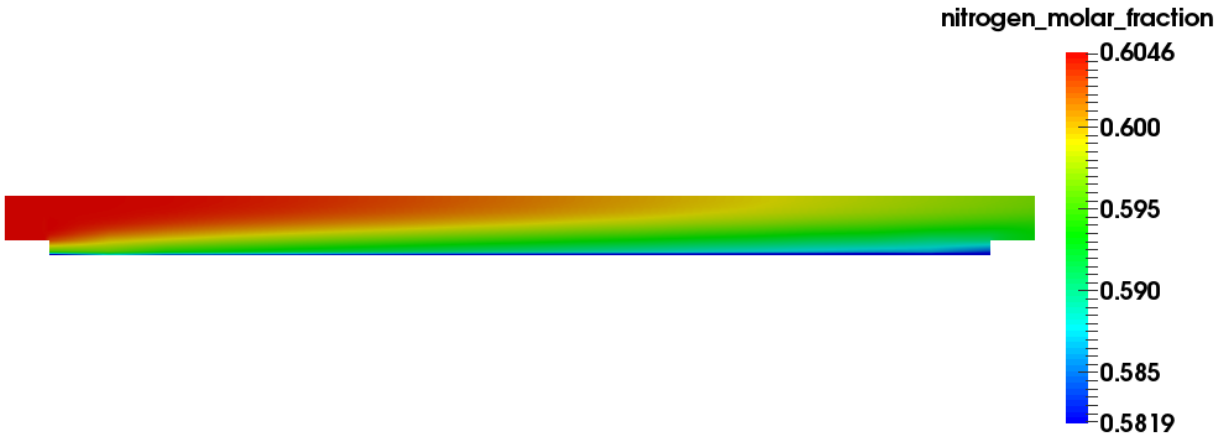

(c) $\lambda_{stoic} = 10.0$

Figure 4.24 – Along Channel CathodeKG model nitrogen molar fractions at $1.0\,\mathrm{A\,cm^{-2}}$ for various λ_{stoic} ratios

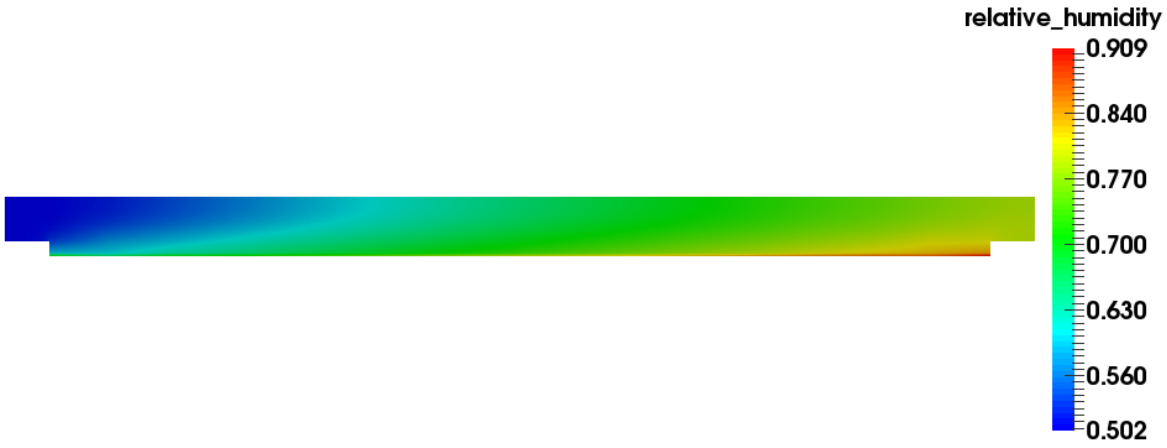

(a) $\lambda_{stoic} = 2.0$

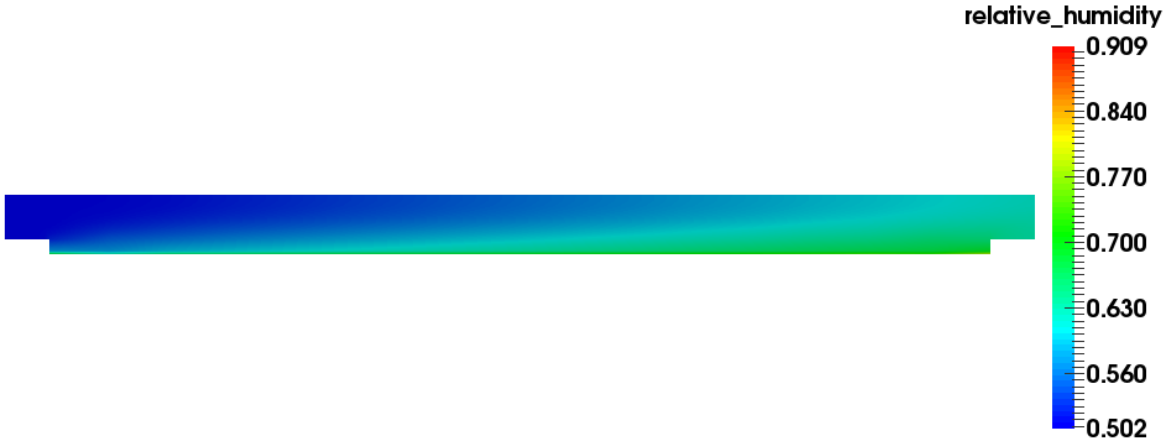

(b) $\lambda_{stoic} = 5.0$

(c) $\lambda_{stoic} = 10.0$

Figure 4.25 – Relative humidity in cathode at $1.0\,\mathrm{A\,cm^{-2}}$ for different λ_{stoic}

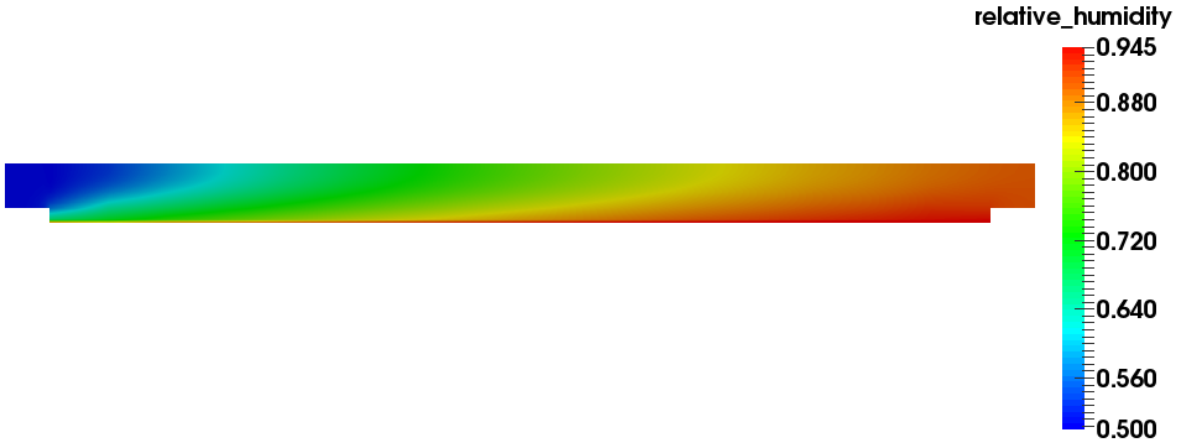

(a) $u_{avg,outlet} = 20.89\,\mathrm{cm\,s^{-1}}$ $(1.685\,\mathrm{A\,cm^{-2}})$

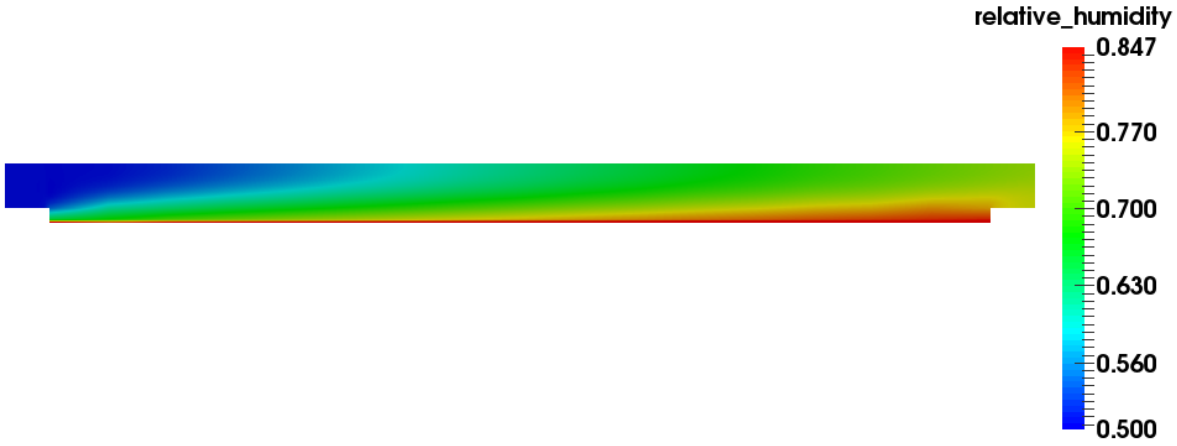

(b) $u_{avg,outlet} = 49.87\,\mathrm{cm\,s^{-1}}$ $(2.378\,\mathrm{A\,cm^{-2}})$

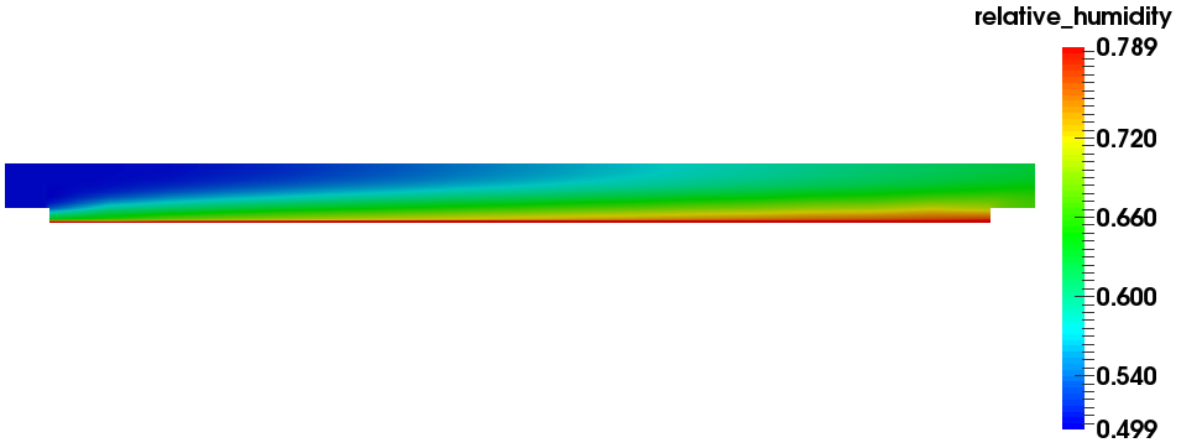

(c) $u_{avg,outlet} = 98.16\,\mathrm{cm\,s^{-1}}$ $(4.174\,\mathrm{A\,cm^{-2}})$

Figure 4.26 – Relative humidity at the limiting current (0.05 V) in the along the channel CathodeKG model for different average outlet flow rates

4.5.4.2 Changes in Density

Figure 4.27 displays how the total density changes along the channel of a PEFC. As mentioned previously, the typical approach used involves the mass-averaged Navier-Stokes equations. For this case, the total density of the mixture is what changes. Figure 4.27 shows that the change in total density is approximately 9.2%, 6.3%, and 5.2% for a λ_{stoic} of 2.0, 5.0, and 10.0 respectively.

Kerkhof and Geboers' model uses a density for each of the individual species. Figures 4.28 through 4.30 display similar results as the through the channel change in density. Similarly to the results for through the channel, the changes are more significant for the oxygen and water vapour compared to the nitrogen. The change in density for oxygen and water vapour ranges from approximately 70 to 30% from λ_{stoic} of 2 to 10. Once again, future work should be done to compare simulations using the classical approach and the new CathodeKG model. Only then can it be determined how sensitive the transport and performance results are to this different assumption.

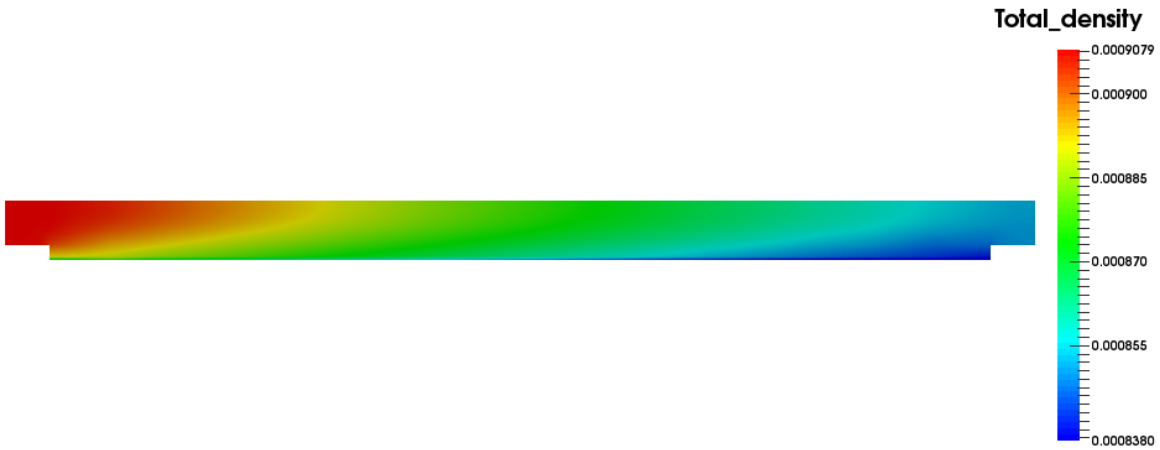

(a) $\lambda_{stoic} = 2.0$

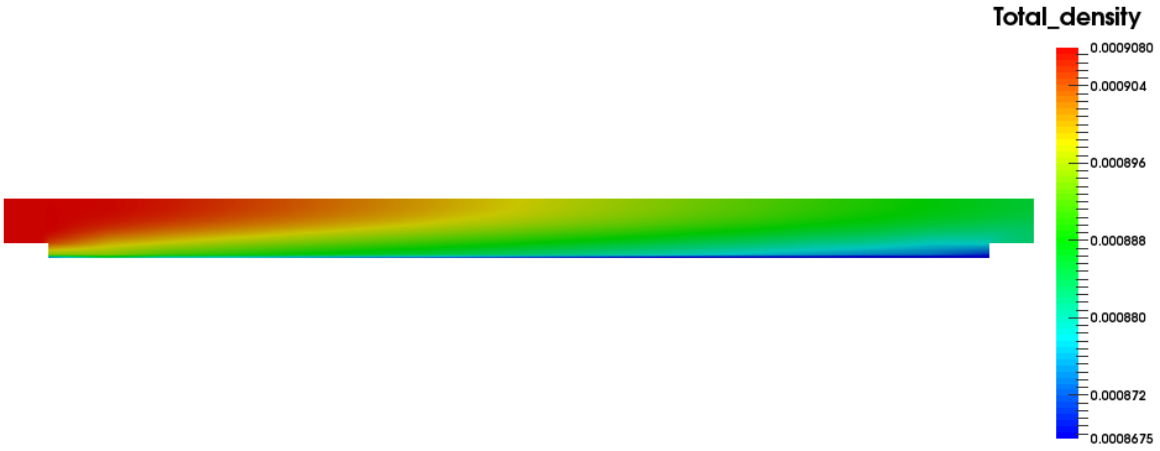

(b) $\lambda_{stoic} = 5.0$

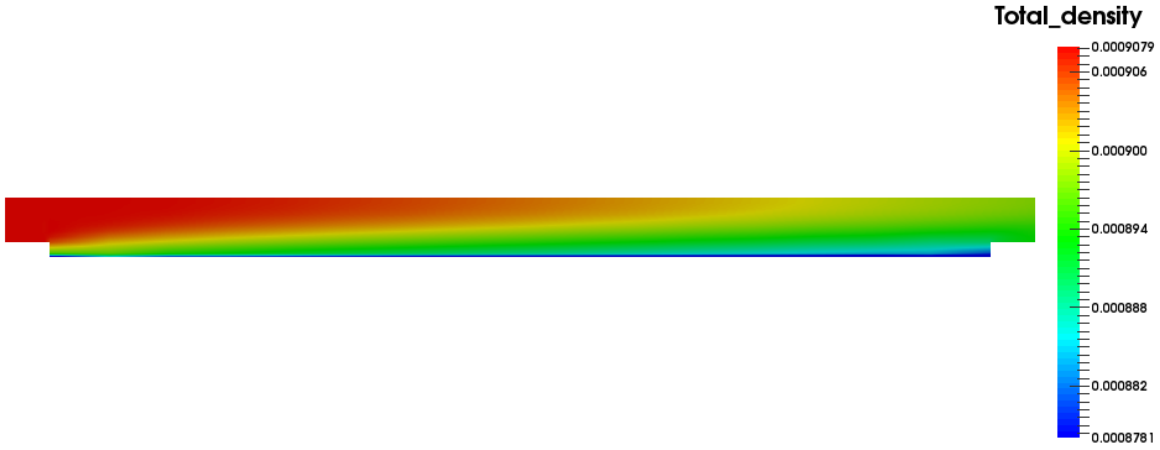

(c) $\lambda_{stoic} = 10.0$

Figure 4.27 – Along Channel CathodeKG model total density at $1.0\,\mathrm{A\,cm^{-2}}$ for various λ_{stoic} ratios

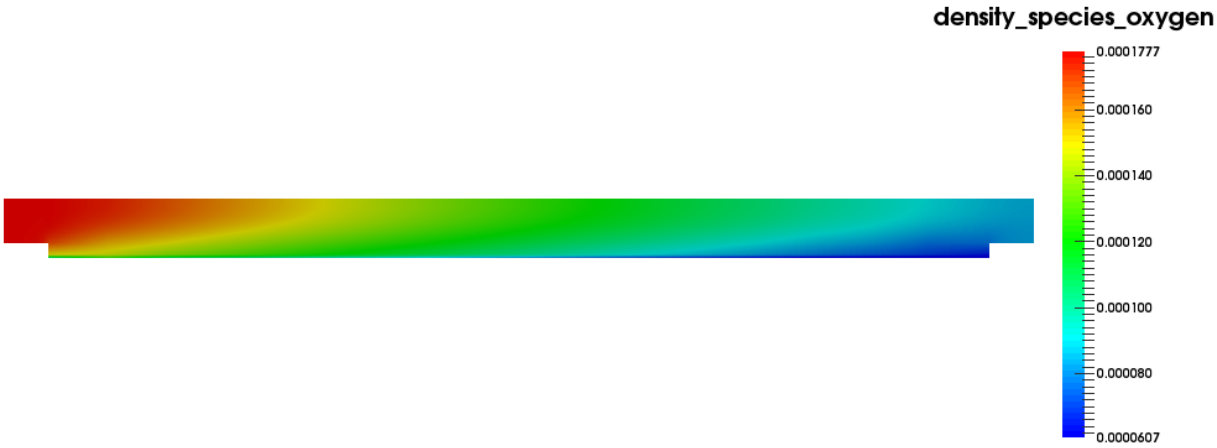

(a) $\lambda_{stoic} = 2.0$

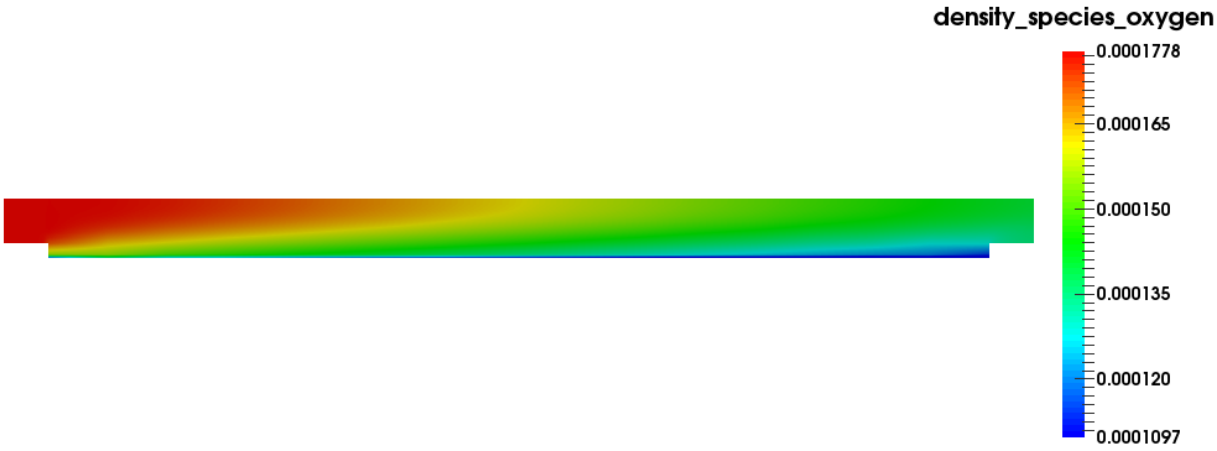

(b) $\lambda_{stoic} = 5.0$

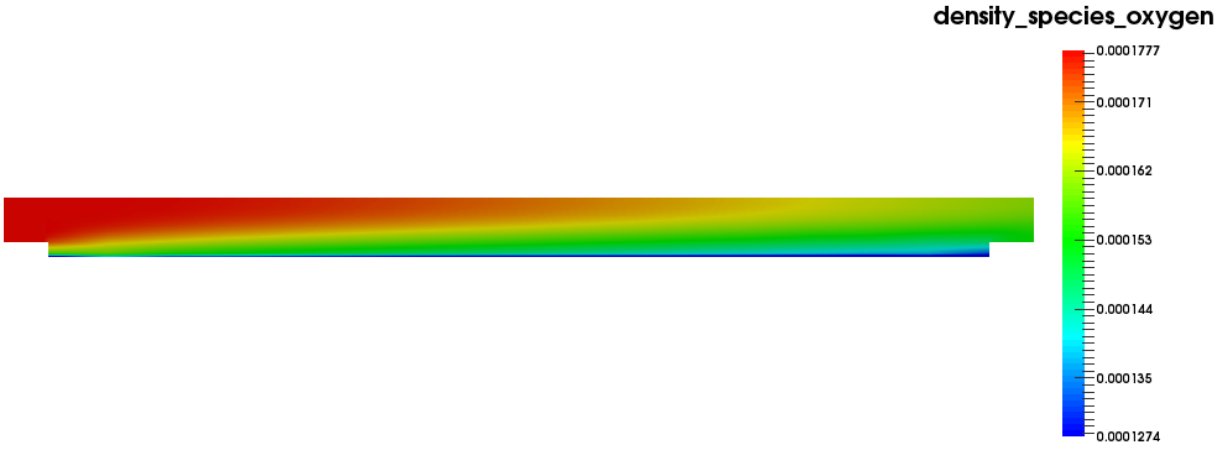

(c) $\lambda_{stoic} = 10.0$

Figure 4.28 – Along Channel CathodeKG model oxygen partial density at $1.0\,\mathrm{A\,cm^{-2}}$ for various λ_{stoic} ratios

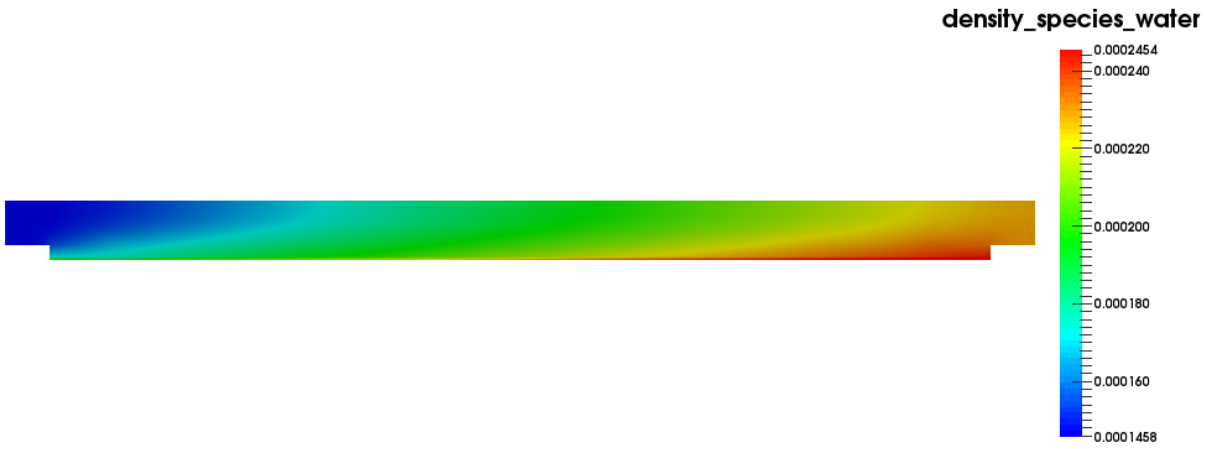

(a) $\lambda_{stoic} = 2.0$

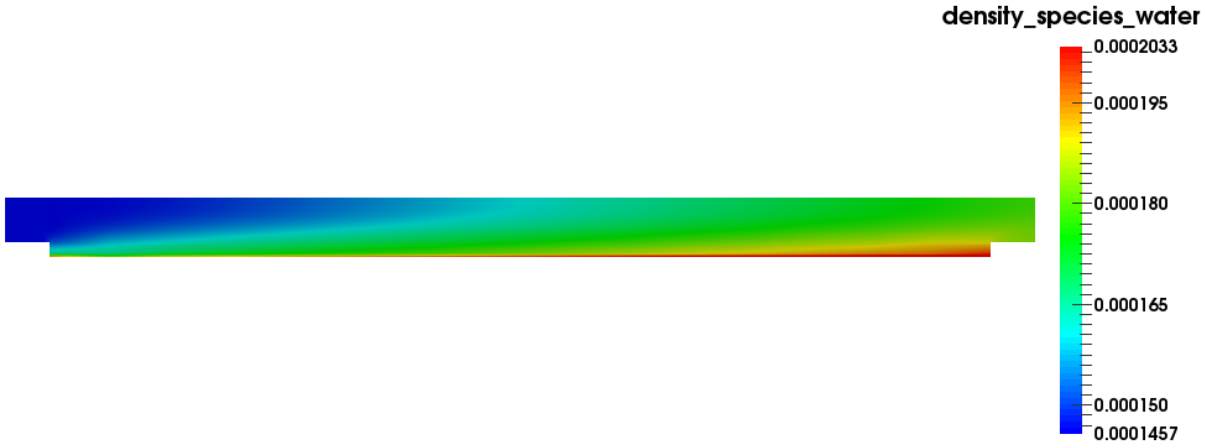

(b) $\lambda_{stoic} = 5.0$

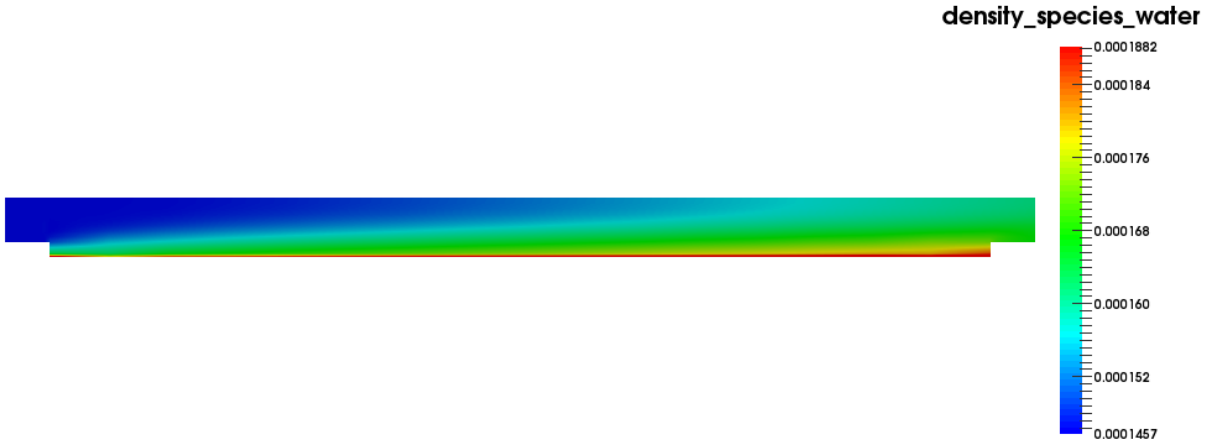

(c) $\lambda_{stoic} = 10.0$

Figure 4.29 – Along Channel CathodeKG model water vapour partial density at $1.0\,\mathrm{A\,cm^{-2}}$ for various λ_{stoic} ratios

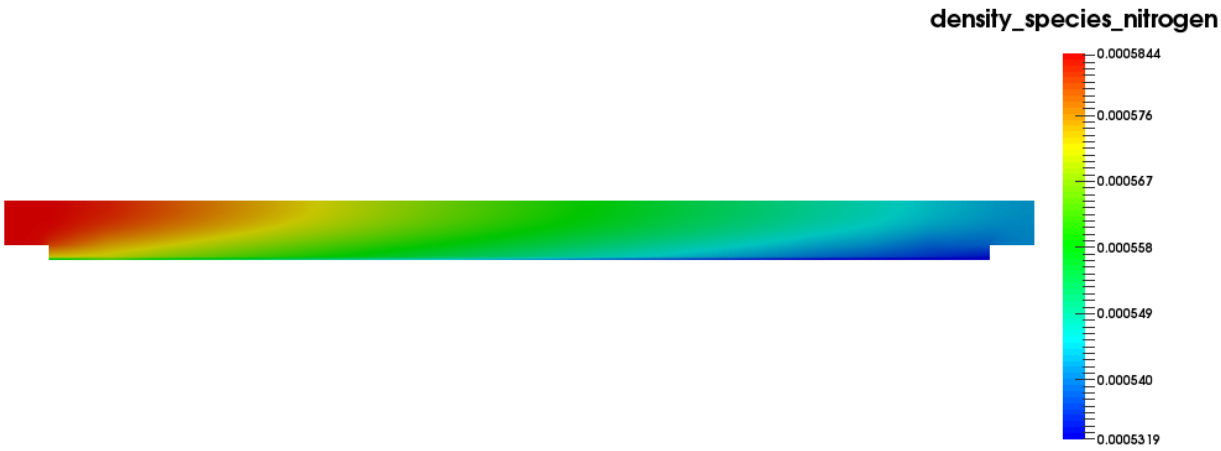

(a) $\lambda_{stoic} = 2.0$

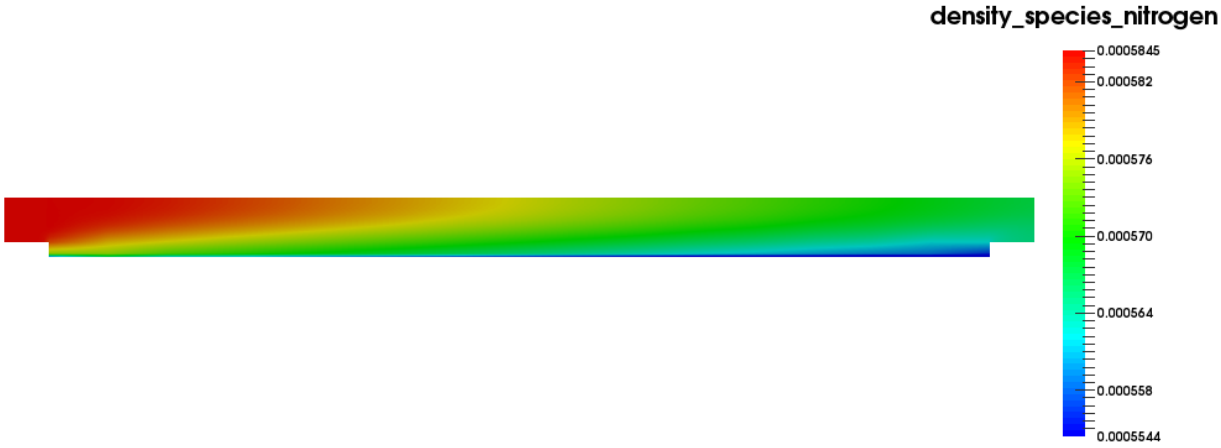

(b) $\lambda_{stoic} = 5.0$

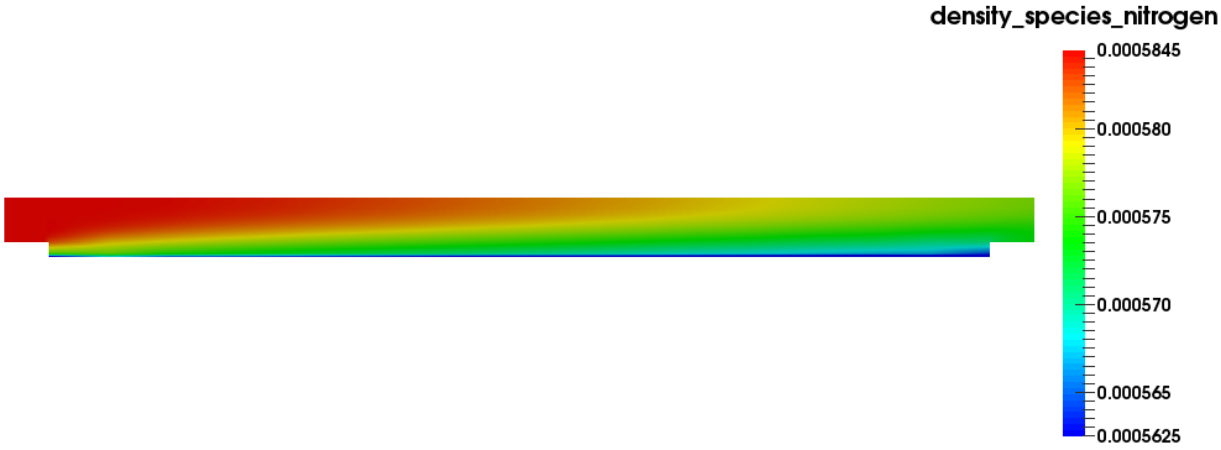

(c) $\lambda_{stoic} = 10.0$

Figure 4.30 – Along Channel CathodeKG model nitrogen partial density at $1.0\,\mathrm{A\,cm^{-2}}$ for various λ_{stoic} ratios

Chapter 5

Conclusion and Future Work

5.1 Conclusion

This work was primarily focused on the implementation and validation of Kerkhof and Geboers' model. The equations were implemented into OpenFCST, and validation was performed using four different benchmark tests. These benchmarks tested that the equations were implemented correctly and could accurately account for all types of mass transport that may occur. A lid driven cavity and backward-facing step tests were performed to test that the equations could correctly account for shear and convection dominated flow respectively. A diffusion bridge was simulated. This confirmed that the volume averaging was done correctly, and that the equations are capable of solving a multi-domain problem including a porous domain. Finally, a Stefan tube simulation confirmed that the equations correctly accounted for multi-component diffusive transport. This is a major form of transport in the porous layers of a PEFC.

Kerkhof and Geboers' equations were then coupled with electrochemical reaction kinetics to account for the electro-chemical reaction occurring in a PEFC. The CathodeKG model was then validated against a simple Cathode model already implemented in OpenFCST. This was done by prescribing an inlet boundary condition where oxygen only consists of 1% of the mixture before being humidified with water vapour. This was done because the Cathode model uses Fickian transport for the oxygen by assuming that the oxygen is an infinitely dilute solution of nitrogen. Under these conditions then the Cathode model's assumptions are valid, and should correctly describe the transport of oxygen in a PEFC.

After the CathodeKG model was validated, simulations were run to see the effect of changing the CL permeability and inlet oxygen concentration in the through-plane direction. For the case of the along the channel direction simulations, the λ_{stoic} was varied. Using the CathodeKG model it was determined that density varied more for the individual species compared to the total densities. Kerkhof and Geboers' equations are able to predict the

velocity of the individual species in the through-plane direction of the cathode. This allowed for the ability to see that there are possibly three circulation regions in the porous layers for the transport of nitrogen. The relative humidity was considered to see if liquid water was forming. At the operating conditions considered, and only in along the channel simulations, liquid water began to form at high current densities near the outlet of the channel. This work presents the first implementation in the literature of a PEFC model including the multi-component mass transport model proposed by Kerkhof and Geboers in 2005 [1, 78]. The model has been used to highlight the effects of multi-component transport and compressibility.

5.2 Future Work

The implementation of Kerkhof and Geboers' model has opened new avenues of research in modeling PEFCs in OpenFCST. These equations allow for both the porous layers and channel to be considered when modeling. Future work could be done modeling a 3D PEFC in OpenFCST. Due to the fact that only a cathode was considered this work, future work could include modeling a full MEA.

The current approach for solving the problem is a brute force method where all equations are solved simultaneously with a direct solver. This results in a slow and a very computationally expensive simulation. Part of the reason this approach was taken is because of the desire to use MUMPS to parallelize the solving of the matrix. This created issues because this was done through PETSC in deal.II, and currently deal.II does not support block matrices with PETSC. If a solver could solve each block of the matrix separately, then each equation could be solved with different solvers optimized for each respective equation. One library that could potentially make this possible is Trilinos [139].

Now that the equations have been shown to be numerically stable future work could remove various simplifying assumptions. For instance, assumptions 3 and 9 in section 2.2 could be removed to account for non-isothermal transport and the more complex shear stress model originally proposed. As well, in section 4.5.4.1 liquid water was shown to form in the cathode under certain conditions. A two-phase model could be implemented that would correctly account for the transport of water in the liquid and vapour phase.

Future work could also be done to implement the classical approach used by researchers. This would allow for a direct comparison with the results obtained using Kerkhof and Geboers' model in OpenFCST.

References

[1] P. Kerkhof and M. Geboers, *AIChE Journal*, **2005,** *51,* 79-121.

[2] S. Shukla *Experimental analysis of inkjet printed polymer electrolyte fuel cell electrodes,* Thesis, University of Alberta, 2016.

[3] D. Carrington and A. Vaughan "Canada condemned at home and abroad for pulling out of Kyoto treaty", 2011.

[4] H. Yang, Z. Wei, and L. Chengzhi, *Applied Energy*, **2009,** *86,* 163-169.

[5] S. Mekhilef, R. Saidur, and A. Safari, *Renewable and Sustainable Energy Reviews*, **2012,** *16,* 981-989.

[6] O. Z. Sharaf and M. F. Orhan, *Renewable and Sustainable Energy Reviews*, **2014,** *32,* 810-853.

[7] K. Tüber, M. Zobel, H. Schmidt, and C. Hebling, *Journal of Power Sources*, **2003,** *122,* 1-8.

[8] K. A. Friedrich, J. Kallo, and J. Schirmer Fuel cells for aircraft application. In *ASME 2009 7th International Conference on Nanochannels, Microchannels, and Minichannels*; American Society of Mechanical Engineers: 2009.

[9] G. M. Renouard-Vallet, J. Kallo, A. K. Friedrich, J. Schirmer, M. Saballus, and G. Schmithals, *ECS Transactions*, **2011,** *30,* 271-280.

[10] T. Keränen, H. Karimäki, J. Viitakangas, J. Vallet, J. Ihonen, P. Hyötylä, H. Uusalo, and T. Tingelöf, *Journal of Power Sources*, **2011,** *196,* 9058-9068.

[11] K. Domican "Mathematical modeling and experimental validation of thin low platinum content and functionally graded cathode catalyst layers", Master's thesis, University of Alberta,.

[12] S. Shukla, K. Domican, K. Karan, S. Bhattacharjee, and M. Secanell, *Electrochimica Acta*, **2015,** *156,* 289-300.

[13] E. Proietti, F. Jaouen, M. Lefvre, N. Larouche, J. Tian, J. Herranz, and J.-P. Dodelet, *Nature communications*, **2011,** *2,* 416.

[14] G. Wu, K. L. More, C. M. Johnston, and P. Zelenay, *Science (New York, N.Y.)*, **2011,** *332,* 443-447.

[15] F. Jaouen, E. Proietti, M. Lefèvre, R. Chenitz, J.-P. Dodelet, G. Wu, H. T. Chung, C. M. Johnston, and P. Zelenay, *Energy & Environmental Science*, **2011,** *4,* 114-130.

[16] M. Secanell, A. Putz, V. Zingan, M. Bhaiya, M. Moore, P. Dobson, P. Wardlaw, and K. Domican "Open-source Fuel Cell Simulation Toolbox (OpenFCST): User and Developer's Reference Guide", 2013.

[17] M. Secanell, A. Putz, P. Wardlaw, V. Zingan, M. Bhaiya, M. Moore, J. Zhou, C. Balen, and K. Domican, *ECS Transactions*, **2014,** *64,* 655–680.

[18] M. S. Secanell *Computational modeling and optimization of proton exchange membrane fuel cells,* Thesis, University of Victoria, 2007.

[19] P. Dobson "Investigation of the polymer electrolyte membrane fuel cell catalyst layer microstructure", Master's thesis, University of Alberta,.

[20] M. Moore "Investigation of the Double-Trap Intrinsic Kinetic Equation for the Oxygen Reduction Reaction and its Implementation into a Membrane Electrode Assembly Model", Master's thesis, University of Alberta,.

[21] M. Moore, A. Putz, and M. Secanell, *Journal of the Electrochemical Society*, **2013,** *160,* F670-F681.

[22] M. Bhaiya "An open-source two-phase non-isothermal mathematical model of a polymer electrolyte membrane fuel cell", Master's thesis, University of Alberta,.

[23] M. Bhaiya, A. Putz, and M. Secanell, *Electrochimica Acta*, **2014,** *147,* 294-309.

[24] M. Bhaiya, A. Putz, and M. Secanell, *ECS Transactions*, **2014,** *64,* 567-579.

[25] P. Wardlaw "Modelling of PEMFC Catalyst Layer Mass Transport and Electro-Chemical Reactions Using Multi-scale Simulations, M. Sc. thesis, University of Alberta", Master's thesis, University of Alberta,.

[26] M. Moore, P. Wardlaw, P. Dobson, J. Boisvert, A. Putz, R. Spiteri, and M. Secanell, *Journal of the Electrochemical Society*, **2014,** *161,* E3125-E3137.

[27] M. Mathias, J. Roth, J. Fleming, and W. Lehnert, *Handbook of Fuel Cells*, **2003,** .

[28] R. OHare, S.-W. Cha, W. Colella, and F. Prinz *Fuel cell fundamentals;* John Wiley & Sons, Hoboken, NJ: 2009.

[29] T. E. Springer, T. Zawodzinski, and S. Gottesfeld, *Journal of the Electrochemical Society*, **1991,** *138,* 2334–2342.

[30] D. M. Bernardi and M. W. Verbrugge, *AIChE journal*, **1991,** *37,* 1151–1163.

[31] C. Siegel, *Energy*, **2008,** *33,* 1331–1352.

[32] D. Singh, D. Lu, and N. Djilali, *International Journal of Engineering Science*, **1999,** *37,* 431–452.

[33] P. Sui and N. Djilali, *Journal of Power Sources*, **2006,** *161,* 294–300.

[34] M. Secanell, K. Karan, A. Suleman, and N. Djilali, *Journal of the Electrochemical Society*, **2008,** *155,* B125–B134.

[35] F. C. Cetinbas, S. G. Advani, and A. K. Prasad, *Journal of The Electrochemical Society*, **2014,** *161,* F803–F813.

[36] A. Fick, *The London, Edinburgh, and Dublin Philosophical Magazine and Journal of Science*, **1855,** *10,* 30-39.

[37] R. Taylor and R. Krishna *Multicomponent mass transfer;* New York : Wiley, c1993: 1993.

[38] C. Boyer, R. Anthony, and A. Appleby, *Journal of Applied Electrochemistry*, **2000,** *30,* 777-786.

[39] C.-P. Wang and H.-S. Chu, *Journal of Power Sources*, **2006,** *159,* 1025-1033.

[40] U. Beuscher, *Journal of the Electrochemical Society*, **2006,** *153,* A1788-A1793.

[41] H. Rivera, J. S. Lawton, D. E. Budil, and E. S. Smotkin, *The Journal of Physical Chemistry B*, **2008,** *112,* 8542-8548.

[42] M. Secanell, B. Carnes, A. Suleman, and N. Djilali, *Electrochimica Acta*, **2007,** *52,* 2668-2682.

[43] J. C. Maxwell, *Philosophical Transactions of the Royal Society of London*, **1867,** 49.

[44] J. Stefan, *Sitzber.Akad.Wiss.Wien*, **1871,** *63,* 63-124.

[45] R. B. Bird, W. E. Stewart, and E. N. Lightfoot *Transport phenomena;* New York : J. Wiley, c2007; Rev. 2nd ed: 2007.

[46] J. B. Duncan and H. Toor, *AIChE Journal*, **1962,** *8,* 38-41.

[47] F. A. Banat, F. A. Al-Rub, R. Jumah, and M. Shannag, *International Communications in Heat and Mass Transfer*, **1999,** *26,* 879-888.

[48] M. Lindstrom and B. Wetton, *arXiv preprint arXiv:1312.1373*, **2013,** .

[49] M. J. Martínez, S. Shimpalee, and J. Van Zee, *Computers & Chemical Engineering*, **2008,** *32,* 2958-2965.

[50] J. Wesselingh and R. Krishna *Mass transfer in multicomponent mixtures;* Delft University Press Delft: 2000.

[51] R. Evans III, G. Watson, and E. Mason, *The Journal of chemical physics*, **1961,** *35,* 2076-2083.

[52] E. A. Mason and A. P. Malinauskas *Gas transport in porous media : the dusty-gas model;* Amsterdam ; New York : Elsevier Scientific Pub. Co., 1983: 1983.

[53] R. Jackson *Transport in porous catalysts;* Amsterdam ; New York : Elsevier Scientific Pub. Co. ; New York : distributors for the U.S. and Canada, Elsevier North-Holland, 1977: 1977.

[54] R. Suwanwarangkul, E. Croiset, M. Fowler, P. Douglas, E. Entchev, and M. Douglas, *Journal of Power Sources*, **2003,** *122,* 9-18.

[55] Y. Vural, L. Ma, D. B. Ingham, and M. Pourkashanian, *Journal of Power Sources*, **2010,** *195,* 4893-4904.

[56] J. Young and B. Todd, *International Journal of Heat and Mass Transfer*, **2005,** *48,* 5338-5353.

[57] J. Fimrite, B. Carnes, H. Struchtrup, and N. Djilali, *Journal of the Electrochemical Society*, **2005,** *152,* A1815-A1823.

[58] L. M. Pant, S. K. Mitra, and M. Secanell, *International Journal of Heat and Mass Transfer*, **2013,** *58,* 70-79.

[59] P. J. Kerkhof, *The Chemical Engineering Journal and the Biochemical Engineering Journal*, **1996,** *64,* 319-343.

[60] E. N. Lightfoot, , **1974,** .

[61] J. Fimrite, B. Carnes, H. Struchtrup, and N. Djilali, *Journal of the Electrochemical Society*, **2005,** *152,* A1815-A1823.

[62] H. Darcy *Les fontaines publiques de la ville de Dijon: exposition et application;* Victor Dalmont: 1856.

[63] S. Whitaker, *Transport in Porous Media*, **1986,** *1,* 3-25.

[64] J. Dupuit *Études théoriques et pratiques sur le mouvement des eaux dans les canaux découverts et à travers les terrains perméables : avec des considérations relatives au régime des grandes eaux, au débouché à leur donner, et à la marche des alluvions dans les rivières à fond mobile;* Dunod: 1863.

[65] P. Forchheimer, *Z.Ver.Deutsch.Ing*, **1901,** *45,* 1788.

[66] D. A. Nield and A. Bejan *Convection in porous media;* Springer Science & Business Media: 2006.

[67] H. Brinkman, *Applied Scientific Research*, **1949,** *1,* 27-34.

[68] H. Brinkman, *Applied Scientific Research*, **1949,** *1,* 81-86.

[69] A. Aiyejina and M. Sastry, *Journal of Fuel Cell Science and Technology*, **2012,** *9,* 011011.

[70] T. Berning, D. M. Lu, and N. Djilali, *Journal of power sources*, **2002,** *106,* 284–294.

[71] T. Berning and N. Djilali, *Journal of the Electrochemical Society*, **2003,** *150,* A1589–A1598.

[72] V. Gurau, H. Liu, and S. Kakac, *AIChE Journal*, **1998,** *44,* 2410–2422.

[73] S. Um, C.-Y. Wang, and K. Chen, *Journal of the Electrochemical society*, **2000,** *147,* 4485–4493.

[74] H. Meng and C.-Y. Wang, *Journal of the Electrochemical Society*, **2004,** *151,* A358–A367.

[75] S. Shimpalee, S. Dutta, W. Lee, and J. Van Zee, *ASME-PUBLICATIONS-HTD*, **1999,** *364,* 367–374.

[76] S. Dutta, S. Shimpalee, and J. Van Zee, *Journal of Applied Electrochemistry*, **2000,** *30,* 135–146.

[77] S. Dutta, S. Shimpalee, and J. Van Zee, *International Journal of Heat and Mass Transfer*, **2001,** *44,* 2029–2042.

[78] P. J. Kerkhof and M. A. Geboers, *Chemical Engineering Science*, **2005,** *60,* 3129–3167.

[79] A. Mills and B. Chang, *Chemical Engineering Science*, **2013,** *90,* 130–136.

[80] A. Faliagas, *Chemical Engineering Science*, **2015,** *123,* 665–668.

[81] P. J. Kerkhof, *Chemical Engineering Science*, **2015,** *123,* 669 - 673.

[82] R. Salcedo-Díaz, R. Ruiz-Femenia, P. Kerkhof, and E. Peters, *Chemical Engineering Science*, **2008,** *63,* 4685–4693.

[83] P. D. Neufeld, A. Janzen, and R. Aziz, *The Journal of chemical physics*, **1972,** *57,* 1100-1102.

[84] T. A. Davidson *A simple and accurate method for calculating viscosity of gaseous mixtures [microform];* Washington, DC : U.S. Dept. of the Interior, Bureau of Mines, 1993]: 1993.

[85] J. O. Hirschfelder, C. F. Curtiss, and R. B. Bird *Molecular theory of gases and liquids;* New York, Wiley 1964]; Corrected printing with notes added: 1964.

[86] B. E. Poling, J. M. Prausnitz, and J. P. O'Connell *The properties of gases and liquids;* New York : McGraw-Hill, c2001; 5th ed: 2001.

[87] C. R. Wilke, *Journal of Chemical Physics*, **1950,** *18,* 517.

[88] P. J. Kerkhof, *AIChE Journal*, **2011,** *57,* 1099-1099.

[89] T. Coplen, *J.Phys.Chem.Ref.Data*, **1997,** *26,*.

[90] S. Whitaker *The method of volume averaging;* Dordrecht ; Boston : Kluwer Academic, c1999: 1999.

[91] V. Zingan, P. Mangal, P. Minev, A. Putz, and M. Secanell, , **In preparation, 2016,** .

[92] W. G. Gray and P. C. Y. Lee, *International Journal of Multiphase Flow*, **1977,** *3,* 333-340.

[93] S. Whitaker, *Industrial and Engineering Chemistry*, **1969,** *61,* 14-28.

[94] F. A. Howes and S. Whitaker, *Chemical Engineering Science*, **1985,** *40,* 1387-1392.

[95] J. C. Slattery, *AIChE Journal*, **1967,** *13,* 1066–1071.

[96] D. Bruggeman, *Ann. Phys.*, **1935,** *24,* 636–642.

[97] J. Pharoah, K. Karan, and W. Sun, *Journal of Power Sources*, **2006,** *161,* 214-224.

[98] M. M. Tomadakis and S. V. Sotirchos, *AIChE Journal*, **1993,** *39,* 397–412.

[99] J. N. Reddy *An introduction to nonlinear finite element analysis. [electronic resource];* Oxford ; New York : Oxford University Press, 2004: 2004.

[100] W. Bangerth, T. Heister, L. Heltai, G. Kanschat, M. Kronbichler, M. Maier, B. Turcksin, and T. D. Young, *Archive of Numerical Software*, **2013,** *3,*.

[101] W. Bangerth, R. Hartmann, and G. Kanschat, *ACM Trans. Math. Softw.*, **2007,** *33,* 24/1–24/27.

[102] J. Donea and A. Huerta *Finite element methods for flow problems;* John Wiley & Sons: 2003.

[103] C. Taylor and P. Hood, *Computers & Fluids*, **1973,** *1,* 73-100.

[104] T. A. Davis, *ACM Trans. Math. Softw.*, **2004,** *30,* 196-199.

[105] P. R. Amestoy, I. S. Duff, J. Koster, and J.-Y. L'Excellent, *SIAM Journal on Matrix Analysis and Applications*, **2001,** *23,* 15-41.

[106] P. R. Amestoy, A. Guermouche, J.-Y. L'Excellent, and S. Pralet, *Parallel Computing*, **2006,** *32,* 136-156.

[107] S. Balay, S. Abhyankar, M. F. Adams, J. Brown, P. Brune, K. Buschelman, L. Dalcin, V. Eijkhout, W. D. Gropp, D. Kaushik, M. G. Knepley, L. C. McInnes, K. Rupp, B. F. Smith, S. Zampini, and H. Zhang "PETSc Web page", `http://www.mcs.anl.gov/petsc`, 2015.

[108] S. Balay, S. Abhyankar, M. F. Adams, J. Brown, P. Brune, K. Buschelman, L. Dalcin, V. Eijkhout, W. D. Gropp, D. Kaushik, M. G. Knepley, L. C. McInnes, K. Rupp, B. F. Smith, S. Zampini, and H. Zhang "PETSc Users Manual", Technical Report ANL-95/11 - Revision 3.6, Argonne National Laboratory, 2015.

[109] S. Balay, W. D. Gropp, L. C. McInnes, and B. F. Smith Efficient Management of Parallelism in Object Oriented Numerical Software Libraries. In *Modern Software Tools in Scientific Computing*; E. Arge, A. M. Bruaset, and H. P. Langtangen, Eds.; Birkhäuser Press: 1997.

[110] C. Burstedde, L. C. Wilcox, and O. Ghattas, *SIAM Journal on Scientific Computing*, **2011,** *33,* 1103-1133.

[111] G. Karypis and V. Kumar, *SIAM Journal on Scientific Computing*, **1999,** *20,* 359-392.

[112] U. Ghia, K. N. Ghia, and C. Shin, *Journal of computational physics*, **1982,** *48,* 387–411.

[113] B. F. Armaly, F. Durst, J. Pereira, and B. Schönung, *Journal of Fluid Mechanics*, **1983,** *127,* 473–496.

[114] J. Ahrens, B. Geveci, C. Law, C. Hansen, and C. Johnson "36-ParaView: An End-User Tool for Large-Data Visualization", 2005.

[115] P. Mangal "Experimental Study of Mass Transport Parameters of PEFC Porous Media", Master's thesis, University of Alberta, 2014.

[116] P. Mangal, L. M. Pant, N. Carrigy, M. Dumontier, V. Zingan, S. Mitra, and M. Secanell, *Electrochimica Acta*, **2015,** *167,* 160-171.

[117] R. Carty and T. Schrodt, *Industrial & Engineering Chemistry Fundamentals*, **1975,** *14,* 276-278.

[118] B. Markham and F. Rosenberger, *Chemical Engineering Communications*, **1980,** *5,* 287–298.

[119] V. Dilman, O. Kashirskaya, and V. Lotkhov, *Theoretical Foundations of Chemical Engineering*, **2010,** *44,* 379-383.

[120] J. X. Wang, J. Zhang, and R. R. Adzic, *The Journal of Physical Chemistry A*, **2007,** *111,* 12702–12710.

[121] M. Secanell, A. Putz, S. Shukla, P. Wardlaw, M. Bhaiya, L. M. Pant, and M. Sabharwal, *ECS Transactions*, **2015,** *69,* 157–187.

[122] L. M. Pant, S. K. Mitra, and M. Secanell, *Journal of Power Sources*, **2012,** *206,* 153-160.

[123] W. Sun, B. A. Peppley, and K. Karan, *Electrochimica Acta*, **2005,** *50,* 3359-3374.

[124] M. Secanell, R. Songprakorp, N. Djilali, and A. Suleman, *Structural and Multidisciplinary Optimization*, **2010,** *40,* 563–583.

[125] N. Ahmadi, S. Rezazadeh, I. Mirzaee, and N. Pourmahmoud, *Journal of mechanical science and technology*, **2012,** *26,* 2247–2257.

[126] M. He, Z. Huang, P. Sun, and C. Wang, *Journal of The Electrochemical Society*, **2013,** *160,* F324–F336.

[127] Y.-S. Li, Y. Han, and J.-M. Zhan, *Journal of Fuel Cell Science and Technology*, **2013,** *10,* 031003.

[128] A. Iranzo, A. Salva, E. Tapia, and F. Rosa, *Journal of Fuel Cell Science and Technology*, **2014,** *11,* 031007.

[129] M. Ismail, K. Hughes, D. Ingham, L. Ma, and M. Pourkashanian, *Applied Energy*, **2012,** *95,* 50–63.

[130] G.-S. Kim, P. Sui, A. Shah, and N. Djilali, *Journal of Power Sources*, **2010,** *195,* 3240–3249.

[131] P. Sui, S. Kumar, and N. Djilali, *Journal of Power Sources*, **2008,** *180,* 410–422.

[132] P. Dobson, C. Lei, T. Navessin, and M. Secanell, *Journal of the Electrochemical Society*, **2012,** *159,* B514-B523.

[133] J. H. Nam and M. Kaviany, *International Journal of Heat and Mass Transfer*, **2003,** *46,* 4595-4611.

[134] M. Eikerling, A. Ioselevich, and A. Kornyshev, *Fuel Cells*, **2004,** *4,* 131-140.

[135] M. Secanell, K. Karan, A. Suleman, and N. Djilali, *Electrochimica Acta*, **2007,** *52,* 6318-6337.

[136] S. Shukla, D. Stanier, M. Saha, J. Stumper, and M. Secanell, *Journal of The Electrochemical Society*, **2016,** *163,* F677–F687.

[137] D. Song, Q. Wang, Z. Liu, T. Navessin, M. Eikerling, and S. Holdcroft, *Journal of Power Sources*, **2004,** *126,* 104-111.

[138] A. Kumar and R. G. Reddy, *Journal of Power Sources*, **2003,** *113,* 11–18.

[139] M. Heroux, R. Bartlett, V. H. R. Hoekstra, J. Hu, T. Kolda, R. Lehoucq, K. Long, R. Pawlowski, E. Phipps, A. Salinger, H. Thornquist, R. Tuminaro, J. Willenbring, and A. Williams "An Overview of Trilinos", Technical Report SAND2003-2927, Sandia National Laboratories, 2003.

[140] P. Chadwick *Continuum mechanics: concise theory and problems;* Mineola, N.Y. : Dover Publications, 1999; 2nd corr. and enl. ed: 1999.

[141] F. C. McQuiston and J. D. Parker *Heating, ventilating, and air conditioning: analysis and design;* John Wiley and Sons., Inc., New York, NY: 2005.

Appendices

Appendix A

Representative Elementary Volume Averaging Derivations

A.1 Continuity Equation

$$0 = \langle \nabla \cdot \boldsymbol{F}_{mass_\alpha} \rangle \tag{A.1}$$

Begin by applying equation (2.55) resulting in:

$$0 = \nabla \cdot \langle \boldsymbol{F}_{mass_\alpha} \rangle + \frac{1}{V_{REV}} \oint_{A_{\beta\gamma}} \boldsymbol{F}_{mass_\alpha} \cdot \boldsymbol{n}_{\beta\gamma} \, \mathrm{d}A \tag{A.2}$$

Remembering that no penetration is assumed along the boundary of the porous medium control volume, then the surface integral in equation (A.2) must be zero. Opening $\boldsymbol{F}_{mass_\alpha}$ the averaging theorem identities can be applied further. This is done by applying equations (2.52) and (2.48) as follows:

$$\begin{aligned} \langle \boldsymbol{F}_{mass_\alpha} \rangle &= \langle \rho_\alpha \boldsymbol{v}_\alpha \rangle \\ &\approx \frac{1}{\varepsilon} \langle \rho_\alpha \rangle \langle \boldsymbol{v}_\alpha \rangle \\ &= \langle \rho_\alpha \rangle \langle \boldsymbol{v}_\alpha \rangle^f \end{aligned} \tag{A.3}$$

In conclusion, the volume averaged continuity equation can be expressed as:

$$0 = \nabla \cdot \langle \boldsymbol{F}_{mass_\alpha} \rangle = \langle \rho_\alpha \rangle \langle \boldsymbol{v}_\alpha \rangle^f \tag{A.4}$$

A.2 Momentum Equation

$$0 = \langle \nabla \cdot (\hat{\boldsymbol{F}}_{mom_\alpha} + P_\alpha \hat{\mathbf{I}} - \hat{\boldsymbol{\tau}}_\alpha) - (\rho_\alpha \boldsymbol{g} + \boldsymbol{D}_\alpha) \rangle \tag{A.5}$$

Begin by applying equations (2.50) and (2.57) resulting in:

$$0 = \nabla \cdot (\langle \hat{\boldsymbol{F}}_{mom_\alpha} \rangle + \langle P_\alpha \rangle \hat{\mathbf{I}} - \langle \hat{\boldsymbol{\tau}}_\alpha \rangle) + \frac{1}{V_{REV}} \oint_{A_{\beta\gamma}} \left(\hat{\boldsymbol{F}}_{mom_\alpha} + P_\alpha \hat{\mathbf{I}} - \hat{\boldsymbol{\tau}}_\alpha \right) \boldsymbol{n}_{\beta\gamma} \, \mathrm{d}A - (\langle \rho_\alpha \rangle \boldsymbol{g} + \langle \boldsymbol{D}_\alpha \rangle) \quad \text{(A.6)}$$

Remembering that no penetration is assumed along the boundary of the porous medium control volume, then the $\hat{\boldsymbol{F}}_{mom_\alpha}$ term in the surface integral in equation (A.6) must be zero. Now each of the terms must be opened and averaged individually. Beginning with $\langle \hat{\boldsymbol{F}}_{mom_\alpha} \rangle$, equation (2.52) must be applied twice. Followed by equation (2.48) twice to transform the phase averaged velocities into the correct intrinsic average form as follows:

$$\begin{aligned} \langle \hat{\boldsymbol{F}}_{mom_\alpha} \rangle &= \langle \rho_\alpha \boldsymbol{v}_\alpha \otimes \boldsymbol{v}_\alpha \rangle \\ &\approx \frac{1}{\varepsilon} \langle \rho_\alpha \rangle \langle \boldsymbol{v}_\alpha \otimes \boldsymbol{v}_\alpha \rangle \\ &\approx \frac{1}{\varepsilon^2} \langle \rho_\alpha \rangle \langle \boldsymbol{v}_\alpha \rangle \otimes \langle \boldsymbol{v}_\alpha \rangle \\ &= \frac{1}{\varepsilon} \langle \rho_\alpha \rangle \langle \boldsymbol{v}_\alpha \rangle^f \otimes \langle \boldsymbol{v}_\alpha \rangle \\ &= \langle \rho_\alpha \rangle \langle \boldsymbol{v}_\alpha \rangle^f \otimes \langle \boldsymbol{v}_\alpha \rangle^f \end{aligned} \quad \text{(A.7)}$$

Since gases are assumed to be ideal then $\langle P_\alpha \rangle$ can easily be determined by applying equation (2.50) where all other terms but density are constants like so:

$$\begin{aligned} \langle P_\alpha \rangle &= \langle \rho_\alpha RT \rangle \\ &= \langle \rho_\alpha \rangle RT \end{aligned} \quad \text{(A.8)}$$

The stress tensor term, $\langle \hat{\boldsymbol{\tau}}_\alpha \rangle$, and its surface integral are discussed in section 2.4.3.1. The final term $\langle \boldsymbol{D}_\alpha \rangle$ is done similarly to $\langle \hat{\boldsymbol{F}}_{mom_\alpha} \rangle$ term by using equations (2.50), (2.52), and

(2.48).

$$\begin{aligned}
\langle \boldsymbol{D}_\alpha \rangle &= \left\langle \sum_{\beta=1}^{N} P_\alpha P_\beta \hat{\boldsymbol{D}}_{\alpha\beta}(\boldsymbol{v}_\beta - \boldsymbol{v}_\alpha) \right\rangle \\
&= \sum_{\beta=1}^{N} \langle P_\alpha P_\beta \hat{\boldsymbol{D}}_{\alpha\beta}(\boldsymbol{v}_\beta - \boldsymbol{v}_\alpha) \rangle \\
&\approx \frac{1}{\varepsilon} \sum_{\beta=1}^{N} \langle P_\alpha \rangle \langle P_\beta \hat{\boldsymbol{D}}_{\alpha\beta}(\boldsymbol{v}_\beta - \boldsymbol{v}_\alpha) \rangle \\
&\approx \frac{1}{\varepsilon^2} \sum_{\beta=1}^{N} \langle P_\alpha \rangle \langle P_\beta \rangle \hat{\boldsymbol{D}}_{\alpha\beta}(\langle \boldsymbol{v}_\beta - \boldsymbol{v}_\alpha \rangle) \\
&= \frac{1}{\varepsilon^2} \sum_{\beta=1}^{N} \langle P_\alpha \rangle \langle P_\beta \rangle \hat{\boldsymbol{D}}_{\alpha\beta}(\langle \boldsymbol{v}_\beta \rangle - \langle \boldsymbol{v}_\alpha \rangle) \\
&= \frac{1}{\varepsilon} \sum_{\beta=1}^{N} \langle P_\alpha \rangle \langle P_\beta \rangle \hat{\boldsymbol{D}}_{\alpha\beta}(\langle \boldsymbol{v}_\beta \rangle^f - \langle \boldsymbol{v}_\alpha \rangle^f)
\end{aligned} \tag{A.9}$$

In conclusion, the volume averaged momentum equation can be expressed as:

$$\begin{aligned}
0 = \nabla \cdot \left(\langle \hat{\boldsymbol{F}}_{mom_\alpha} \rangle + \langle P_\alpha \rangle \hat{\mathbf{I}} - \langle \hat{\boldsymbol{\tau}}_\alpha \rangle \right) + \frac{1}{V_{REV}} \oint_{A_{\beta\gamma}} \left(P_\alpha \hat{\mathbf{I}} - \hat{\boldsymbol{\tau}}_\alpha \right) \boldsymbol{n}_{\beta\gamma} \, \mathrm{d}A \\
- \left(\langle \rho_\alpha \rangle \boldsymbol{g} + \langle \boldsymbol{D}_\alpha \rangle \right)
\end{aligned} \tag{A.10}$$

$$\langle \hat{\boldsymbol{F}}_{mom_\alpha} \rangle = \langle \rho_\alpha \rangle \langle \boldsymbol{v}_\alpha \rangle^f \otimes \langle \boldsymbol{v}_\alpha \rangle^f \tag{A.11}$$

$$\langle P_\alpha \rangle = \langle \rho_\alpha \rangle RT \tag{A.12}$$

$$\langle \boldsymbol{D}_\alpha \rangle = \frac{1}{\varepsilon} \sum_{\beta=1}^{N} \langle P_\alpha \rangle \langle P_\beta \rangle \hat{\boldsymbol{D}}_{\alpha\beta}(\langle \boldsymbol{v}_\beta \rangle^f - \langle \boldsymbol{v}_\alpha \rangle^f) \tag{A.13}$$

Appendix B

Proofs

B.1 Tensors

If the reader has difficulties understanding the validity of any of the intermediate steps in the following proofs, then it is highly recommended to read Chapter 1 of *Continuum Mechanics: Concise Theory and Problems* [140]. As all of the following proofs can be derived from that chapter.

If $\hat{\boldsymbol{A}}$ is an arbitrary tensor and $\boldsymbol{u}$ is an arbitrary vector, then:

$$\nabla \cdot (\hat{\boldsymbol{A}}\boldsymbol{u}) = \boldsymbol{u} \cdot \nabla \cdot \hat{\boldsymbol{A}} + \mathrm{tr}(\hat{\boldsymbol{A}}\nabla\boldsymbol{u}) \tag{B.1}$$

Proof. Begin by expanding the LHS as follows:

$$\begin{aligned}
\nabla \cdot (\hat{\boldsymbol{A}}\boldsymbol{u}) &= \nabla \cdot ((A_{ij}\boldsymbol{e}_i \otimes \boldsymbol{e}_j)(u_k\boldsymbol{e}_k)) \\
&= \nabla \cdot (A_{ij}(u_k\boldsymbol{e}_k \cdot \boldsymbol{e}_j)\boldsymbol{e}_i) \\
&= \nabla \cdot (A_{ij}u_k\delta_{kj}\boldsymbol{e}_i) \\
&= \nabla \cdot (A_{ij}u_j\boldsymbol{e}_i) \\
&= \frac{\partial}{\partial x_i}(A_{ij}u_j) \\
&= u_j\frac{\partial A_{ij}}{\partial x_i} + A_{ij}\frac{\partial u_j}{\partial x_i}
\end{aligned} \tag{B.2}$$

Consider the RHS now, and expanding the first term as follows:

$$\begin{aligned}
\boldsymbol{u} \cdot \nabla \cdot \hat{\boldsymbol{A}} &= u_k\boldsymbol{e}_k \cdot \frac{\partial T_{ij}}{\partial x_i}\boldsymbol{e}_j \\
&= u_k\frac{\partial T_{ij}}{\partial x_i}\boldsymbol{e}_k \cdot \boldsymbol{e}_j \\
&= u_k\frac{\partial T_{ij}}{\partial x_i}\delta_{kj} \\
&= u_j\frac{\partial T_{ij}}{\partial x_i}
\end{aligned} \tag{B.3}$$

Now expand the second term of the RHS as follows:

$$\begin{aligned}
\text{tr}(\hat{\boldsymbol{A}}\nabla\boldsymbol{u}) &= \text{tr}\left[A_{ij}\boldsymbol{e}_i \otimes \boldsymbol{e}_j \left(\frac{\partial u_k}{\partial x_q}\boldsymbol{e}_k \otimes \boldsymbol{e}_q\right)\right] \\
&= \text{tr}\left[A_{ij}\frac{\partial u_j}{\partial x_q}\boldsymbol{e}_i \otimes \boldsymbol{e}_q\right] \\
&= A_{ij}\frac{\partial u_j}{\partial x_q}\,\text{tr}\left[\boldsymbol{e}_i \otimes \boldsymbol{e}_q\right] \\
&= A_{ij}\frac{\partial u_j}{\partial x_q}\boldsymbol{e}_i \otimes \boldsymbol{e}_q \\
&= A_{ij}\frac{\partial u_j}{\partial x_q}\delta_{iq} \\
&= A_{ij}\frac{\partial u_j}{\partial x_i}
\end{aligned} \tag{B.4}$$

Combining equations (B.3) and (B.4), this results in the RHS of the equation being:

$$\boldsymbol{u}\cdot\nabla\cdot\hat{\boldsymbol{A}} + \text{tr}(\hat{\boldsymbol{A}}\nabla\boldsymbol{u}) = u_j\frac{\partial A_{ij}}{\partial x_i} + A_{ij}\frac{\partial u_j}{\partial x_i} \tag{B.5}$$

Thus, it can clearly be seen that equations (B.2) and (B.5) are the same, and so the identity in equation (B.1) must be true. □

If $\hat{\boldsymbol{A}}_{\boldsymbol{s}}$ is an arbitrary symmetric tensor and $\boldsymbol{u}$ is an arbitrary vector, then:

$$\nabla\cdot(\hat{\boldsymbol{A}}_{\boldsymbol{s}}\boldsymbol{u}) = \boldsymbol{u}\cdot\nabla\cdot\hat{\boldsymbol{A}}_{\boldsymbol{s}} + \nabla\boldsymbol{u} : \hat{\boldsymbol{A}}_{\boldsymbol{s}} \tag{B.6}$$

Proof. The following properties of traces and tensors are required:

$$\text{tr}(\hat{\boldsymbol{A}}\hat{\boldsymbol{B}}) = \text{tr}(\hat{\boldsymbol{B}}\hat{\boldsymbol{A}}) \tag{B.7}$$

$$\hat{\boldsymbol{A}} : \hat{\boldsymbol{B}} = \text{tr}(\hat{\boldsymbol{A}}^{\boldsymbol{T}}\hat{\boldsymbol{B}}) = \text{tr}(\hat{\boldsymbol{A}}\hat{\boldsymbol{B}}^{\boldsymbol{T}}) \tag{B.8}$$

Assuming that the arbitrary tensor in equation (B.1) is symmetric, i.e. $\hat{\boldsymbol{A}} = \hat{\boldsymbol{A}}_{\boldsymbol{s}}$, then equation (B.7) and (B.8) can be applied as follows:

$$\begin{aligned}
\nabla\cdot(\hat{\boldsymbol{A}}_{\boldsymbol{s}}\boldsymbol{u}) &= \boldsymbol{u}\cdot\nabla\cdot\hat{\boldsymbol{A}}_{\boldsymbol{s}} + \text{tr}((\nabla\boldsymbol{u})\hat{\boldsymbol{A}}_{\boldsymbol{s}}) \\
\nabla\cdot(\hat{\boldsymbol{A}}_{\boldsymbol{s}}\boldsymbol{u}) &= \boldsymbol{u}\cdot\nabla\cdot\hat{\boldsymbol{A}}_{\boldsymbol{s}} + \nabla\boldsymbol{u} : \hat{\boldsymbol{A}}_{\boldsymbol{s}}^{\boldsymbol{T}}
\end{aligned} \tag{B.9}$$

However, since $\hat{\boldsymbol{A}}_{\boldsymbol{s}}$ is symmetric this means that $\hat{\boldsymbol{A}}_{\boldsymbol{s}} = \hat{\boldsymbol{A}}_{\boldsymbol{s}}^{\boldsymbol{T}}$. So equation (B.9) becomes:

$$\nabla\cdot(\hat{\boldsymbol{A}}_{\boldsymbol{s}}\boldsymbol{u}) = \boldsymbol{u}\cdot\nabla\cdot\hat{\boldsymbol{A}}_{\boldsymbol{s}} + \nabla\boldsymbol{u} : \hat{\boldsymbol{A}}_{\boldsymbol{s}} \tag{B.10}$$

Equation (B.10) is the same as equation (B.6), thus the identity is true. □

Appendix C

Sample Calculations

C.1 Relating Air-to-Fuel Ratio, Current Density, and Inlet Velocity

The along the channel geometry specified is:

$$h = 0.1\,\text{cm} \tag{C.1}$$

$$L = 2.1\,\text{cm} \tag{C.2}$$

where h is the height of the channel, and L is the length of the active area of the PEFC. Due to fact that the PEFC is being represented in 2D space, the width into the page will be treated as 1 cm. This results in the following areas and volumes for the geometry:

$$A_{in} = wh = 0.1\,\text{cm}^2 \tag{C.3}$$

$$A_{act} = wL = 2.1\,\text{cm}^2 \tag{C.4}$$

$$Q_{air} = v_{avg}A_{in} = 0.1v_{avg}\ \text{cm}^3\,\text{s}^{-1} \tag{C.5}$$

where A_{in} is the area of the inlet (cm^2), A_{act} is the active area of the CL (cm^2), w is the width into the page (1 cm), Q_{air} is the flow rate of air entering the channel ($\text{cm}^3\,\text{s}^{-1}$), and v_{avg} is the average velocity at the inlet of the channel (cm/s). The air entering is at a temperature and pressure of 80 °C and 101 325 Pa, with a relative humidity of 50%. In dry air, it is considered that the molar fraction of oxygen is 0.21. This gives the following equations for molar fractions of the humid air:

$$x_{O_2} = 0.21(1 - x_{H_2O}) \tag{C.6}$$

$$x_{H_2O} = \frac{P_{sat}RH}{P_{tot}} \tag{C.7}$$

$$\tag{C.8}$$

where x_{O_2} and x_{H_2O} are the molar fractions of oxygen and water vapour in the humid air, P_{sat} is the saturated pressure (47 370 Pa [141]), RH is the relative humidity (0.5), and P_{tot} is the total pressure (101 325 Pa). using the above numbers this gives an oxygen and water vapour molar fraction of approximately 0.161 and 0.234 respectively. The molar mass of the humid air, M_{humid}, is:

$$M_{humid} = (1 - x_{H_2O})M_{dry} + x_{H_2O}M_{H_2O} \tag{C.9}$$
$$= (1 - 0.234)28.97 \times 10^{-3} + 0.234(18.02 \times 10^{-3}) \tag{C.10}$$
$$= 26.4 \times 10^{-3}\,\mathrm{kg\,mol^{-1}} \tag{C.11}$$

where M_{dry} is the molar mass of dry air ($28.97 \times 10^{-3}\,\mathrm{kg\,mol^{-1}}$), and M_{H_2O} is the molar mass of water vapour ($18.02 \times 10^{-3}\,\mathrm{kg\,mol^{-1}}$). Now the density of humid air, ρ_{humid}, are can now be calculated as follows:

$$\rho_{humid} = \frac{P_{tot}M_{humid}}{RT} \tag{C.12}$$
$$= \frac{101325(26.4 \times 10^{-3})}{8.314(353.15)} \tag{C.13}$$
$$= 0.911\,\mathrm{kg\,m^{-3}} \tag{C.14}$$
$$= 9.11 \times 10^{-4}\,\mathrm{g\,cm^{-3}} \tag{C.15}$$

where R is the ideal gas constant ($8.314\,\mathrm{J\,K^{-1}\,mol^{-1}}$), T is the temperature (353.15 K). Finally, the current density, air-to-fuel ratio, and velocity can be related as follows:

$$\frac{Q_{air}\rho_{humid}}{M_{humid}} = \frac{1}{x_{O_2}}\left(\frac{jA_{act}}{4F}\right)\lambda_{stoic} \qquad \leftarrow Q_{air} = v_{avg}A_{in} \tag{C.16}$$
$$v_{avg} = \frac{M_{humid}}{x_{O_2}A_{in}\rho_{humid}}\left(\frac{jA_{act}}{4F}\right)\lambda_{stoic} \tag{C.17}$$

where j is the current density ($\mathrm{A\,cm^{-2}}$), F is Faraday's constant ($96\,485\,\mathrm{C\,mol^{-1}}$), and λ_{stoic} is the oxygen to stoichiometric ratio. For the case when $\lambda_{stoic} = 1$ and the current density is $1.0\,\mathrm{A\,m^{-2}}$ then the average velocity at the inlet is:

$$v_{avg} = \frac{26.4}{0.161(0.1)9.11 \times 10^{-4}}\left(\frac{1.0(2.1)}{4(96485)}\right) \tag{C.18}$$
$$v_{avg} = 9.80\,\mathrm{cm\,s^{-1}}. \tag{C.19}$$